

INVESTIGATIONS INTO CONTROL STRATEGIES AND INTEGRATED CHARGING SOLUTIONS FOR SWITCHED RELUCTANCE MOTOR-DRIVEN ELECTRIC VEHICLES

Thesis

Submitted in partial fulfillment of the requirements for the degree of

DOCTOR OF PHILOSOPHY

by

FAHEEMALI T.



DEPARTMENT OF ELECTRICAL AND ELECTRONICS ENGINEERING,
NATIONAL INSTITUTE OF TECHNOLOGY KARNATAKA,
SURATHKAL, MANGALORE -575025

October, 2024

DECLARATION

by the Ph.D. Research Scholar

I hereby *declare* that the Research Thesis entitled “**Investigations into Control Strategies and Integrated Charging Solutions for Switched Reluctance Motor-Driven Electric Vehicles**” which is being submitted to the **National Institute of Technology Karnataka, Surathkal** in partial fulfillment of the requirement for the award of the Degree of **Doctor of Philosophy in Electrical and Electronics Engineering** is a *bonafide report of the research work carried out by me*. The material contained in this Research Thesis has not been submitted to any University or Institution for the award of any degree.



.....
FAHEEMALI T, 197111

Department of Electrical and Electronics Engineering

Place: NITK-Surathkal

Date: 23-10-2024

CERTIFICATE

This is to *certify* that the Research Thesis entitled “**Investigations into Control Strategies and Integrated Charging Solutions for Switched Reluctance Motor-Driven Electric Vehicles**” submitted by **Faheemali T** (Register Number: 197111) as the record of the research work carried out by him, is *accepted as the Research Thesis submission* in partial fulfillment of the requirements for the award of degree of **Doctor of Philosophy**.



Dr. Arun Dominic D.
(Research Guide)



Dr. Prajof Prabhakaran
(Research Co-guide)



Dr. Debashisha Jena
(Chairman-DRPC, EEE dept.)

Acknowledgements

I am deeply grateful for the support and guidance I received throughout the journey of this dissertation.

I am indebted to *Dr. Arun Dominic D.* and *Dr. Prajof Prabhakaran* for their invaluable mentorship as my Ph.D. supervisors. Their unwavering support and encouragement have been instrumental in shaping this work.

I am grateful to the *National Institute of Technology Karnataka, Surathkal (NITK)*, for providing me with the opportunity to pursue my research, and to the *Ministry of Human Resource Development, Government of India*, for awarding me a research scholarship.

Special appreciation goes to the members of my research progress assessment committee (RPAC), *Dr. Dharavath Kishan* and *Dr. Nikhil K S*, for their insightful feedback and guidance.

I extend my thanks to the former Heads of Department, *Prof. Dattatraya Narayan Gaonkar*, *Prof. Shubhanga K N*, and *Prof. Gururaj S Punekar*, as well as the current HOD, *Prof. Debashisha Jena*, and the secretary of DRPC, *Dr. Tukaram Moger*, for their support and provision of resources essential for my research endeavors.

My sincere gratitude goes to *Mr. Marupuru Vinod*, *Mr. Muthumula Rama Narayana Reddy*, *Mr. Sourav Prasad*, *Mr. Vivek Kumar*, *Mr. Sunil Mandal* and *Miss. Bussa Vinusha* for their assistance and valuable contributions at different stages of my research.

Lastly, I am deeply indebted to my family members for their unwavering love and patience, which has been my source of strength throughout this journey.

Faheemali T

Abstract

Electric vehicles (EVs) are increasingly recognized as a vital solution to mitigate greenhouse gas emissions and air pollution in the transportation sector. However, challenges such as limited driving range, higher upfront costs, and dependence on rare earth minerals hinder their widespread adoption. One promising solution lies in the Switched Reluctance Motor (SRM), distinguished by its simple structure devoid of permanent magnets or rotor conductors. This design offers inherent advantages such as efficient operation in high temperatures, robust fault tolerance, and minimal rotor losses, rendering SRMs a compelling choice for EV propulsion.

Furthermore, the integration of integrated on-board chargers (IOBCs) adds another layer of efficiency and functionality to EV systems. By seamlessly combining motor driving and charging functions, IOBCs not only promise cost savings and reduced complexity but also offer increased power density. Notably, with bidirectional capability, IOBCs enable EVs to both charge from external sources and supply power back to the grid. This bidirectional functionality holds immense significance for diverse operating scenarios such as grid-to-vehicle (G2V), vehicle-to-grid (V2G), vehicle-to-load (V2L), and vehicle-to-home (V2H).

This thesis explores the promising prospects of utilizing SRM drives in EVs and investigates the integration of IOBC systems. Acknowledging challenges such as higher torque ripple and lower power density associated with SRM motors for EVs, the research emphasizes the need for further research and enhancement in this domain. With a primary focus on enhancing efficiency, reducing costs, and increasing the overall power density of EV systems, the study aims to address key obstacles hindering the widespread adoption of EVs while advancing sustainable transportation solutions.

This thesis also presents a precise simulation model of SRM for analyzing and conducting simulation studies on the proposed methods. This necessitates the characterization of the SRM, for which various methods are available in the literature, ranging from analytical approaches to electromagnetic Finite Element Analysis (FEA) tools. While FEA-based models

offer high accuracy, this thesis initially details the procedure for developing a MATLAB Simulink model derived from the FEA-based characterization of the SRM prototype which is used in further studies. Additionally, obtaining a linearized SRM model is crucial for controller design. This thesis details the procedure for obtaining the linearized SRM model.

Subsequently in the thesis, a novel SRM drive utilizing a Miller converter-fed SRM motor for medium-power applications with a single current sensor is proposed to reduce cost and improve performance. The literature offers a variety of control strategies for SRM drives, yet for medium-power applications, those equipped with a dedicated position sensor and employing a fixed control strategy based on a linearized transfer function hold particular relevance. Also, there is a notable absence of a comprehensive control development procedure in the existing literature. Moreover, there lies an opportunity to reduce costs by minimizing the number of current sensors necessary for controlling the SRM drive. The thesis offers a comprehensive control development, dynamic simulation, analysis, and experimental validation of the same. Speed and current controllers are designed using the K-factor method, and the efficacy of the proposed drive is rigorously evaluated across various operating modes in MATLAB Simulink. Additionally, a hardware prototype is developed and the digital control algorithm is implemented on the DSP microcontroller TMS320F28379D based on the designed controllers to further assess drive performance. The results obtained validate the robustness and dynamic performance of the proposed cost-effective SRM drive with single current sensor across variable speed, variable torque, and constant power modes of operation.

In the literature, the single-pulse control (SPC) of SRM is discussed for high-speed applications, operating at the fundamental switching frequency to reduce core and switching losses effectively. However, its suitability for wide speed control is limited due to significant torque ripple. To address this, extending the constant conduction period with v/f control can mitigate torque ripple by facilitating torque sharing during winding commutation. Nevertheless, this extended conduction angle may result in negative torque production and a lower torque-to-ampere ratio. This research conducts an analysis of conventional SPC, conventional v/f con-

trol, and the impact of a wider conduction angle on torque ripple and efficiency through simulation studies. Moreover, it investigates the effect of accelerated demagnetization on torque ripple and efficiency in v/f controlled SRM drives with a wider conduction angle. This thesis introduces a novel bidirectional dual-port Ćuk converter-fed SRM drive with accelerated demagnetization capability. In the proposed Ćuk converter-fed SRM drive, the magnetization voltage controls the speed and provides a decoupled higher demagnetization voltage, thus accelerating demagnetization. This facilitates reduced switching losses and core losses similar to those in SPC, while ensuring reduced torque ripple with a wider conduction period and a higher torque ampere ratio due to accelerated demagnetization. Additionally, the proposed system incorporated IOBC capability. In G2V mode, the converter is reconfigured to adopt a two-stage, non-isolated charger topology, comprising a diode bridge followed by a Ćuk converter in the reverse direction. Detailed control development and analysis are presented in the thesis. The proposed SRM drive with IOBC capability is validated through simulations and an experimental prototype. It demonstrates robust performance across various modes of operation and offers cost reduction and increased overall power density.

Existing literature identifies two types of IOBCs for SRM-based electric vehicles: one leveraging machine windings as inductors and the other not. While utilizing machine windings offers advantages like higher power density, it also introduces risks such as instantaneous torque pulsation. To ensure reliable utilization of machine windings as filter inductors, maintaining zero instantaneous torque (ZIT) during charging modes is imperative. This thesis extensively investigates the utilization of machine windings as filter inductors, highlighting potential benefits in terms of power density and cost reduction. In the literature, the issue of common-mode voltage in non-isolated IOBCs for SRM based EVs have not received much attention. Additionally, the SRM based IOBCs proposed in the literature have no bidirectional capability limiting the operating modes. Bidirectional capabilities for IOBCs enable versatile operating modes by allowing EVs to feed power back to the grid or other electrical loads. Additionally, the literature lacks detailed qualitative analysis of IOBCs using machine

windings as filter inductors, including the impact of even harmonics from unequal inductances in positive and negative cycles. This thesis introduces a IOBC system with bidirectional capability for a 4-phase SRM drive based EV. In the proposed drive outlined in the thesis, the converter is reconfigured as a two-phase interleaved totem pole PFC converter, utilizing machine windings as filter inductors. This configuration enables the suppression of common-mode voltage or current and higher efficiency compared to previously reported IOBCs, without the need for additional magnetic contactors. During charging, four stable ZIT positions are identified, ensuring reliable utilization of machine windings as filter inductors, thereby mitigating wear and tear induced by torque pulsations. The thesis provides a detailed analysis of instantaneous torque during charging modes, supported by FEA and MATLAB simulation results to validate ZIT. This versatile IOBC demonstrates bidirectional capability, accommodating various operational modes such as G2V, V2G, V2H, and V2L. The performance of the proposed system is further validated through an experimental prototype, affirming the advantages of the proposed IOBC, which utilizes SRM windings as filter inductors, promising versatile operating modes with bidirectional capability and reduced common-mode voltage.

In conclusion, this thesis presents a comprehensive exploration of utilizing SRMs in EVs and the integration of IOBCs to enhance efficiency and functionality. Through simulation studies and experimental validation, novel solutions for SRM drives and IOBC systems for SRM based EVs are proposed, addressing challenges such as torque ripple, efficiency, and cost. The results demonstrate robust performance and validate the advantages of the proposed systems, paving the way for advancements in sustainable transportation solutions.

Contents

Abstract	i
List of figures	ix
List of tables	xv
List of abbreviations	xvii
List of symbols	xix
1 Introduction	1
1.1 Background and Motivation	1
1.1.1 Electric Vehicles (EVs)	1
1.1.2 Switched Reluctance Motor (SRM)	2
1.1.3 On-board chargers	3
1.2 Operation of SRM	4
1.2.1 Principle of Operation of SRM	4
1.2.2 SRM Drive	8
1.3 Detailed Literature Survey	9
1.3.1 Cost effective SRM drive for medium power applications	9
1.3.2 Enhancement of efficiency and effect of higher demagnetization voltage	12
1.3.3 SRM Drive with Integrated On-board Charging Capability	13
1.4 Conclusions	16
1.5 Research Objectives	18
1.6 Organization of Thesis	19
2 Simulation Model and Linear Model for Controller Design	21
2.1 Modeling of SRM for Simulation	21
2.1.1 Characterization of SRM	22
2.2 Derivation of System Linear Model	26

2.2.1	Small signal model of SRM Motor	26
2.3	Conclusions	28
3	Digital Control Development for Four-Phase SRM Drive using Single Current Sensor	29
3.1	Proposed System	29
3.2	Selection of Conduction Angle	33
3.2.1	System Transfer Function	34
3.3	Controller Design and Implementation	35
3.3.1	K Factor Method	35
3.3.2	Descretization of Controllers and Integral Anti-windup using Back Calculation Method	37
3.4	Simulation Results	39
3.5	Experimental Implementation: Results and Discussion	43
3.5.1	Control Algorithm	43
3.5.1.1	Calculation of position and speed	44
3.5.1.2	Current sensing	44
3.5.1.3	Speed and current low pass filters	44
3.5.1.4	Speed and current controllers	47
3.5.1.5	Phase Current Control	47
3.5.2	Results and Discussion	47
3.6	Conclusions	50
4	Ćuk Converter-fed SRM Drive with Accelerated Demagnetization and Integrated On-board Charging Capability for EVs	53
4.1	Conventional SPC and Effect of Higher Demagnetization Voltage	54
4.2	Proposed SRM Drive	59
4.2.1	Motoring and regenerative braking modes	60
4.2.2	Grid-to-Vehicle (G2V) charging mode	61
4.3	Front-end Converter Design	63
4.4	Control Design	64
4.4.1	Motoring mode	64
4.4.1.1	System transfer function	65
4.4.1.2	Design of current and speed controller	67
4.4.1.3	Selection of conduction angle	68

4.4.2	G2V charging mode	69
4.4.3	Derivation of system model	70
4.4.4	Design of voltage and current controller	71
4.5	Simulation Results	72
4.5.1	Motoring Mode	72
4.5.2	Grid to Vehicle Mode	74
4.6	Experimental Results	76
4.6.1	Motoring mode	77
4.6.2	G2V mode	78
4.7	Conclusions	80
5	A Bidirectional Interleaved Totem Pole PFC-based IOBC for EV SRM Drive	81
5.1	Proposed System	82
5.1.1	Motoring and Regenerative Braking Modes	82
5.1.1.1	Operating Modes	82
5.1.1.2	Control Design	83
5.1.2	Charging (G2V and V2G) modes	84
5.1.2.1	Operating Modes	84
5.1.2.2	Control Design	86
5.2	Discussion on instantaneous torque and variation of inductance during charging modes	87
5.2.1	Ansys Transient Analysis: Results and Discussion	88
5.2.2	Inductance values during charging mode	89
5.2.3	Matlab Simulations: Results and Discussion	91
5.3	Experimental Results	93
5.3.1	Motoring Mode	94
5.3.2	G2V and V2G modes	94
5.4	Conclusions	98
6	Conclusion and Future Scope	101
6.1	Conclusions and Contributions of the Thesis	101
6.2	Future Research Prospects	103
	Bibliography	105

List of Figures

1.1	Illustrative block diagram showing SRM drive with integrated on-board charging capability.	3
1.2	Illustrative cross-sectional view of a four-phase 8/6 SRM	5
1.3	Illustrative per phase inductance profile of SRM	6
1.4	Illustrative inductance profile, phase current, and torque of an SRM in motoring mode and generating mode.	6
1.5	Illustrative cross-section of a four-phase 8/6 SRM with the excitation sequence for counterclockwise (CCW) rotor rotation. (a) Phase A excited. (b) Phase B excited. (c) Phase C excited. (d) Phase D excited.	7
1.6	Conventional asymmetric H-bridge (AHB) converter fed SRM drive.	8
1.7	Modes operation for Phase A in AHB converter fed SRM drive.	8
2.1	Detailed simulation model of the SRM. (a) Per phase SRM electrical model. (b) Mechanical model.	21
2.2	The downsampled flux characteristics obtained from SRM characterization using Ansys as in (2.3).	23
2.3	Three-dimensional LUT showing phase current versus flux and rotor angle obtained by inverse interpolation of the flux characteristics as in (2.4).	24
2.4	The downsampled torque characteristics obtained as in (2.6)	25
2.5	Three-dimensional LUT showing electromagnetic torque generated versus phase current and rotor angle obtained as in (2.6).	25
2.6	Block diagram for the speed control of the proposed SRM drive.	26
3.1	The circuit configuration of the proposed Miller converter fed the SRM drive utilizing a single current sensor.	30

3.2	The block diagram depicting the control logic for the proposed SRM drive.	31
3.3	Three operating states of phase A during the motoring mode. (a) Magnetization mode. (b) Zero voltage mode. (c) Demagnetization mode.	32
3.4	The conduction period of 15° shown in torque vs rotor angle characteristic.	33
3.5	The control block diagram for the SRM drive utilizing single current sensor.	33
3.6	Bode plot of the current controller, G_{ci} (Type II Compensator)	35
3.7	Bode plots of plant transfer function (G_{pi}) and loop transfer function ($G_{pi} \cdot G_{ci}$) for closed-loop current control.	36
3.8	Bode plot of the speed controller, G_{ω_m} (Type II Compensator). . . .	36
3.9	Bode plots of plant transfer function ($G_{p\omega_m}$) and loop transfer function ($G_{p\omega_m} \cdot G_{\omega_m}$) for closed-loop speed control.	37
3.10	Discretized current controller model.	38
3.11	Discretized speed controller controller model with saturation and integral windup.	39
3.12	Simulation results showing phase currents, phase torques, and net torque at 2000 rpm.	39
3.13	Drive characteristics obtained from simulation analysis showing output torque, output power, efficiency, and torque ripple across a wide range of speed.	40
3.14	Simulation results showing reference speed, speed, load torque and output torque during dynamic step changes in speed reference at constant load torque.	41
3.15	Simulation results showing reference speed, speed, load torque and output torque during dynamic step changes in speed reference in constant power region above base speed.	41
3.16	Simulation results showing reference speed, speed, load torque and output torque during dynamic step changes in load torque at constant speed reference of 2000 rpm.	42
3.17	Photograph of the experimental setup.	42
3.18	Flowchart of the control implementation within Timer ISR.	46

3.19	Experimental results showing steady state voltage and current waveforms. (a) Phase voltage and phase current at 1200 rpm at rated load. (b) electrical angle, phase currents, and current through magnetization path at 1500 rpm at rated load.	48
3.20	Experimental results showing transient speed waveforms and current through the magnetizing path (i_{mag}). (a) Transient waveforms for a step change in speed reference from 0 to 1200 rpm. (b) Transient waveforms for a step change in speed reference from 1400 to 400 rpm.	48
3.21	Experimental results showing speed waveforms and current through the magnetizing path (i_{mag}) during dynamic changes. (a) Dynamic waveforms for step changes in reference speed (1500 rpm, 500 rpm, and 1000 rpm). (b) Waveforms for dynamic changes in the load torque.	49
4.1	Theoretical waveforms showing variations in per phase inductance, voltage, and current with machine rotor angle for different demagnetization voltages.	54
4.2	Simulation results for conventional SPC with variable conduction angle for controlling speed at different speeds of SRM drive. (a) Speed of 1000 rpm. (b) Speed of 1500 rpm. (c) Speed of 2000 rpm.	56
4.3	Simulation results for v/f control with constant conduction period (18.25°) and demagnetization voltage equal to the magnetization voltage at different speeds of the SRM drive. (a) Speed of 1000 rpm. (b) Speed of 1500 rpm. (c) Speed of 2000 rpm.	57
4.4	Simulation results for v/f control with constant conduction period (18.25°) and higher demagnetization voltage at different speeds of the SRM drive. (a) Speed of 1000 rpm. (b) Speed of 1500 rpm. (c) Speed of 2000 rpm	58
4.5	Configuration of the proposed onboard power converter for the SRM Drive-based EV with integrated onboard charging capability (Switch S closed at position M for motoring mode and position C for charging mode).	59
4.6	Modes of operation of the Čuk converter in motoring mode. (a) When T_1 is ON and T_2 is OFF. (b) When T_1 is OFF and T_2 is ON.	60

4.7	Modes of operation for one phase of SRM converter in motoring mode. (a) Magnetization mode. (b) Demagnetization mode.	61
4.8	Converter in grid-to-vehicle battery charging (G2V) mode	62
4.9	Operating modes of the power converter in grid-to-vehicle (G2V) bat- tery charging mode. (a) When T_2 is ON and T_1 is OFF. (b) When T_2 is OFF and T_1 is ON.	62
4.10	Control logic block diagram for motoring mode.	64
4.11	Control block diagram for the SRM drive in the motoring mode	65
4.12	Bode plots of uncompensated and compensated systems. (a) Current control loop: plant transfer function (G_{pi}) and loop transfer function ($G_{pi} \cdot G_{ci}$). (b) Speed control loop: plant transfer function ($G_{p\omega}$) and loop transfer function ($G_{p\omega} \cdot G_{c\omega}$) for closed-loop speed control.	68
4.13	Plots showing the effect of variation in conduction angle. (a) Induc- tance profile of phase A showing the conduction angle of 18.25° . (b) Plot showing efficiency and torque ripple for various conduction angles. . . .	69
4.14	Control block diagram for constant current and constant voltage modes of operation in G2V charging mode	69
4.15	Control model block diagram for constant voltage mode of operation in G2V charging mode	70
4.16	Bode plots of uncompensated and compensated systems for G2V mode. (a) Current control loop: plant transfer function (G_{gi}) and loop transfer function ($G_{gi} \cdot G_{gci}$). (b) Speed control loop: plant transfer function (G_{gpv}) and loop transfer function ($G_{gpv} \cdot G_{gcv}$) for closed-loop voltage control in CV mode.	72
4.17	Simulation results showing the voltage output of the Čuk converter ($V_{\acute{c}uk}$), rotor speed generated electromagnetic torque during dynamic operating conditions. (a) Step variations in speed reference (2000 rpm, 1000 rpm, 500 rpm, and 1500 rpm) at constant rated torque. (b) Step variations in speed reference above base speed (2000 rpm, 4000, rpm, 2500 rpm, and 3000 rpm) in constant power mode. (c) Step variations in load at constant speed. (d) Step variation in input battery voltage (100 V, 80 V, 120 V) at rated speed and torque.	73

4.18	Simulation results showing grid voltage, grid current, battery voltage, battery current in G2V charging mode in dynamic conditions. (a) Dynamic variations in input grid voltage (220 V, 170 V, and 270 V). (b) Dynamic Variations in input current in slow charging in CV mode.	74
4.19	Simulation results showing THD for different reference currents. (a) 5 A (b) 3.67 A (c) 2.5 A.	75
4.20	Photograph of the experimental setup.	76
4.21	Experimental results showing the operational waveforms in motoring mode at 1400 rpm. (a) Phase A voltage and current. (b) Rotor position and phase currents. (c) Input battery current and inductor current. .	77
4.22	Experimental results depicting speed and input inductor current (i_{L1}) waveforms during motoring mode across various operating conditions. (a) Step reference speed variations (1100 rpm, 700 rpm, 1400 rpm). (b) Constant speed operation at 1300 rpm with variations in load torque. (c) Constant speed operation at 1000 rpm under variations in input battery voltage through 80 V, 100 V, and 120 V.	77
4.23	Experimental results showing grid voltage, grid current, and battery current in G2V charging mode for constant grid current at different grid voltages. (a) $V_{grid}=220V$. (b) $V_{grid}=200V$. (c) $V_{grid}=170V$	78
4.24	Experimental results showing grid voltage, grid current, and battery current in G2V charging mode for different reference grid currents at grid voltage of 220V. (a) $I_{grid}=4A$. (b) $I_{grid}=3A$. (c) $I_{grid}=2A$	79
4.25	Experimental results showing power quality analyzer result showing THD for reference current of 4A.	79
5.1	Circuit configuration for the proposed SRM drive.	82
5.2	Three operating states of phase A during the motoring and regenerative braking modes. (a) Magnetization mode. (b) Zero voltage mode. (c) Demagnetization mode.	83
5.3	Circuit configuration of the power converter during charging mode (re-configured version of the circuit in Figure 5.1.	84

5.4	Operating modes for phase A winding in G2V/V2G modes. (a) While T_2 is turned on during the positive cycle. (b) While T_2 is turned off during the positive cycle. (c) While T_1 is turned on during the negative cycle. (d) While T_1 is turned off during the negative cycle.	85
5.5	Control block for G2V (positive current reference) and V2G (negative current reference) modes.	86
5.6	FEA results depicting (a) rotor trajectory with arbitrary initial position plotted along with inductance and torque profiles. (b) Phase inductance profile of the SRM for different phase currents.	88
5.7	Anslys FEA results showing flux lines at the stable positions. (a) Stable Position I (7.5°) (b) Stable Position II (22.31°) (c) Stable Position III (37.5°) (d) Stable Position IV (52.69°)	90
5.8	Simulation results showing input grid voltage, grid current, inductor currents, A-phase and C-phase torques, and net torque for stable positions. (a) Position I. (b) Position II. (c) Position III. (d) Position IV.	92
5.9	Photograph of the experimental setup.	93
5.10	Experimental results during motoring mode. (a) Steady-state speed and phase (phase A) current at a speed of 300 rpm. (b) Steady-state speed and phase (phase A) current at a speed of 500 rpm. (c) Speed transient for increasing speed reference from 0 to 800 rpm. (d) Speed transient for decreasing speed reference from 800 to 300 rpm. (e) Speed for variable speed references.	95
5.11	Experimental results showing waveforms in G2V/V2G modes for a grid reference current of 4 A. (a) Grid voltage and duty cycles for T_2 and T_6 . (b) PLL output, inductor currents (i_A and i_C), and grid current (i_{Grid}). (c) Voltage across T_2 and T_6 . (d) Battery voltage (V_{bat}) and battery current.	96
5.12	Experimental results showing grid voltages and current waveforms in G2V/V2G modes for different reference grid currents. (a) 1.4 A. (b) 2.83 A. (c) 4.6 A. (d) 5.3 A. (e) -2.12 A. (f) -3.18 A. (g) -3.9 A. (h) -5.2 A.	97
5.13	Efficiency vs load curve obtained from experimental results.	98

List of Tables

2.1	Machine parameters.	23
5.1	Table showing the switching states and sensor used for each phase during motoring and regenerative braking modes.	84
5.2	Comparison of different IOBCs utilizing machine windings as filter inductors for SRM based EVs	99

List of Abbreviations

AC	Alternating Current
DC	Direct Current
OEM	Original Equipment Manufacturer
IM	Induction Motor
PM	Permanent Magnet
IGBT	Insulated-Gate Bipolar Transistor
MOSFET	Metal-Oxide-Semiconductor Field-Effect Transistor
PWM	Pulse Width Modulation
RMS	Root Mean Square
EV	Electric Vehicle
LPF	Low Pass Filter
ICE	Internal combustion Engine
SRM	Switched Reluctance Motor
OBC	On-board Charger
IOBC	Integrated On-board Charger
V2G	Vehicle-to-Grid
V2H	Vehicle-to-Home
G2V	Grid-to-Vehicle
AHB	Asymmetric H-bridge
NPC	Neutral Point Clamped
CCW	Counter-clockwise
FEA	Finite Element Analysis
PLL	Phase Locked Loop
DSP	Digital Signal Processor
DITC	Direct Instantaneous Torque Control
DTC	Direct Torque Control
TSF	Torque Sharing Function
SPC	Single Pulse Control
PFC	Power Factor Correction
VSR	Voltage Source Rectifier
ZIT	Zero Instantaneous Torque
DBR	Diode Bridge Rectifier

LUT	Look-up Table
PWM	Pulse Width Modulation
PPR	Pulses per revolution
DSO	Digital Storage Oscilloscope
DAC	Digital-to-Analog Conversion
ADC	Analog-to-Digital Conversion
FW	Freewheeling
CV	Constant Voltage
CC	Constant Current
SOGI	Second-order Generalized Integrator
THD	Total Harmonic Distortion

List of Symbols

V_{DC}	DC-link voltage
v_{ph}	Phase voltage
i_{ph}	Phase current
R_s	SRM stator winding resistance
ψ_{ph}	Flux linkage with the rotor
θ_m	Mechanical rotor angle
L_{ph}	Inductance per phase
E_b	Back-emf
T_{ph}	Torque per phase
J	Moment of Inertia
B	Coefficient of Friction
L_u	Unaligned Phase Inductance
L_a	Aligned Phase Inductance
β_s	Stator pole arc angle
β_r	Rotor pole arc angle
W	Energy
T_l	Load torque
G_i	Current to phase voltage transfer function of SRM
G_m	Speed to phase voltage transfer function of SRM
G_{ω_m}	Speed to phase current transfer function of SRM
i_{mag}	Magnetization path current
ω_{ref}	Speed reference
ω_m	Rotor speed
i_{ref}	Current reference
d	Duty cycle
G_c	Converter transfer function
G_{fi}	Current feedback LPF transfer function
τ_{fi}	Current LPF corner frequency
$G_{f\omega_m}$	Speed feedback LPF transfer function
$\tau_{f\omega_m}$	Speed LPF corner frequency
G_{pi}	Plant transfer function for current controller design

$G_{p\omega_m}$	Plant transfer function for speed controller design
G_{ci}	Current controller transfer function
A_i	Current controller gain
ω_{zi}	Current controller zero
ω_{pi}	Current controller pole
$G_{c\omega_m}$	Speed controller transfer function
A_i	Speed controller gain
ω_{zi}	Speed controller zero
ω_{pi}	Speed controller pole
A_i	Current controller gain
ω_{zi}	Current controller zero
k_w	Integral anti-windup constant
v_{dmag}	Demagnetization voltage
$V_{\acute{c}uk}$	Output voltage of the Ćuk converter
V_{bat}	Battery voltage

Chapter 1

Introduction

1.1 Background and Motivation

1.1.1 Electric Vehicles (EVs)

The transportation sector accounts for a significant portion of global energy consumption, with a notable reliance on internal combustion engines (ICE) fueled by fossil fuels. As a result, this sector is a major contributor to greenhouse gas emissions and air pollution, which have detrimental effects on climate change and public health. To address these environmental challenges, there is a growing recognition of the need to transition toward electric vehicles (EVs).

Diversifying energy sources and increasing the share of renewable energy in electricity generation is vital to reduce the life cycle emissions of EVs. Advancements in battery technology and power electronics have been instrumental in driving the interest in electrified powertrains. These technological improvements have led to enhanced performance, efficiency, and reliability of EVs, making them a viable and competitive alternative to ICE vehicles. EVs offer various advantages, including lower maintenance costs, quieter operation, and improved acceleration due to the instant torque provided by electric motors.

However, challenges remain in the widespread adoption of EVs. One primary concern is the limited driving range of certain EV models compared to traditional vehicles fueled by gasoline or diesel. While technological advancements have contributed to increasing the range of EVs, addressing range anxiety is crucial to ensure wider consumer acceptance and confidence in EVs' capabilities. Another obstacle

is the higher upfront cost of EVs compared to internal combustion engine vehicles. Although the total cost of ownership, including fuel and maintenance expenses, tends to be lower for EVs over time, the initial purchase price can be a deterrent for some consumers. Governments and industry stakeholders are actively pursuing measures such as financial incentives, subsidies, and ongoing advancements in technology to reduce costs and make EVs more affordable and accessible to a broader population. To accelerate the transition to sustainable transportation, governments and original equipment manufacturers (OEMs) are increasing their investments in research and development efforts [Outlook \(2021\)](#).

1.1.2 Switched Reluctance Motor (SRM)

The most popular choices of motors for electric vehicles (EVs) are permanent magnet (PM) motors and Induction Motors (IM) due to their high power density, efficiency, reliability, and mature technology [Zhu and Howe \(2007\)](#), [Rahman et al. \(2000\)](#), [Zeraoulia et al. \(2006\)](#). In the early stages of EV development, Direct Current (DC) machines were widely used for traction, but they were later replaced by Induction Motors (IM) for their superior efficiency and reliability. Subsequently, Permanent Magnet (PM) motors emerged as the preferred choice over Induction Motors (IM) for EVs. PM motors offer higher power density and efficiency compared to IMs, contributing to improved performance and extended driving range for electric vehicles [Chau et al. \(2008\)](#), [Zhu and Howe \(2007\)](#), [Zeraoulia et al. \(2006\)](#), [Rahman et al. \(2000\)](#). However, the production of permanent magnets with high flux density requires rare earth minerals, such as neodymium (Nd) and dysprosium (Dy), which poses environmental and social concerns due to the extraction and processing methods involved. Additionally, rare earth minerals are unevenly distributed across the globe, leading to geopolitical issues that can impact the supply chain for these essential motor components [Bilgin et al. \(2019\)](#), [de Santiago et al. \(2012\)](#), [Boldea et al. \(2014\)](#).

To address the environmental and supply chain concerns associated with rare earth minerals, researchers and manufacturers have been exploring alternative magnet compositions. One such alternative is the use of ferrite magnets, which are more abundant and less reliant on rare earth minerals. However, ferrite magnets may have inferior magnetic properties compared to rare-earth magnet machines, potentially impacting

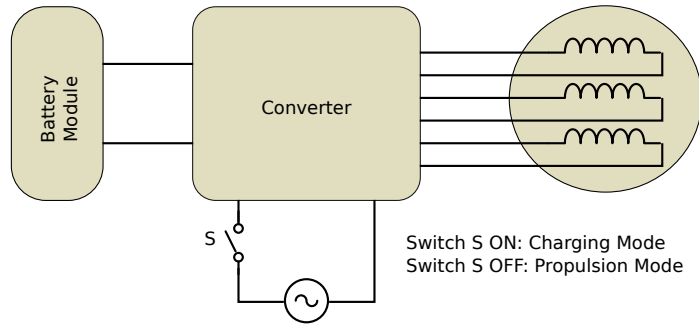


Figure 1.1: Illustrative block diagram showing SRM drive with integrated on-board charging capability.

overall motor performance [Boldea et al. \(2014\)](#), [Cai et al. \(2014\)](#), [Moghaddam and Gyllensten \(2014\)](#).

The Switched Reluctance Motor (SRM), by contrast, has a simple construction with a doubly salient structure. Its rotor, made entirely of laminated steel, lacks permanent magnets and copper bars, enhancing its reliability. SRMs are highly efficient under harsh conditions, unlike PM motors, whose magnetic properties degrade at high temperatures. Additionally, SRMs do not require field weakening at speeds above the base speed, which is necessary for PM motors. SRMs also offer superior fault tolerance—if one phase fails, the motor can continue to operate using the remaining phases, although with reduced performance. Moreover, the absence of rotor windings reduces rotor losses, further improving efficiency [Bilgin et al. \(2020\)](#). As a result, SRMs provide greater ruggedness and efficiency compared to IMs [de Santiago et al. \(2012\)](#), [Bilgin et al. \(2020\)](#), [Yang et al. \(2015\)](#), [Bostanci et al. \(2017\)](#), making them a promising alternative that could contribute to more affordable and efficient electric vehicles for consumers.

1.1.3 On-board chargers

Chargers used for electric vehicles can be categorized as either off-board chargers or on-board chargers. Off-board chargers are commonly used for fast charging as they can be connected to a higher-power grid and are not constrained by the size and weight limitations of the vehicle. On-board chargers (OBCs), while often used for slow or regular charging, can also support fast charging. However, OBCs must contend with limitations in size, space, and weight, as well as consider grid capacity constraints to prevent overloading the AC power grid during charging [Yilmaz and Krein \(2013\)](#).

While off-board charging infrastructure, such as public fast-charging stations, is still being developed, on-board chargers provide the convenience of charging the vehicle directly from available electrical outlets, making them suitable for regular commutes within the vehicle’s battery range or in areas where off-board charging options are limited [Yilmaz and Krein \(2013\)](#).

The traditional OBC typically comprises two dedicated power converters for motor driving and charging. In contrast, as shown in [Figure 1.1](#), integrated on-board chargers (IOBCs) combine these functionalities, resulting in cost savings, reduced complexity, and increased power density of the overall system [Yilmaz and Krein \(2013\)](#), [Metwly et al. \(2020\)](#), [Na et al. \(2019\)](#), [Khaligh and Dantonio \(2019\)](#). Also, on-board chargers with bidirectional capabilities can not only charge the vehicle’s battery from an external power source but also allow the vehicle to feed power back to the grid or other electrical loads. This bidirectional capability is essential for vehicle-to-grid (V2G) and vehicle-to-home (V2H) applications, where the EV battery can serve as a storage system and supply power to the grid or home during peak demand or power outages [Khaligh and Dantonio \(2019\)](#), [Monteiro et al. \(2016\)](#), [Kwon and Choi \(2017\)](#).

However, transitioning from separate propulsion and charging systems to an integrated approach requires significant modifications to the vehicle’s electrical architecture, control systems, and layout. Adapting to existing charging standards and ensuring safety certification further complicates retrofitting IOBC systems into current EV models. Ongoing research is aimed at improving the practicality and adoption of these systems.

1.2 Operation of SRM

1.2.1 Principle of Operation of SRM

In a reluctance machine, torque is produced by the tendency of a ferromagnetic material (such as iron) to align itself in a magnetic field along the least reluctance path. [Figure 1.2](#) presents a cross-sectional view of a four-phase Switched Reluctance Machine (SRM) featuring 8 stator poles and 6 rotor poles. Both the rotor and stator have salient poles, resulting in a double salient structure. The rotor has no permanent magnets or conductors.

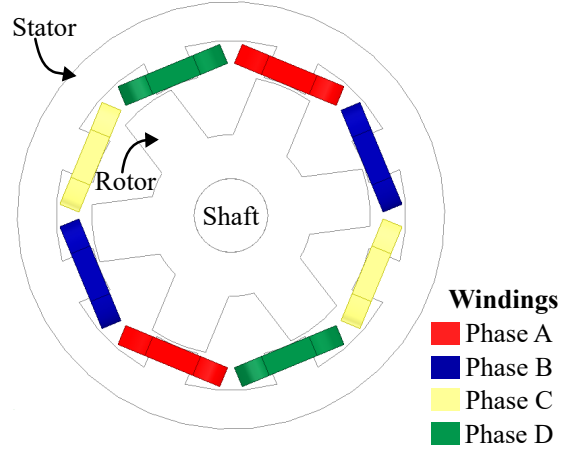


Figure 1.2: Illustrative cross-sectional view of a four-phase 8/6 SRM

The voltage equation for an SRM can be written as:

$$v_{ph} = i_{ph} R_s + \frac{d\psi_{ph}(i_{ph}, \theta_m)}{dt}. \quad (1.1)$$

Where v_{ph} , i_{ph} , R_s , ψ_{ph} , and θ_m are the phase voltage, phase current, stator winding resistance, and flux linkage with the rotor, mechanical rotor angle respectively. Ignoring the magnetic saturation, gives an ideal linear magnetization characteristic with phase current. Ignoring magnetic saturation, inductance of the phase can be assumed to be independent of current, hence can be represented as a function of rotor angle (θ_m). Hence, the flux linkage per phase is given by:

$$\psi(i_{ph}, \theta_m) = L_{ph}(\theta_m) i_{ph}(t) \quad (1.2)$$

Where the L_{ph} is the inductance per phase, θ is the rotor angle. From 1.1 and 1.2, the voltage equation can be derived as below:

$$v_{ph} = i_{ph} R_s + L_{ph}(\theta) \frac{di_{ph}(t)}{dt} + \omega i_{ph}(t) \frac{dL_{ph}(\theta)}{d\theta} \quad (1.3)$$

Where ω represents the speed of the rotor. Hence the back-emf (E_b) for SRM is given by:

$$E_b = \omega i_{ph}(t) \frac{dL_{ph}(\theta)}{d\theta} \quad (1.4)$$

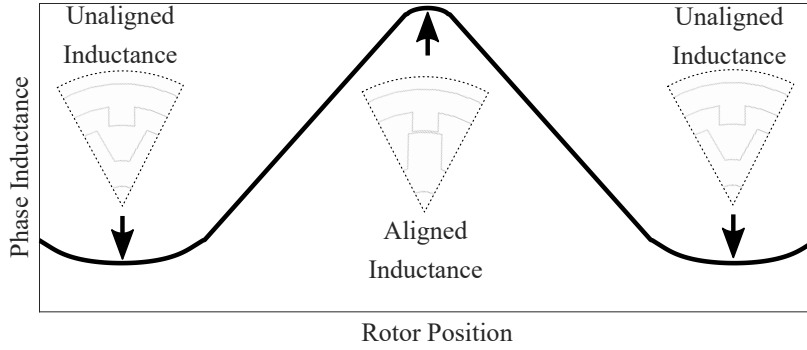


Figure 1.3: Illustrative per phase inductance profile of SRM

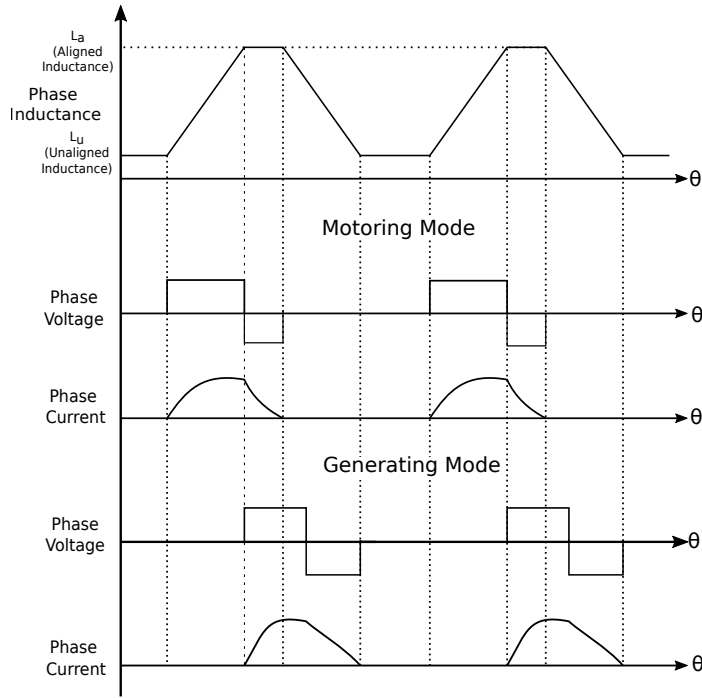


Figure 1.4: Illustrative inductance profile, phase current, and torque of an SRM in motoring mode and generating mode.

With the same assumption, the torque per phase can be derived as given below:

$$T_{ph} = \frac{1}{2} i_{ph}^2(t) \frac{dL_{ph}(\theta)}{d\theta} \quad (1.5)$$

From (1.5), it is evident that torque is directly proportional to the slope of the phase inductance and the square of the phase current. Figure 1.3 illustrates the inductance profile for one phase with respect to the rotor position. When the rotor moves from

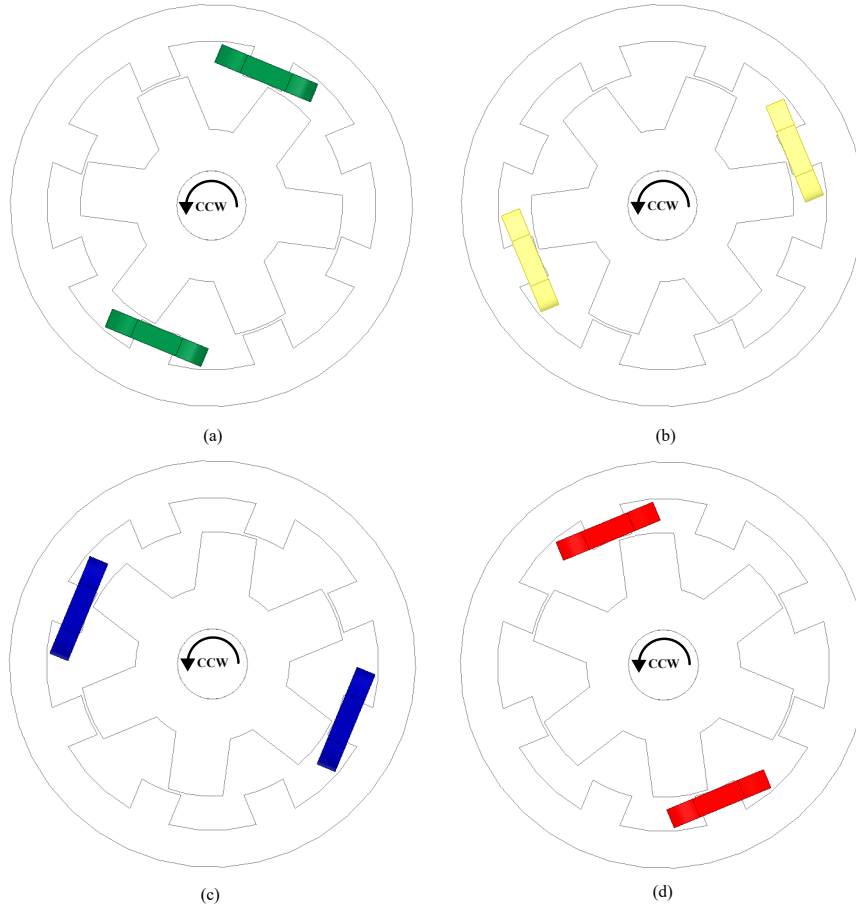


Figure 1.5: Illustrative cross-section of a four-phase 8/6 SRM with the excitation sequence for counterclockwise (CCW) rotor rotation. (a) Phase A excited. (b) Phase B excited. (c) Phase C excited. (d) Phase D excited.

an unaligned position to an aligned position, the phase inductance exhibits a positive inductance slope. Conversely, when the rotor moves from an aligned to an unaligned position, the phase inductance exhibits a negative inductance slope. The direction of torque, as derived from equation (1.5), depends on the slope of the inductance and is independent of the current direction, as shown in Figure 1.4.

To achieve continuous torque and rotation in a Switched Reluctance Machine (SRM), the phase windings must be excited in a specific sequence. Figure 1.5 illustrates the excitation sequence for continuous rotation in the counter-clockwise (CCW) direction. Initially, Phase A is excited until the rotor aligns along Phase A. Then, Phase D, which is closest to the rotor, is excited, followed by Phase C and Phase B. This sequence is repeated to enable continuous rotation of the SRM. In this instance,

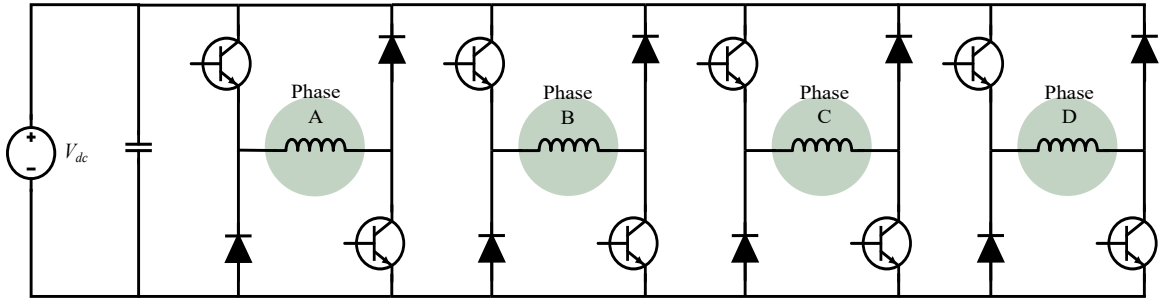


Figure 1.6: Conventional asymmetric H-bridge (AHB) converter fed SRM drive.

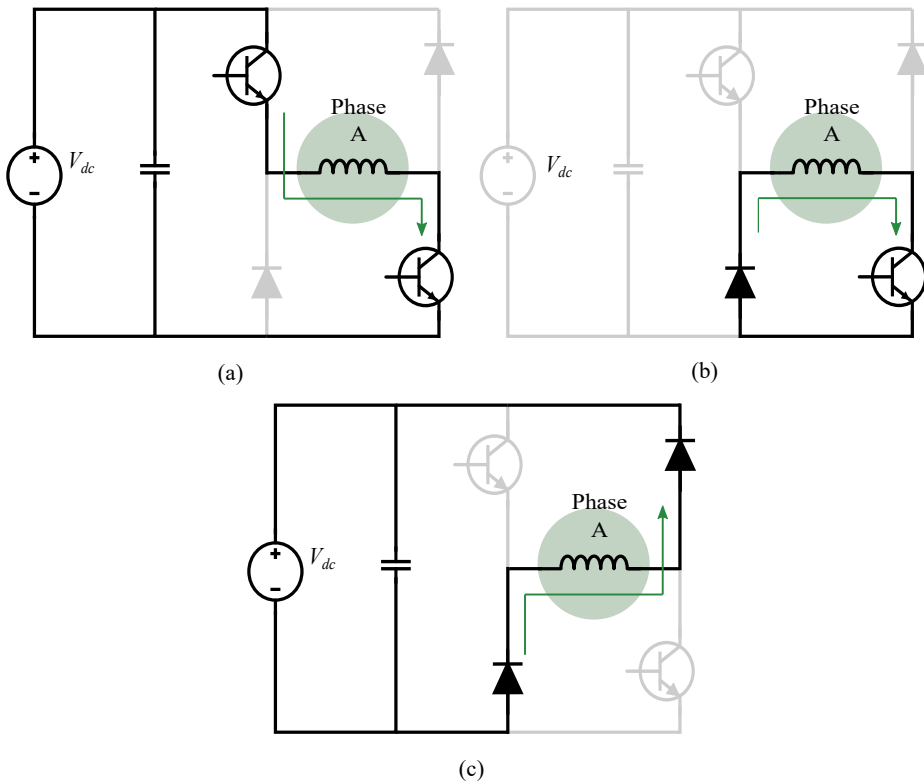


Figure 1.7: Modes operation for Phase A in AHB converter fed SRM drive.

the stator phase excitation sequence for CCW rotation is A-D-C-B. Conversely, for clockwise rotation, the phase sequence would be A-B-C-D.

1.2.2 SRM Drive

The drive system relies on knowing the rotor position to accurately excite the phases, ensuring proper torque generation. Additionally, the rotor speed can be estimated based on the rotor position for speed control. To achieve electronic commutation

and control, a power converter is essential. The power converter magnetizes and demagnetizes the phase windings based on the rotor position, regulating the current flow through the windings. As explained before, the direction of generated torque is independent of the direction of phase current as represented by (1.5).

Figure 1.6 illustrates the use of an asymmetric half-bridge circuit (AHB), a commonly employed choice for the power converter in SRM drives. This converter comprises two power electronic switches and two diodes, facilitating precise and independent control of each phase current, thus ensuring efficient operation. Figure 1.7 depicts the three operating modes of the AHB converter for phase A. When both switches connected to the phase are turned on, the input voltage $+V_{dc}$ appears across the winding to magnetize it. Subsequently, one switch is turned off, and the current in the phase decays through the diode and the remaining switch due to the winding resistance. Hence, the top switch is modulated to control the phase current in accordance with the reference current. Now during commutation, both switches are turned off, and the diodes conduct, applying $-V_{dc}$ across the windings for demagnetization while the next phase is excited.

1.3 Detailed Literature Survey

This section reviews literature in three key areas of SRM drives: cost-effective solutions for medium power applications, advancements in efficiency enhancement, and integrated on-board charging functionalities for EVs. Each subsection provides an overview of the pertinent literature, highlighting significant studies, methodologies, and findings within the respective domains. This survey offers insights into the latest developments and research trends shaping the field of SRM drives.

1.3.1 Cost effective SRM drive for medium power applications

In the context of medium power applications, optimizing both converter and control strategies is crucial within cost constraints, aiming to minimize costs without compromising drive performance. The asymmetric H-bridge (AHB) converter, a popular choice for SRM, with $2n$ switches and diodes for an n -phase SRM, offers advantages such as independent phase current control and faster demagnetization. Numerous

literature sources, such as [Bilgin et al. \(2019\)](#), [Krishnan \(2017\)](#), [Pires et al. \(2020\)](#) explore various converter configurations for SRM drives. [Peng et al. \(2017a\)](#) proposes an asymmetric three-level neutral point diode clamped converter for SRM drives which are typically useful for high power applications, since it has more number of switches than conventional AHB converter. Among these, the Miller converter [Pollock and Williams \(1990\)](#) stands out for its utilization of $2(n - 2)$ switches for an n -phase SRM. This topology maintains both phase independence and demagnetization efficiency, making it a notable choice for reduced switch SRM applications.

In addition to cost-effective converters, control methods with lower computational intensity and reduced memory requirements are crucial for medium-power applications. Minimizing the number of sensors is also imperative. While absolute position encoders are commonly used for precise rotor positioning in SRM control, position sensorless control strategies [Xiao et al. \(2022\)](#) offer alternatives. The SRM position-sensorless control typically relies on acquiring flux linkage or inductance, which vary with rotor position, to estimate the rotor position. In [Ye et al. \(2015a\)](#), an incremental-inductance estimation method for position sensing is analyzed. The implementation is simple but provides inaccurate position estimation at lower speeds. For accurate speed estimation across a wide range of speeds, a method employing high-frequency voltage injection during the idle phase is employed in [Pasquesoone et al. \(2011\)](#). However, this involves additional voltage injection power losses. These require a position lookup table based on flux linkage-position-phase current characteristics of the SRM. In [Peng et al. \(2017b\)](#), the 3D lookup table is obtained by numerical methods and a third-order phase-locked loop (PLL) is designed to reduce estimation error. These position sensorless schemes in [Ye et al. \(2015a\)](#), [Pasquesoone et al. \(2011\)](#), [Peng et al. \(2017b\)](#) require a 3D lookup table to be stored in the controller to estimate the position, taking up a significant amount of memory space. Additionally, position sensorless SRM control requires phase current measurement to estimate the phase inductance. In [Gan et al. \(2018b\)](#), a cost-effective current measurement technique for 4-phase SRM by split dual bus line without pulse injection and voltage penalty is proposed. An online sensorless position estimation for SRM using one current sensor is proposed in [Gan et al. \(2016\)](#). However, these methods demand higher memory space or computational capabilities, leading to a preference for dedicated position encoders in medium-power applications.

Considering current sensors, a conventional SRM drive typically employs n num-

ber of current sensors for an n -phase SRM motor. To overcome this issue, [Kumar et al. \(2023\)](#) suggests a v/f strategy, controlling the input voltage instead of phase currents and hence reducing the sensor count. However, this results in increased torque ripple. In [Xu et al. \(2019\)](#), the authors have proposed an innovative SRM drive with single and dual current sensors for the conventional AHB converter, addressing torque ripple. However, this work lacks detailed control development, and a systematic control design is missing.

In addition to prioritizing cost-effective converters and minimizing the number of sensors, control methods with lower computational intensity and reduced memory requirements are crucial for medium-power applications. Various control strategies for SRM drives have been proposed and developed in the literature, focusing on digital implementation with low-cost microcontrollers. For instance, in [Bose et al. \(1986\)](#), the authors designed and laboratory-tested a 5-hp SRM drive using an Intel 8751 microcomputer, known for its affordability as a digital controller. This work specifically featured the design and implementation of a speed or torque controller using current delta modulation. Similarly, the authors of [Samudio and Pillay \(1995\)](#) adopted the same control strategy for an SRM drive, employing delta modulation but implementing it on the TMS320C30 Digital Signal Processor (DSP). While the delta modulation PWM technique offers a fixed-frequency modulation method that is easy to implement in digital controllers, it comes with the drawback of increased current ripple due to fixed sampling intervals, potentially impacting motor performance and efficiency [Bae and Krishnan \(1996\)](#). Also, in [Bose et al. \(1986\)](#) and [Samudio and Pillay \(1995\)](#), the non-linear dynamic characteristics of SRM are not analyzed in detail to decide the conduction angle. [Ilic et al. \(1987\)](#) uses a non-linear analytical flux function to figure out the conduction angle. In this work, the authors have designed a non-linear state feedback controller to handle the non-linearities described by this function. However, often, the analytical flux function does not accurately align with actual motor dynamics.

In [Inderka and De Doncker \(2003\)](#), an innovative control strategy called direct instantaneous torque control (DITC) employing a torque hysteresis controller is proposed. However, this requires a pre-estimated rotor torque look-up table to calculate the instantaneous torque. A sliding mode DITC cruise control for SRM, where the turn-off angle is controlled using a minimum torque ripple point tracker, is proposed in [de Paula and Barros \(2022\)](#). However, both [Inderka and De Doncker \(2003\)](#) and

de Paula and Barros (2022) require prior torque characteristics stored in the microcontroller or computationally intensive online optimization techniques. This complexity makes them unsuitable for medium-power SRM drive applications. Current hysteresis control is another popular method implemented for SRM drives, where motor phase currents are controlled and regulated within a hysteresis band. Although effective in maintaining current within a desired band, its variable switching frequency poses challenges for digital implementation. The use of PI controllers mitigates the above-mentioned issue, operates the SRM drive with a fixed switching frequency, and ensures lower current ripple Peng et al. (2016). Additionally, using a linear controller makes it easier to utilize the PWM module in DSPs and synchronize with other control systems. Different fixed frequency control strategies for SRM drives are reviewed in Dhale et al. (2021). However, to the best of the authors' knowledge, there are no research papers in the literature that present a systematic approach to digital control development for an SRM drive using a single current sensor for medium-power applications.

1.3.2 Enhancement of efficiency and effect of higher demagnetization voltage

In the area of control of SRM drive, several torque-smoothing strategies have been proposed, including approaches based on direct and indirect torque control. These strategies encompass methods such as torque sharing function (TSF) approaches, direct torque control (DTC) Cheok and Fukuda (2002), Yan et al. (2019), and direct instantaneous torque control (DITC) Inderka and De Doncker (2003), Sun et al. (2021). While increasing the conduction angle can effectively reduce torque ripple during commutation, it may lead to negative torque, resulting in a lower torque-to-ampere ratio. To address this issue, an enhanced DITC scheme with modified vector tables has been proposed by Yan et al. Yan et al. (2019). However, many of the torque-smoothing strategies suggested in the literature tend to degrade the efficiency of SRM drives due to their operation at high switching frequencies with higher switching losses and core losses Ye et al. (2015b), Lee et al. (2009), Ralev et al. (2017).

To mitigate this efficiency loss, the single-pulse control (SPC) technique has been introduced, reducing the switching frequency to the fundamental frequency Ahmad

and Narayanan (2020). In this method, machine speed is controlled by adjusting the conduction angle. However, SPC may not be suitable for applications prioritizing smooth torque or low acoustic noise Klein-Hessling et al. (2014). Nevertheless, torque sharing between adjacent phases during commutation can effectively diminish torque ripple in SPC by widening the conduction angle for each phase. Yet, extending the conduction angle necessitates accelerated demagnetization to eliminate negative torque production Pires et al. (2020). Therefore, with accelerated demagnetization and a broader conduction angle, higher power density and lower torque ripple can be achieved, albeit at the cost of requiring a higher negative demagnetization voltage.

The paper Jain and Mohan (2005) introduces an AHB converter with a buck-boost converter in the demagnetization path to increase demagnetization voltage. This utilizes SPC, controlling the turn-off angle. However, torque ripple increases during commutation at lower speeds, limiting its suitability for wide-speed-range applications. Another proposal in Tang et al. (2021) suggests a drive topology for grid-connected applications, featuring a T-type single-phase three-level voltage source rectifier (VSR) based SRM drive, albeit with three switches and diodes per phase. Additionally, Chaurasiya et al. (2023) employs a reduced switch multilevel converter. Literature also explores SRM drives with higher demagnetization voltage for AC grid connections and power factor correction (PFC) Sadeghi et al. (2021), Mohamadi et al. (2018), but they involve high-frequency power converter switching Tang et al. (2021), Chaurasiya et al. (2023), Sadeghi et al. (2021), Mohamadi et al. (2018). Thus, there exists a gap in the literature concerning the simultaneous integration of fundamental switching (to enhance efficiency and reduce inverter cost), extended conduction period (to minimize torque ripple), and accelerated demagnetization (to improve torque-ampere ratio).

1.3.3 SRM Drive with Integrated On-board Charging Capability

Beyond control strategies, integrating on-board charging (IOBC) capability into electric vehicle (EV) drives can eliminate the need for a dedicated on-board charger, thereby reducing costs and improving system power density. This integration can be achieved by reutilizing the SRM converter and machine windings as filter inductors in charging mode Chang and Liaw (2011), Cai and Zhao (2021), Chen et al. (2019), Chen and Huang (2021) or by reutilizing the SRM converter and separate additional filter

inductor [Gan et al. \(2018a\)](#). While reutilizing the machine windings offers advantages in cost and weight savings, it can reduce efficiency and introduce pulsating torque during charging. This pulsating torque cannot be mitigated in SRM based IOBCs utilizing machine windings without disengaging the motor from the shaft. Additionally, in converter configurations [Chang and Liaw \(2011\)](#), [Cai and Zhao \(2021\)](#), [Chen et al. \(2019\)](#), [Chen and Huang \(2021\)](#), the front-end converter remains connected in motoring mode, which can degrade motoring efficiency.

Traditionally, OBCs are isolated from the grid, but non-isolated chargers hold the advantage of greater efficiency [Rivera et al. \(2023\)](#). However, they introduce potential safety concerns due to leakage current from common mode voltage, as discussed in [Zhang et al. \(2018\)](#). Recent research works have identified methods to mitigate common mode voltage in non-isolated on-board chargers, making them a viable option [Zhang et al. \(2019\)](#). In the literature, it is demonstrated that compared to various power factor correction (PFC) converter topologies (which is part of an OBC), the totem-pole PFC has a small common mode leakage current [Park et al. \(2019\)](#). Additionally, the totem pole PFC converter has higher efficiency, reduced ripple in the input AC current, and fewer components compared to the other PFC topologies [Park et al. \(2019\)](#).

As mentioned earlier, research exploring the use of SRM-based IOBCs in EVs is rapidly gaining traction. Specifically, studies presented in [Gan et al. \(2019\)](#), [Cheng et al. \(2020b\)](#), [Hu et al. \(2018\)](#), [Cheng et al. \(2020a\)](#) have delved into IOBCs for SRM-equipped Plug-in Hybrid EVs (PHEVs), while research works in [Hu et al. \(2015a\)](#), [Thankachan and Singh \(2020\)](#), [Hu et al. \(2016, 2015b\)](#), [Chang and Liaw \(2009, 2011\)](#), [Cai and Zhao \(2021\)](#), [Shah and Payami \(2021\)](#), [Chen et al. \(2019\)](#), [Shah and Payami \(2023\)](#), [Yu et al. \(2021\)](#) have investigated methodologies for SRM-equipped pure EVs.

Among the various IOBCs for SRM-equipped EVs, some have employed machine windings as filter inductors, achieving higher power density and an increased power rating for the OBC without significantly increasing system weight [Khaligh and Dantonio \(2019\)](#). However, utilizing machine windings as filter inductors can induce torque pulsation or rotor rotation during charging mode. Blocking the rotor during charging may not eliminate rotor vibrations and associated wear and tear in the machine. Even when the average torque is controlled to zero, pulsating torque may still exist, resulting in rotor vibrations and associated wear and tear [Bodo et al. \(2017\)](#). For example, the research presented in [Chang and Liaw \(2009, 2011\)](#) and [Cai and Zhao](#)

(2021) utilizes machine winding as a filter inductor during the input PFC stage. However, these methods have unequal current distribution across the machine windings during charging, leading to torque pulsation. To address this issue, research in [Hu et al. \(2015a\)](#), [Thankachan and Singh \(2020\)](#) has proposed using separate inductors instead of machine windings as filter inductors during charging mode. However, this approach increases cost and reduces power density.

To address the mentioned challenge, various innovative solutions have been proposed to achieve zero instantaneous torque (ZIT) using machine windings as filter inductors. For instance, the research in [Gan et al. \(2019\)](#) and [Cheng et al. \(2020b\)](#) aims to achieve ZIT for a three-phase SRM by ensuring equal current through all three machine windings. This, in contrast to the approaches in [Chang and Liaw \(2009, 2011\)](#) and [Cai and Zhao \(2021\)](#), gives 6 ZIT positions. However, the proposed topology is a two-stage topology, i.e., a diode bridge rectifier (DBR) followed by a three-phase PFC boost converter using machine windings. For higher efficiency, [Cheng et al. \(2020a\)](#) suggests a bridgeless boost converter with two phases connected in series during the charging mode. This configuration ensures four stable positions with ZIT during charging. However, it necessitates the use of two magnetic contactors for reconfiguration during charging, adding to the overall cost and bulkiness, especially when considering their automotive-grade expense. Furthermore, the converters in [Gan et al. \(2019\)](#), [Cheng et al. \(2020b\)](#) and [Cheng et al. \(2020a\)](#) lack bidirectional operation capability for OBCs.

The methods discussed in [Hu et al. \(2018, 2016\)](#) and [Hu et al. \(2015b\)](#) utilize SRM with split-phase windings to attain ZIT during the charging mode. In these approaches, one phase is split into two and excited during charging, providing two stable positions with ZIT. However, these methods require a specialized split-phase SRM and the incorporation of additional magnetic contactors for reconfiguration. The introduction of split-phase windings necessitates constructional modifications, and the inclusion of extra contactors adds to the overall expense and complexity of the system.

In [Chen et al. \(2019\)](#), [Yu et al. \(2021\)](#), a four-phase SRM is reconfigured into a bridgeless boost PFC converter without using any magnetic contactors. Both have four stable ZIT positions. However, both configurations have disparities in equivalent inductances in the positive and negative cycles. This leads to even harmonics in the grid current due to unequal current ripples in positive and negative cycles.

These even harmonics are mitigated in [Shah and Payami \(2023\)](#), with the same inductance in positive and negative cycles irrespective of the rotor position. Also, the charging methodology proposed in [Shah and Payami \(2023\)](#) has 8 stable ZIT positions. However, in [Shah and Payami \(2023\)](#), the conduction losses and switching losses are higher, with four windings and their respective semiconductor switches conducting simultaneously. Also, the converters discussed in [Gan et al. \(2019\)](#), [Cheng et al. \(2020b\)](#), [Hu et al. \(2018\)](#), [Cheng et al. \(2020a\)](#), [Hu et al. \(2015a\)](#), [Thankachan and Singh \(2020\)](#), [Chang and Liaw \(2009, 2011\)](#), [Hu et al. \(2016, 2015b\)](#), [Cai and Zhao \(2021\)](#), [Shah and Payami \(2021\)](#), [Chen et al. \(2019\)](#), [Yu et al. \(2021\)](#), [Shah and Payami \(2023\)](#) lack bidirectional operation capability for OBCs. Bidirectional operation capability for OBCs can facilitate versatile operating modes such as returning power back to the grid, supplying power to other loads, grid forming mode, and reactive power compensation [Monteiro et al. \(2016\)](#).

In [Yu et al. \(2021\)](#), the motor drive converter is reconfigured into a bidirectional single-phase totem-pole PFC converter for charging. The totem pole configuration enables the suppression of common mode voltage or current. However, the bidirectional operation is not detailed in the paper. Also, it requires two additional magnetic contactors. Additionally, in [Yu et al. \(2021\)](#), a conventional VSI is used to drive the motor, hindering independent control of phase currents with slower demagnetization in motoring mode.

The literature shows that the development of SRM-based OBCs for EVs has gained significant traction. However, existing OBC designs often face challenges in achieving ZIT with machine windings as filter inductance. These systems often involve trade-offs between cost, complexity, and performance. Addressing these limitations requires detailed analysis and further research into innovative topologies and control strategies.

1.4 Conclusions

This chapter provides an overview of the scope for electric vehicles and discusses the operating principles of Switched Reluctance Motor (SRM) drives. It reviews literature on the characterization, control, and design of high-speed SRMs and corresponding high-switching frequency power converters. In summary, this thesis addresses the following points:

1. Accurate simulation models are essential for simulation studies of SRM drives.

Various methods, from analytical approaches to electromagnetic Finite Element Analysis (FEA) tools, are available for characterizing SRMs. FEA-based models offer high accuracy, and linear controller design necessitates a linearized SRM model.

2. The literature offers a variety of control strategies for SRM drives, yet for medium-power applications, those equipped with a dedicated position sensor and employing a fixed control strategy based on a linearized transfer function hold particular relevance. Nevertheless, there is a notable absence of a comprehensive control development procedure in the existing literature. Moreover, there lies an opportunity to reduce costs by minimizing the number of current sensors necessary for controlling the SRM drive.
3. The single-pulse control of SRM, operating at fundamental frequency switching, effectively reduces core losses and switching frequency losses. However, its suitability for wide speed control is limited due to significant torque ripple. Extending the constant conduction period with v/f control can mitigate torque ripple by facilitating torque sharing during winding commutation. Nonetheless, this extension may lead to negative torque production and a lower torque-to-ampere ratio. Further research is essential to develop SRM drives with improved torque-to-ampere ratios and reduced torque ripple. Investigating accelerated demagnetization's effectiveness in eliminating negative torque, particularly when applied to v/f control with an extended conduction period, is an area that warrants deeper exploration.
4. There are two types of on-board chargers (OBCs) for SRM-based electric vehicles, one utilizing machine windings as inductors and the other not. Utilizing machine windings offers advantages in terms of higher power density but poses risks such as instantaneous torque pulsation. A detailed study into utilizing machine windings could provide higher power density and lower costs for SRM-based EVs. Additionally, non-isolated input-output bridge converters (IOBCs) for SRMs with reduced common-mode voltage and bidirectional capability have not received much attention in the literature. Qualitative analysis, including consideration of even harmonics due to unequal inductances, also requires further investigation.

1.5 Research Objectives

Based on the detailed literature review and future prospects in the area, the following research objectives have been identified:

1. **Develop Simulink models for simulation studies and linear models for control design.** Specific objectives for this aim include:
 - Obtain a nonlinear MATLAB Simulink model of the SRM based on FEA analysis for simulation studies.
 - Obtain a linearized SRM model neglecting core saturation to aid in controller design.
2. **Design and develop a novel SRM drive with reduced current sensors for medium-power applications.** Specific objectives include:
 - Investigate converter topologies with reduced power electronic devices for SRM drive.
 - Investigate cost-effective control strategies for SRM drive.
 - Propose a novel SRM drive employing a Miller converter with a single current sensor.
 - Develop control strategies, simulate, and experimentally validate the proposed drive.
3. **Study the effect of accelerated demagnetization in v/f control of SRM drives, aiming to enhance efficiency with fundamental switching of the SRM converter.** Specific objectives include:
 - Analyze conventional Single Pulse Control (SPC), conventional v/f control, and the effect of a wider conduction angle on torque ripple and efficiency through simulation studies.
 - Investigate the effect of accelerated demagnetization on torque ripple and efficiency in v/f controlled SRM drives with a wider conduction angle.
 - Propose a novel bidirectional dual-port Ćuk converter-fed SRM drive with integrated on-board charging capability and accelerated demagnetization.

- Design the front-end converter and the controller for motoring and charging modes, followed by simulation and experimental validation of the proposed SRM drive.
4. **Study the effect of utilizing machine windings as filter inductors during charging in SRM drives with IOBC capability.** Specific objectives include:
- Investigate the effect of rotor position on instantaneous torque and power factor when the machine winding is used as filter inductors during charging.
 - Propose an interleaved totem pole Power Factor Correction (PFC) based non-isolated single-stage IOBC utilizing machine windings as filter inductors with zero instantaneous torque, bidirectional capability, and reduced common mode voltage.
 - Perform simulation and experimental validation of the proposed drive with IOBC capability.

1.6 Organization of Thesis

The thesis comprises six chapters, each addressing important aspects of SRM drive for EVs with IOBC capability.

Chapter 2 discusses the development of simulation model for SRM utilizing FEA tool for motor characterization. The development of linearized model of SRM for controller design, is also explained in this chapter.

Chapter 3 presents a novel SRM drive employing a Miller converter-fed SRM motor with a single current sensor, featuring comprehensive control development, simulation, and experimental validation for the same.

Chapter 4 introduces a bidirectional dual-port Ćuk converter-fed SRM drive with integrated on-board charging capability, optimizing efficiency and reducing torque ripple through modified v/f control. It details control design and provides simulation and experimental validation.

Chapter 5 presents an interleaved totem-pole PFC based non-isolated IOBC for a 4-phase SRM drive utilizing SRM phase windings as filter inductors. Along with the increased power density of the system, the proposed IOBC features reduced common-mode voltage and bidirectional capability. The chapter presents detailed analysis of

instantaneous torque and effect of inductance variation with respect to rotor angle during charging modes. Simulation and experimental results are presented to validate effectiveness of the proposed system.

Chapter 6 presents the conclusions of the thesis with guidelines for future work.

Chapter 2

Simulation Model and Linear Model for Controller Design

This chapter outlines the development of the simulation model and linear model for the SRM used in the research. Firstly, it describes the procedure for obtaining a MATLAB Simulink model after characterizing the SRM using FEA tools, specifically Ansys Maxwell in this study. Additionally, it discusses the development of a linearized model for controller design. These models are useful in subsequent simulation and experimental studies.

2.1 Modeling of SRM for Simulation

SRMs inherently exhibit nonlinear characteristics, such as magnetic saturation and switching dynamics. For accurate simulations, it is essential to utilize an SRM model that encompasses its inherent nonlinearities. The block diagram depicting the SRM

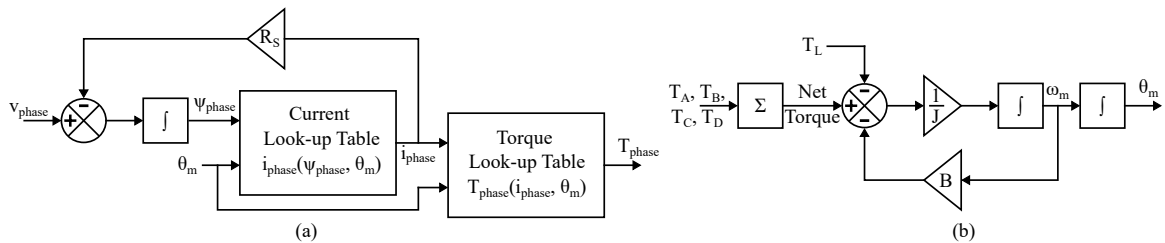


Figure 2.1: Detailed simulation model of the SRM. (a) Per phase SRM electrical model. (b) Mechanical model.

simulation model is shown in Figure 2.1. From the voltage equation for an SRM in (1.1), the flux per phase can be derived and is given by:

$$\psi_{ph} = \int_0^t (v_{ph} - i_{ph}R_s) dt. \quad (2.1)$$

Figure 2.1(a) shows the block diagram for the corresponding per-phase electrical model of the SRM. In this model, the flux linkage is calculated as per (2.1). Subsequently, the model incorporates a current look-up table (LUT), offering current values based on the respective flux linkage and rotor position. This is followed by an LUT that provides torque values corresponding to the given current and rotor position. In order to enhance the comprehensiveness and accuracy of the model depicted in Figure 2.1(a) and to develop a holistic simulation model, it is imperative to conduct a prior characterization of the SRM. The details of this characterization are provided in the subsequent section of this chapter.

The mechanical equation for the torque of the motor is given by

$$T_m = T_l + J \frac{d\omega_m}{dt} + B\omega_m. \quad (2.2)$$

Where T_m , T_l , ω_m , J , and B represent the generated torque, load torque, mechanical speed, the moment of inertia, and frictional coefficient of the motor, respectively. Figure 2.1(b) illustrates the corresponding mechanical model. The net generated torque (T_m) is the sum of the individual phase torques.

2.1.1 Characterization of SRM

Several methods exist for characterizing SRMs, ranging from analytical approaches to powerful electromagnetic Finite Element Analysis (FEA) tools. The analytical method, based on known parameters such as aligned inductance, unaligned inductance, maximum current, and maximum flux linkage, is extensively detailed in [Le-Huy and Brunelle \(2005\)](#), [Hannoun et al. \(2007\)](#). While analytical methods based on known parameters offer simplicity, they often struggle with the intricate nonlinearities inherent in SRMs [Bilgin et al. \(2019\)](#). For that reason, this work leverages Ansys Maxwell, a robust FEA tool, to achieve a more accurate and comprehensive characterization.

The characterization of the SRM begins with its design in Ansys RMxpert, utilizing

Table 2.1: Machine parameters.

Electrical Parameters		Geometrical Parameters	
Parameter	Value	Parameter	Value
Phases	4	Stator poles/rotor poles	8/6
Power	1 <i>hp</i>	Number of Turns	70 turns
Speed	2000 <i>RPM</i>	Length of Core	100 mm
Voltage, Current	380 <i>V</i> , 2.6 <i>A</i>	Stator Outer Diameter	100 mm
Stator Resistance (R_s)	1 Ω	Stator Inner Diameter	60 mm
Moment of Inertia (J)	0.00082 <i>kg.m²</i>	Length of Air Gap	0.5 mm
Coefficient of Friction (B)	0.001 <i>N.m.s</i>	Rotor Inner Diameter	19 mm
Unaligned Phase Inductance (L_u)	3.95 <i>mH</i>	Stator pole arc angle (β_s)	19.8°
Aligned Phase Inductance (L_a)	24.6 <i>mH</i>	Rotor pole arc angle (β_r)	24°

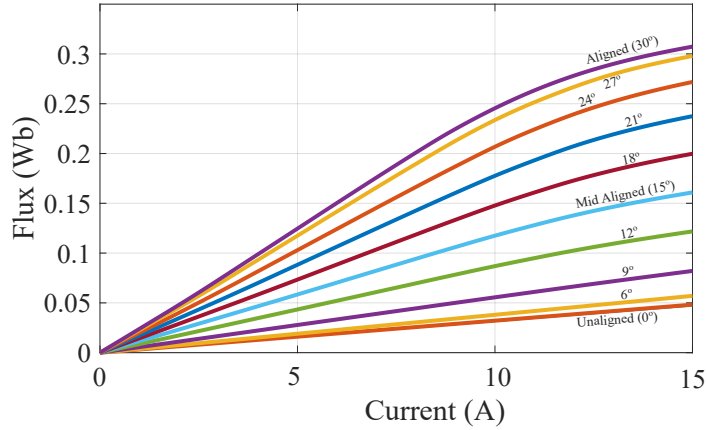


Figure 2.2: The downsampled flux characteristics obtained from SRM characterization using Ansys as in (2.3).

the geometrical parameters provided in Table 2.1. After the initial design phase, Finite Element Analysis (FEA) is conducted across a range of phase currents and rotor positions to capture the nonlinear electromagnetic behavior of the motor. This analysis yields flux linkage data as a function of both phase current (i_{ph}) and rotor position (θ_m). To ensure smooth and continuous modeling of the SRM's nonlinear characteristics, the obtained flux linkage data is interpolated, producing a smooth flux linkage surface that varies with current and rotor position. This interpolation ultimately provides a nonlinear function that represents the flux linkage (ψ_{ph}) as a function of both current and rotor position as:

$$\text{Phase Flux} = \psi_{ph}(i_{ph}, \theta_m). \quad (2.3)$$

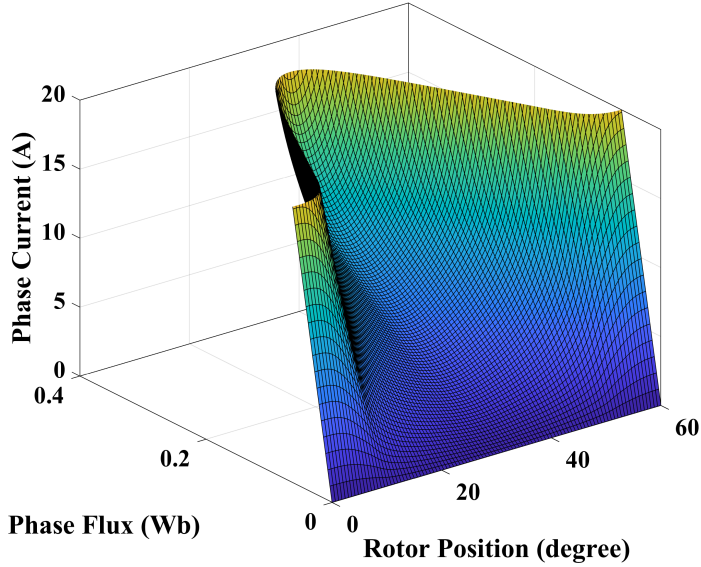


Figure 2.3: Three-dimensional LUT showing phase current versus flux and rotor angle obtained by inverse interpolation of the flux characteristics as in (2.4).

To enhance clarity and visual understanding, the dense interpolated flux data is down-sampled, and the resulting plot is presented in Figure 2.2.

With the non-linear flux-current-angle relationship established in (2.3), the phase current Look-Up Table (LUT) for the SRM model is derived. This LUT maps the required current for a given flux and rotor position. This LUT is obtained by performing inverse interpolation on the flux data in (2.3) for flux values ranging from zero to maximum flux. This determines the corresponding current required to achieve a flux for any given rotor position. Mathematically, this relationship is captured by Equation (2.4):

$$\text{Phase Current} = i_{ph}(\psi_{ph}, \theta_m). \quad (2.4)$$

The surface plot illustrating the current LUT obtained is depicted in Figure 2.3.

In SRM, for a given current, the incremental mechanical energy required for the rotor to traverse an angle corresponds to the area enclosed between the flux curves at the initial and final rotor positions. Dividing this energy by the angle of rotation provides the mechanical torque. Consequently, the flux data (in (2.3)) is integrated along the current vector to get the energy (W) function as:

$$W = \int_0^{i_{ph}} \psi_{ph}(i_{ph}, \theta_m) di_{ph}. \quad (2.5)$$

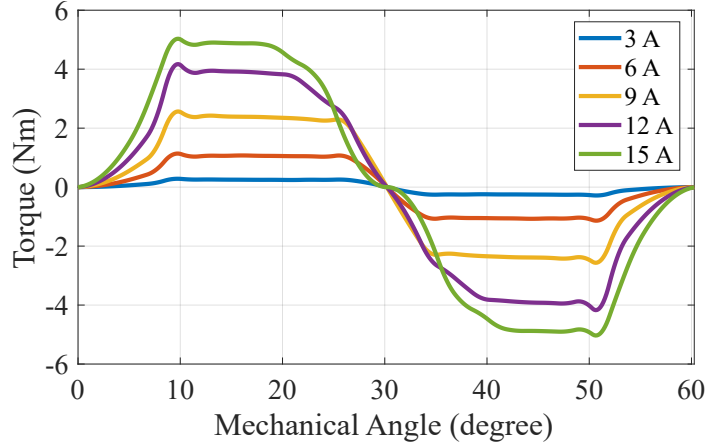


Figure 2.4: The downsampled torque characteristics obtained as in (2.6)

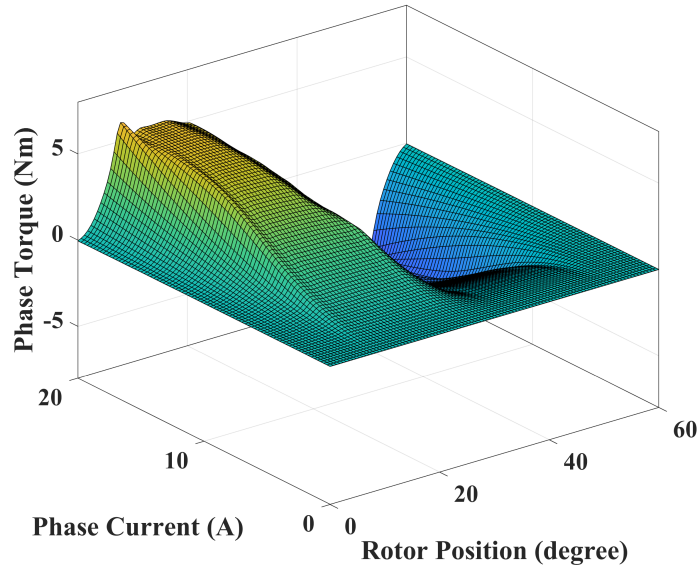


Figure 2.5: Three-dimensional LUT showing electromagnetic torque generated versus phase current and rotor angle obtained as in (2.6).

The resulting incremental area, divided by the incremental angle, gives the torque torque:

$$\text{Phase Torque} = \frac{\partial W(i_{ph}, \theta_m)}{\partial \theta_m}. \quad (2.6)$$

The obtained downsampled torque data is presented in Figure 2.4, while the surface plot of the same can be seen in Figure 2.5. The LUT for one phase can be used to model all phases by applying a rotor position offset of 15° . The offset of 15° in rotor position is applied to align with the symmetric characteristic of a 4-phase SRM with

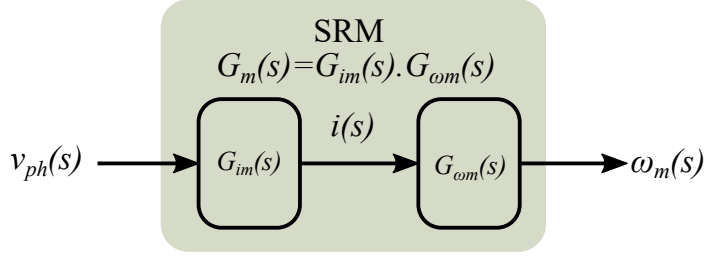


Figure 2.6: Block diagram for the speed control of the proposed SRM drive.

6 rotor poles, ensuring accurate representation in the simulation.

2.2 Derivation of System Linear Model

Linear controllers are typically developed under the assumption of linear system dynamics. As a result, it becomes necessary to derive a linearized model. Hence, in this section, a linearized SRM model is derived to facilitate controller design.

2.2.1 Small signal model of SRM Motor

The small signal model of the SRM is derived from the fundamental voltage and torque equations assuming linear dynamics. From the expressions for voltage equation in (1.3), per phase electromagnetic per phase torque in (1.5), and mechanical torque in (2.2), the small signal model can be obtained. Assuming there is no overlap in phase currents. i.e., only one phase conducts at a time, the voltage and torque equations can be written as below:

$$v = iR_s + L(\theta)\frac{di(t)}{dt} + \omega_m i(t)\frac{dL(\theta)}{d\theta} \quad (2.7)$$

$$J\frac{d\omega_m}{dt} = \frac{1}{2}i^2(t)\frac{dL(\theta)}{d\theta} - T_l - B\omega_m \quad (2.8)$$

Where, i represents the sum of the phase currents, assuming no overlap in phase currents. Also, L_{ph} is represented as L to simplify the equation. By perturbing and linearizing the system around a steady-state operating point characterized by a speed of ω_{m0} and current of i_0 , the state space model of SRM can be obtained. The

state-space representation of the SRM is given by:

$$\dot{x} = Ax + B'u$$

$$Y = Cx + Du. \quad (2.9)$$

$$\text{where, } x = \begin{bmatrix} i \\ \omega_m \end{bmatrix} \text{ and } u = \begin{bmatrix} v \\ T_l \end{bmatrix}.$$

The state-space model is further elaborated as follows:

$$\dot{x} = \begin{bmatrix} -\frac{R_s}{L} - \frac{1}{L} \frac{dL}{d\theta} \omega_{m0} & -\frac{1}{L} \frac{dL}{d\theta} i_0 \\ \frac{1}{J} \frac{dL}{d\theta} i_0 & -\frac{B}{J} \end{bmatrix} x + \begin{bmatrix} \frac{1}{L} & 0 \\ 0 & -\frac{1}{J} \end{bmatrix} u. \quad (2.10)$$

The inductance slope in the torque-generating region is assumed to be constant, and the average inductance is assumed to be the average of aligned and unaligned inductances. Thus,

$$\frac{dL}{d\theta} = \frac{L_a - L_u}{\beta_s}; \quad L = \frac{L_a + L_u}{2}. \quad (2.11)$$

Where L_a , L_u , and β_s are aligned inductance, unaligned inductance, and stator pole arc angle of the SRM motor. To simplify the design of the linear controller, we can extract relevant transfer functions from the state space model as following:

$$G_i(s) = \frac{i(s)}{v_{ph}(s)}; \text{ for } C = \begin{bmatrix} 1 & 0 \end{bmatrix} \quad (2.12)$$

$$G_m(s) = \frac{\omega_m(s)}{v_{ph}(s)}; \text{ for } C = \begin{bmatrix} 0 & 1 \end{bmatrix} \quad (2.13)$$

From equations (2.12) and (2.13), G_{ω_m} can be obtained as below:

$$G_{\omega_m}(s) = \frac{G_m(s)}{G_i(s)} \quad (2.14)$$

Hence, the system linear transfer functions are derived, which can be utilized in designing the linear controllers.

2.3 Conclusions

This chapter outlines the procedure for obtaining the FEA-based SRM model, followed by the development of the small signal model. The FEA-based model effectively captures the nonlinearities present in the SRM machine, enabling detailed simulation studies in various operating modes. Additionally, the model aids in selecting the conduction angle to optimize efficiency and torque ripple.

The derivation of the small signal model relies on two main assumptions: firstly, the neglect of machine core saturation, assuming a linear inductance profile regardless of the phase current; and secondly, the assumption of no torque sharing between phases. The obtained linear model is utilized in designing the linear controllers for subsequent research works.

Chapter 3

Digital Control Development for Four-Phase SRM Drive using Single Current Sensor

This chapter presents a novel SRM drive utilizing a Miller converter-fed SRM motor with a single current sensor, offering a comprehensive control development, dynamic simulation, analysis, and experimental validation. The FEA based model detailed in 2.1 is utilized for simulation studies and the conduction angle is optimized for drive efficiency through parametric simulation studies. The linear SRM model for control design is obtained via small signal analysis as detailed in 2.2. Speed and current controllers are designed using the K-factor method, and the efficacy of the proposed drive is rigorously evaluated across various operating modes in MATLAB Simulink. Additionally, a hardware prototype is developed and the digital control algorithm is implemented on the DSP microcontroller TMS320F28379D based on the designed controllers to further assess drive performance. The results obtained validate the robustness and dynamic performance of the SRM drive across variable speed, variable torque, and constant power modes of operation.

3.1 Proposed System

The proposed converter topology is illustrated in Figure 3.1. As shown in Figure 3.1, the system utilizes a Miller converter, which, in the case of a four-phase SRM, results

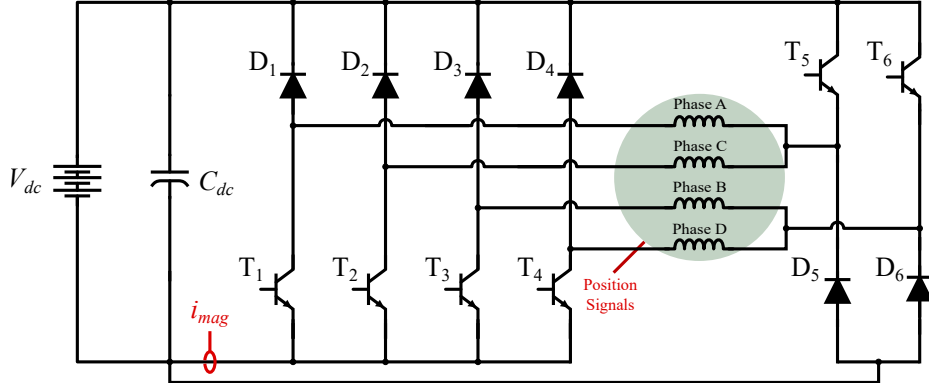


Figure 3.1: The circuit configuration of the proposed Miller converter fed the SRM drive utilizing a single current sensor.

in a reduction in the number of switches and diodes compared to an AHB converter. Specifically, the Miller converter employs six switches and six diodes, while the AHB converter necessitates eight switches and eight diodes. By sharing one leg between two non-adjacent phase windings in the power converter, independent current control in all phases is achieved. Consequently, this design effectively mitigates extended demagnetization times. Despite the uneven distribution of heating losses among devices, it notably enhances control flexibility.

The proposed system incorporates a single current sensor strategically placed to measure phase currents during magnetization. To achieve this, the magnetizing and demagnetizing paths are decoupled, as depicted in Figure 3.1, which also shows the operational modes for phase A of the proposed SRM drive. In the control scheme, only one phase is excited at a time, allowing the current sensor to measure the individual phase current when the corresponding phase is active. Consequently, independent control of this drive is feasible with just a single current sensor.

The control logic for the proposed drive is shown in Figure 3.2. The control scheme employs a dual loop with inner current control and an outer speed control loop. The controller's inputs include the speed reference, the sensed current through the magnetizing path (i_{mag}), and position signals. A position sensor is utilized to gather position information, and both speed (ω_m) and position (θ_m) are derived from these signals. The measured speed (ω_m) goes through a digital low pass filter for noise rejection and is compared with the reference speed (ω_{ref}) and fed into the speed controller, which gives the current reference (i_{ref}). The measured current through the magnetizing path (i_{mag}) is passed through a low-pass digital filter to filter out

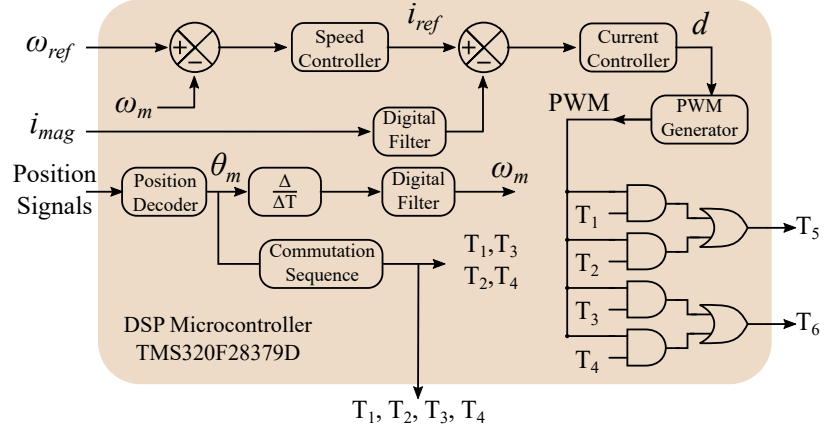


Figure 3.2: The block diagram depicting the control logic for the proposed SRM drive.

the noise, which is then compared with the current reference (i_{ref}). In the proposed switching scheme, switches T_1 , T_2 , T_3 , and T_4 are switched at the fundamental frequency following the commutation sequence. The duty cycle output of the current controller is fed to the PWM generator module and supplied to switches T_5 and T_6 according to the phase sequence.

Figure 3.3 is drawn assuming the phase excitation sequence is in a clockwise direction, i.e., D-A-B-C. This sequence is selected to illustrate the operation of the drive during clockwise rotation. As shown in Figure 3.3(a), during the commutation of winding D, phase A is excited. To enter the demagnetization region for the D phase, switches T_4 and T_6 are turned off. During this mode, diodes D_4 and D_6 conduct, applying $-V_{dc}$ across phase D, thereby feeding the phase current back to the source until phase D is completely demagnetized. Simultaneously, switches T_1 and T_5 are turned on, applying $+V_{dc}$ across phase A. As in Figure 3.3(b), as T_5 is turned off, the phase A current freewheels through switch T_1 and diode D_5 . During this period, the voltage across phase A is zero, and the phase current decays due to winding resistive loss. Hence, the phase current is controlled by switching T_5 in PWM mode at high frequency. In these two modes, only the current through the phase A winding appears in the current sensor output since the magnetization and demagnetization paths are decoupled. Moving to Figure 3.3(c), phase A, akin to phase D in Figure 3.3(a), undergoes demagnetization as phase B is excited. During this mode, the current sensor measures the current through the phase B winding.

Therefore, it can be inferred that the proposed system, incorporating the Miller converter and employing a single current sensor, presents a cost-effective solution

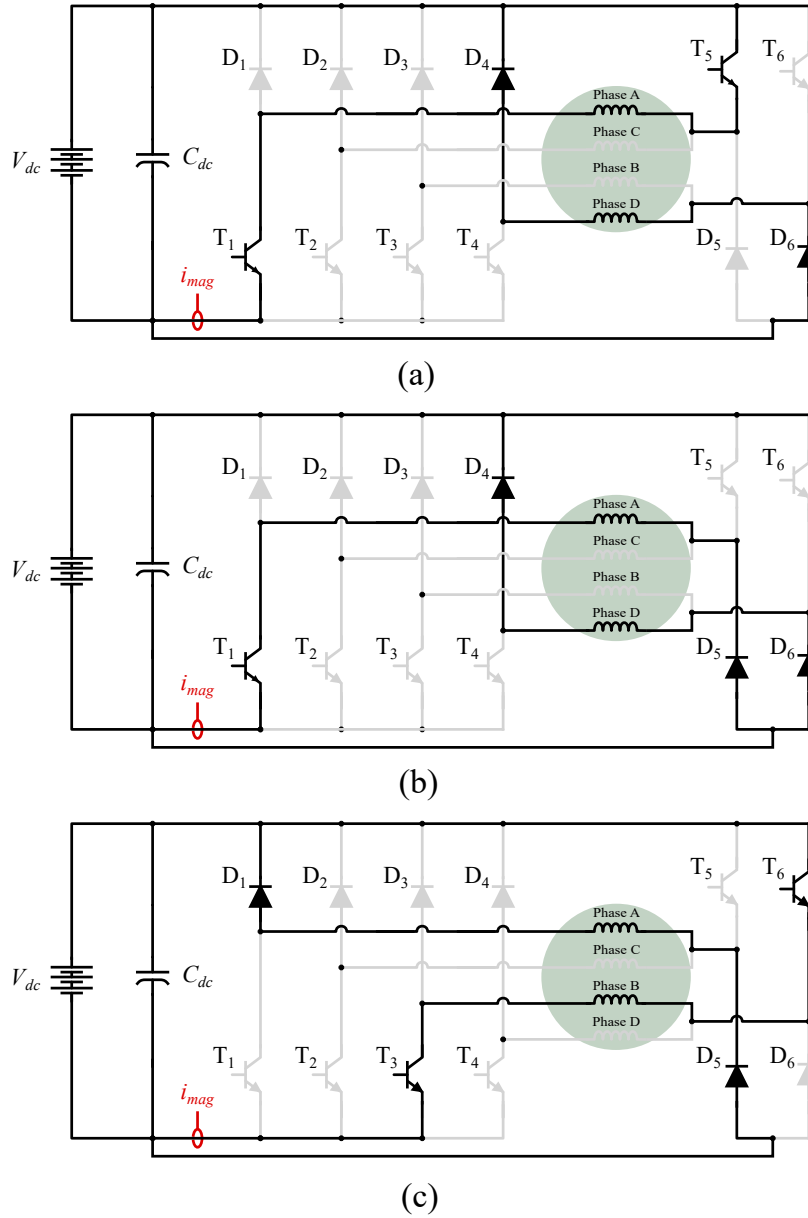


Figure 3.3: Three operating states of phase A during the motoring mode. (a) Magnetization mode. (b) Zero voltage mode. (c) Demagnetization mode.

particularly crucial for medium power applications. The control strategy proposed without overlap in the conduction period for different phases ensures optimal drive performance. The control and validation of the proposed are detailed in subsequent sections.

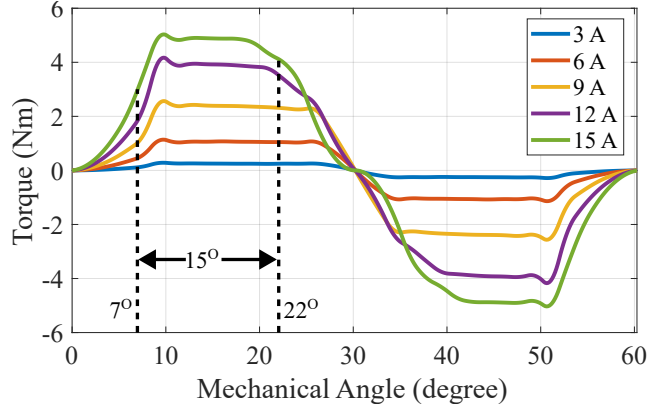


Figure 3.4: The conduction period of 15° shown in torque vs rotor angle characteristic.

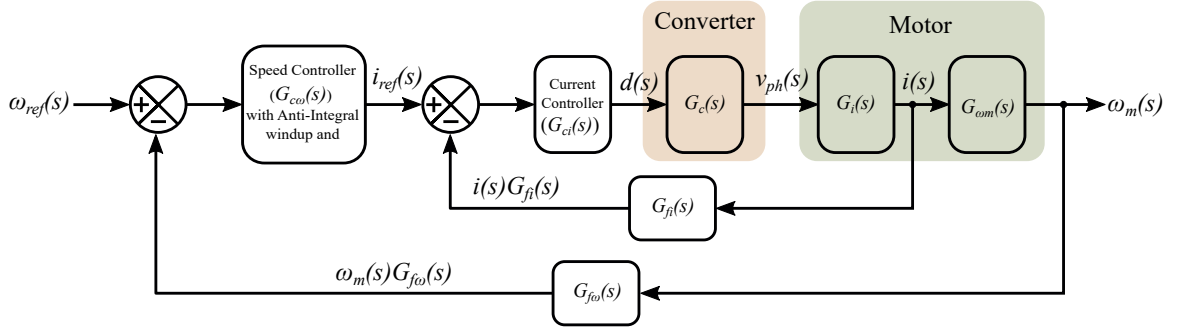


Figure 3.5: The control block diagram for the SRM drive utilizing single current sensor.

3.2 Selection of Conduction Angle

Furthermore, the conduction and commutation angles have been fine-tuned to enhance efficiency at the rated power level. As previously explained, given the constraint of using a single current sensor to control phase currents independently, it is imperative to avoid conduction overlap between the phases. Therefore, to ensure only one phase is excited at a time, the conduction angle for each phase is fixed at 15° . Through parameterized simulations and analysis, it has been determined that the maximum efficiency is achieved with a turn-on angle of 7° , while the turn-off angle is set at 22° ($7^\circ + 15^\circ$). The obtained turn-on and commutation angles are marked in the torque characteristics shown in Figure 3.4. Subsequent investigations are conducted with these fixed turn-on and commutation angles.

3.2.1 System Transfer Function

The block diagram for the per-phase control can be seen in Figure 3.5. Here, the expressions for $G_i(s)$ and $G_{\omega_m}(s)$ are given in equations (2.12) and (2.14) respectively. Now, the transfer functions for the converter transfer function and feedback loop low-pass filters need to be derived to obtain the plant transfer functions.

The expression for the average output voltage of the soft-chopped converter, denoted as V_{ph} , during a switching cycle T_s is given by:

$$V_{ph} = V_{dc}d + 0 \cdot (1 - d) = d \cdot V_{dc}. \quad (3.1)$$

In the soft-chopped converter, the output voltage switches between $+V_{dc}$ and zero or $-V_{dc}$ and zero. Due to the nature of pulse width modulation, there is a delay of half the switching period T_s , which can be represented as a pole with a time constant $\tau_d = T_s/2$. For a switching frequency of 10 kHz, T_d is equal to 50 μs . Thus, the converter transfer function is given by:

$$G_c(s) = \frac{v_{ph}(s)}{d(s)} = \frac{V_{dc}}{1 + s\tau_d}. \quad (3.2)$$

The current feedback transfer function is of a low-pass type, designed to eliminate high-frequency components. It corresponds to a first-order filter with a time constant τ_{fi} , resulting in a pole at 8 kHz (10 times the current controller corner frequency). Therefore:

$$G_{fi}(s) = \frac{1}{1 + s\tau_{fi}}; \tau_{fi} = \frac{1}{2\pi \cdot 8000}. \quad (3.3)$$

Similarly, the speed feedback transfer function is also a first-order low-pass filter with a time constant $\tau_{f\omega_m}$ corresponding to a pole at 1000 Hz:

$$G_{f\omega_m}(s) = \frac{1}{1 + s\tau_{f\omega_m}}; \tau_{f\omega_m} = \frac{1}{2\pi \cdot 1000}. \quad (3.4)$$

Now, we can derive the plant transfer functions for the current controller design and speed controller design. The equivalent plant transfer function for the current controller design is:

$$G_{pi}(s) = G_c \cdot G_{fi} \cdot G_i(s). \quad (3.5)$$

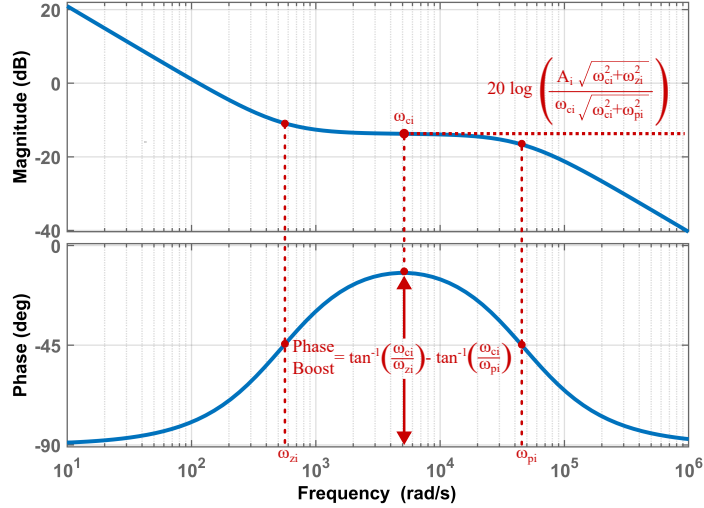


Figure 3.6: Bode plot of the current controller, G_{ci} (Type II Compensator)

Similarly, the equivalent plant transfer function for the speed controller design is:

$$G_{p\omega_m}(s) = \frac{G_{ci} \cdot G_c \cdot G_i}{1 + G_{ci} \cdot G_c \cdot G_i \cdot G_{fi}} \cdot G_{\omega_m} \cdot G_{f\omega_m}. \quad (3.6)$$

Now from the known electrical parameters of the machine given in Table 2.1, the plant transfer functions are obtained for control design.

3.3 Controller Design and Implementation

3.3.1 K Factor Method

For the obtained plant transfer functions, type II compensators are designed using the K-Factor approach Venable (1983). Initially, the current controller is designed for the current loop plant transfer function given in (3.5). The controller bandwidth is set to 800 Hz ($\omega_{ci} = 1600\pi$), considering the switching frequency of 10 kHz. To minimize transient ripple in the phase current and consequent torque ripple, a desired phase margin of 70° is chosen. The type II compensator transfer function is given by

$$G_{ci}(s) = \frac{A_i s + \omega_{zi}}{s s + \omega_{pi}}. \quad (3.7)$$

In the controller design process, the phase boost required for the loop transfer

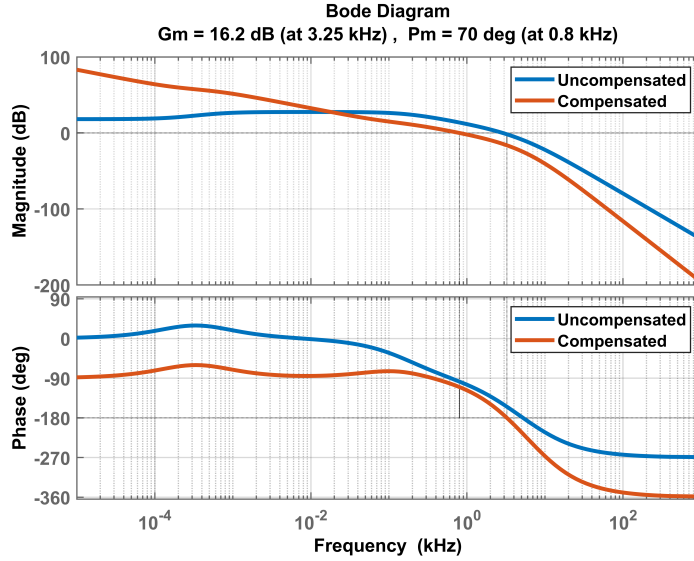


Figure 3.7: Bode plots of plant transfer function (G_{pi}) and loop transfer function ($G_{pi} \cdot G_{ci}$) for closed-loop current control.

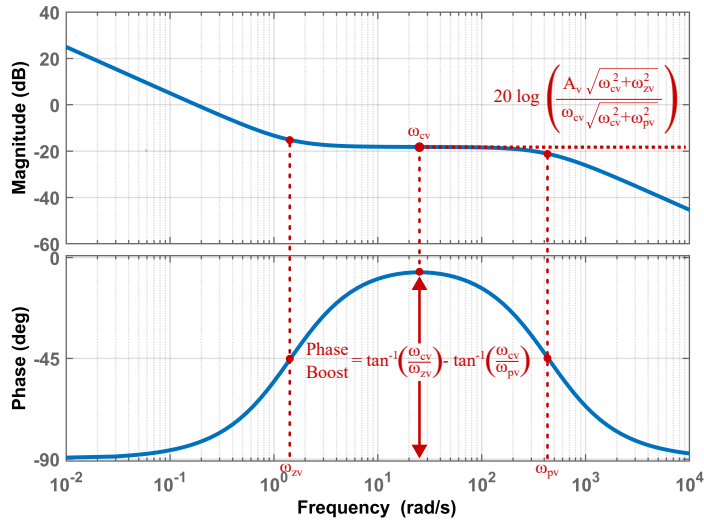


Figure 3.8: Bode plot of the speed controller, G_{cwm} (Type II Compensator).

function ($G_{pi} \cdot G_{ci}$) to achieve the desired phase margin at the controller cutoff frequency (ω_{ci}) is calculated. Subsequently, the controller zero (ω_{zi}) and pole (ω_{pi}) are determined, and the controller gain (A_i) is adjusted to achieve unity gain at the controller cut-off frequency. The bode plot for the resulting current controller is shown in Figure 3.6, with bode plots for the plant transfer function (G_{pi}) and the loop transfer function ($G_{pi} \cdot G_{ci}$) presented in Figure 3.7.

Similarly, the speed controller for the plant transfer function in (3.6) is designed

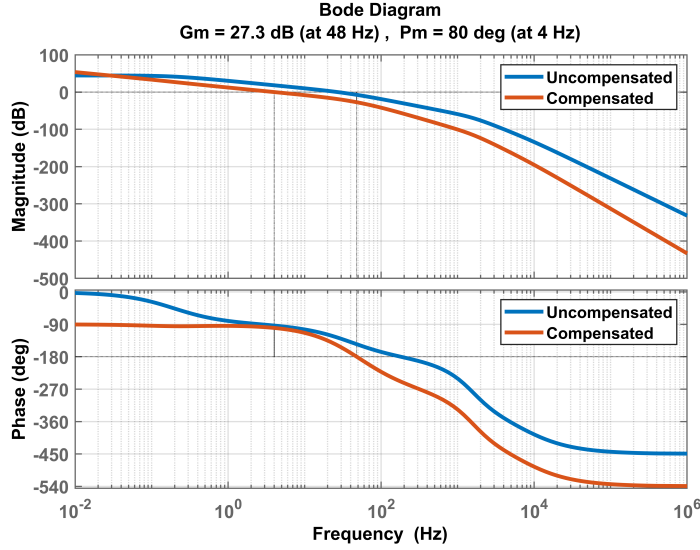


Figure 3.9: Bode plots of plant transfer function ($G_{p\omega_m}$) and loop transfer function ($G_{p\omega_m} \cdot G_{c\omega_m}$) for closed-loop speed control.

for a bandwidth of 4 Hz with a desired phase margin of 80° . The type II transfer function is given by

$$G_{c\omega_m}(s) = \frac{A_{\omega_m} s + \omega_z \omega_m}{s s + \omega_p \omega_m}. \quad (3.8)$$

The bode plot for the obtained speed controller is shown in Figure 3.8. The bode plots for the plant transfer function ($G_{p\omega_m}$) and loop transfer function ($G_{p\omega_m} \cdot G_{c\omega_m}$) are provided in Figure 3.9.

3.3.2 Discretization of Controllers and Integral Anti-windup using Back Calculation Method

The obtained controllers are in the continuous domain. Hence, the discretization of linear controllers is essential for implementing control algorithms in digital control systems. This discrete-time operation requires converting continuous-time controllers and system models into discrete-time equivalents. Additionally, finite precision and hardware limitations in digital systems must be considered, which can introduce quantization errors. Ensuring stability in the discrete-time domain, adjusting controller parameters, and addressing computational constraints are vital aspects of this process. The current controller transfer function shown in (3.7) is discretized using bilinear transformation for a sampling frequency of $20 \mu s$. The discretized model of the cur-

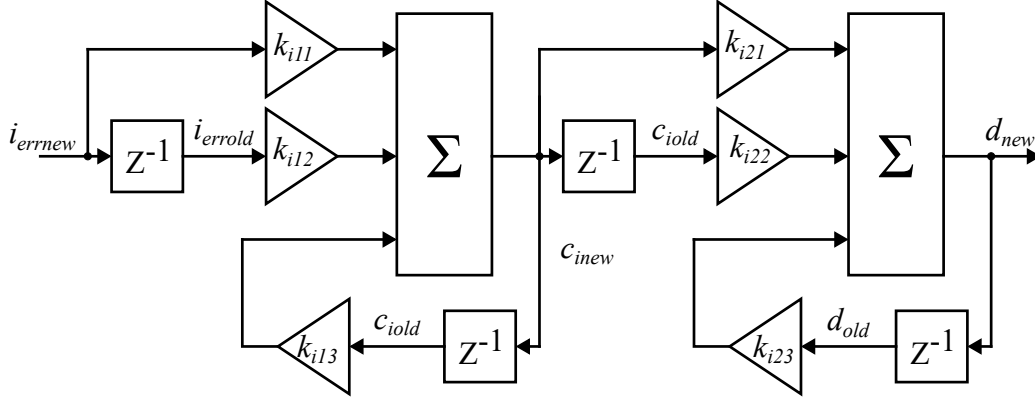


Figure 3.10: Discretized current controller model.

rent control transfer function is shown in Figure 3.10. Constants, k_{i11} , k_{i12} , k_{i13} , k_{i21} , k_{i22} , and k_{i23} corresponds to the gain values in discrete current controller.

The motor operates as a system with higher inertia. To prevent the current from exceeding its rated value, it is essential to introduce saturation to the current reference. Without this saturation, a substantial overshoot in the current reference could occur, posing a risk during startup or transient load changes. Therefore, implementing saturation is crucial to safeguard the motor drive. While saturation is already applied to the controller's output, there remains a possibility of overshooting in the integral component. This can occur due to the integral action continuing to accumulate errors even when the system is saturated. To address this concern, the implementation of integral anti-windup becomes essential. This mechanism helps prevent the integral component from excessively accumulating error during saturation, thereby mitigating the risk of overshoot and instability.

Similar to the current controller, the speed controller transfer function shown in (3.8) is discretized using bilinear transformation for a sampling frequency of $20 \mu s$. Anti-integral windup are explored for PID-based control systems in [Tarbouriech and Turner \(2009\)](#), [Visioli \(2006\)](#). Here, a back calculation-based anti-windup strategy is developed for the designed discrete controller as shown in 3.11. The controller gains $k_{\omega 11}$, $k_{\omega 12}$, $k_{\omega 13}$, $k_{\omega 21}$, $k_{\omega 22}$, and $k_{\omega 23}$ corresponds to the discretized speed controller transfer functions. On the other hand, the parameter k_w is associated with the anti-windup constant, which governs the rate of integral term reset. The control algorithm for hardware implementation is described in the next section.

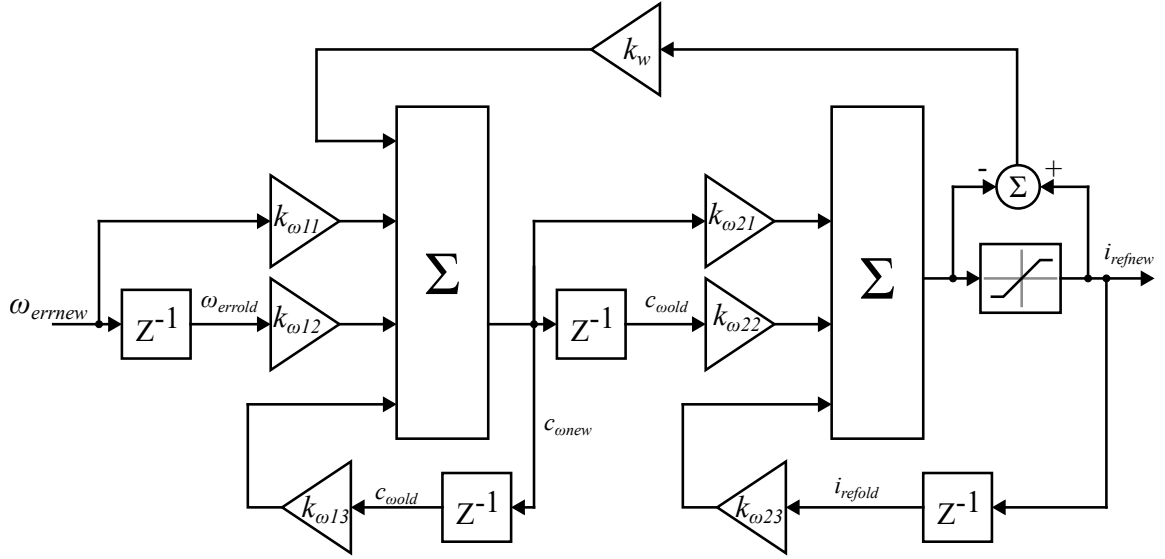


Figure 3.11: Discretized speed controller controller model with saturation and integral windup.

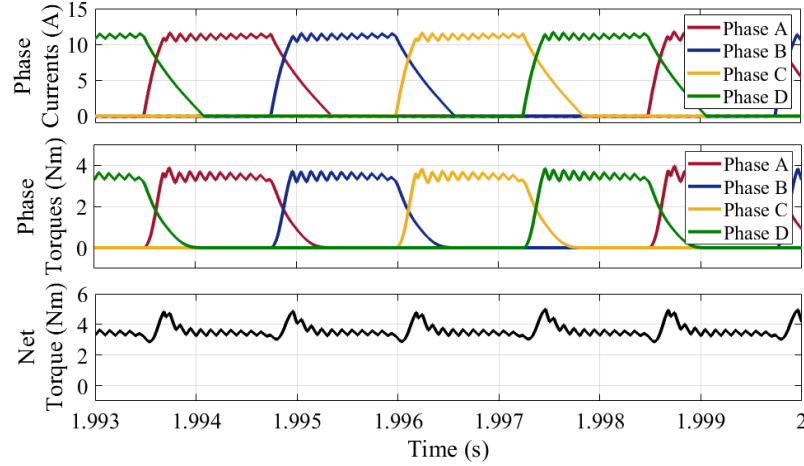


Figure 3.12: Simulation results showing phase currents, phase torques, and net torque at 2000 rpm.

3.4 Simulation Results

The MATLAB Simulink model described in 2.1 is utilized for the simulation studies. The simulation is carried out to validate and verify the operation of the proposed SRM drive and to validate the control strategy and design detailed in previous sections.

Figure 3.12 showcases individual phase currents, phase torques, and the net torque at 2000 rpm. Notably, the designed current controller effectively regulates the phase

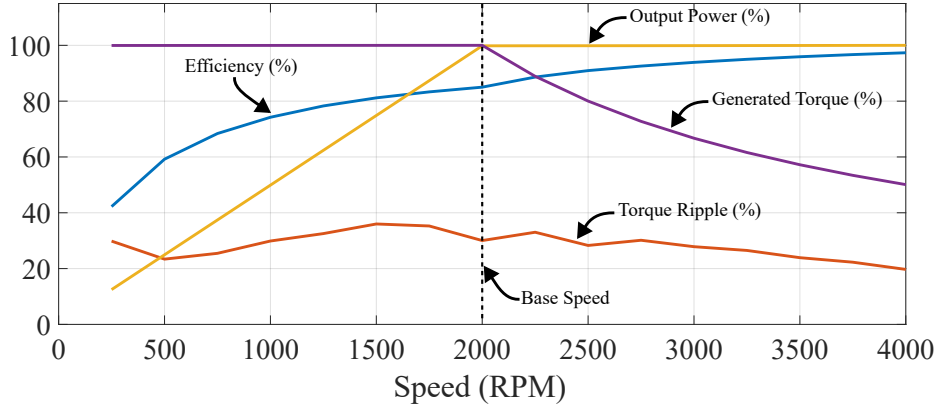


Figure 3.13: Drive characteristics obtained from simulation analysis showing output torque, output power, efficiency, and torque ripple across a wide range of speed.

currents within a satisfactory tolerance band, even without relying on hysteresis control. This demonstrates its efficacy and offers a simpler and more reliable alternative to techniques like hysteresis or delta modulation. Furthermore, the plot reveals the torque sharing between phases achieved by the employed control strategy, with the net torque representing the sum of individual phase torques. Evidently, while only one phase operates in magnetization mode, the torque generated by the demagnetization current facilitates torque sharing at the commutation points.

Figure 3.13 provides insight into the efficiency and torque ripple across a wide speed range with a fixed conduction period. Notably, the net torque exhibits a maximum torque ripple of 29.8% at 250 rpm with a 12% load and a minimum of 19% at 4000 rpm under full load. Furthermore, the drive displays its lowest efficiency of 42.2% at 250 rpm with a 12% load, while achieving maximum efficiency of 97.34% at 4000 rpm under full load. At the rated speed and power, the drive maintains a torque ripple of 29% and an efficiency of 85%. These results collectively validate the suitability of the SRM for a wide array of applications.

To comprehensively evaluate the control design’s effectiveness, an in-depth simulation is carried out, analyzing the drive’s performance across various operational scenarios. These scenarios encompass variable speed control, variable torque control, and constant power control at speeds exceeding the base speed. In Figure 3.14, the dynamic performance of the drive during variable speed control under constant load torque is illustrated. Operating at a load torque of 3.58 Nm, the motor seamlessly tracks the reference speed, exhibiting neither overshoot nor undershoot. Figure 3.15

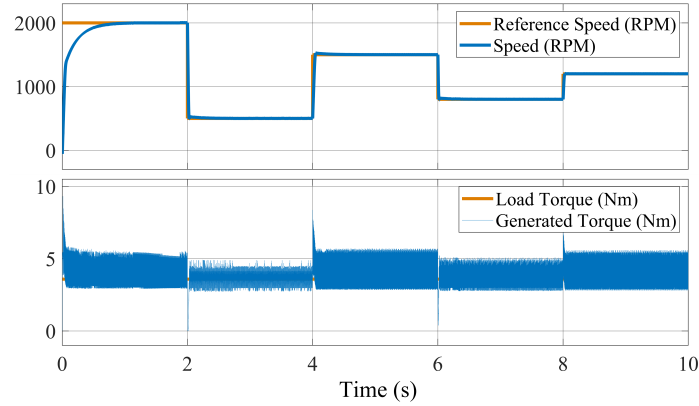


Figure 3.14: Simulation results showing reference speed, speed, load torque and output torque during dynamic step changes in speed reference at constant load torque.

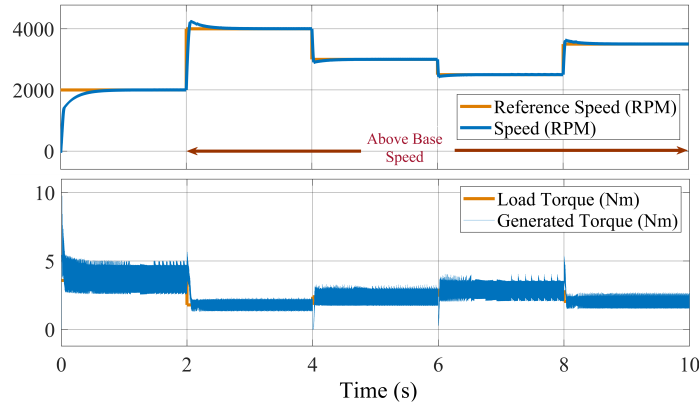


Figure 3.15: Simulation results showing reference speed, speed, load torque and output torque during dynamic step changes in speed reference in constant power region above base speed.

presents the speed and generated torque in the constant power region above the base speed. In this mode, power is set to the rated 750 W, and the results demonstrated accurate tracking of the speed reference. Figure 3.16 shows the dynamic performance of the drive in constant speed mode with variable load torque. The speed is regulated at the rated speed of the motor of 2000 rpm. Minor amplitude overshoots or undershoots occurred during step changes in load torque, but the speed promptly stabilized thereafter.

Across all three figures (Figure 3.14, Figure 3.15, and Figure 3.16), it is evident that the integration of anti-windup effectively mitigated speed overshoots and minimized delays in tracking the reference speed, especially during startup and dynamic speed variations. Furthermore, the approach successfully addressed the challenge of

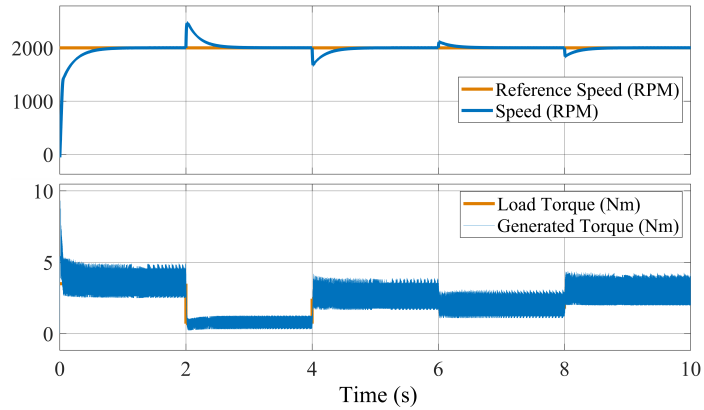


Figure 3.16: Simulation results showing reference speed, speed, load torque and output torque during dynamic step changes in load torque at constant speed reference of 2000 rpm.

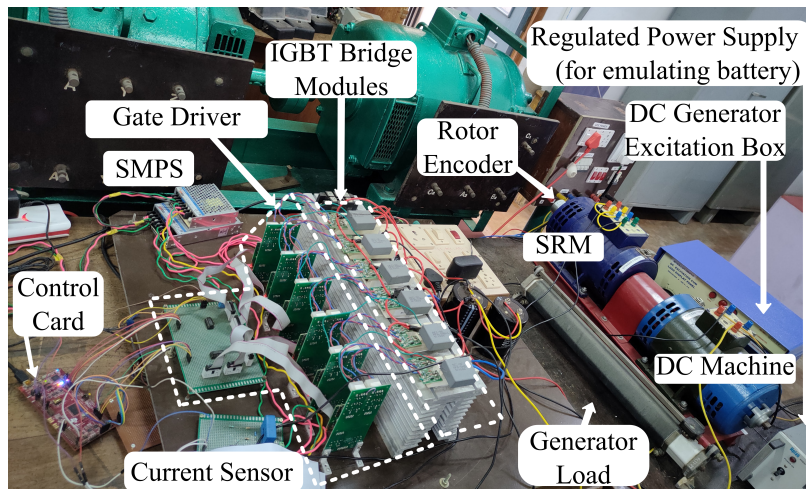


Figure 3.17: Photograph of the experimental setup.

integrator accumulation, mitigating potential numerical instability and floating-point errors in digital implementations.

Simulations confirm robust performance of the drive system across various operating conditions, validating the effectiveness of the control design. This performance holds true under steady state, dynamic, and transient conditions, as well as across variable speed, variable torque, and constant power modes.

3.5 Experimental Implementation: Results and Discussion

In the laboratory, an experimental prototype is set up as shown in Figure 3.17. A 1 hp four-phase SRM with 8 stator poles and six rotor poles is used. A separately excited DC machine is coupled with the SRM for loading. The setup uses six SKM50GB12T4 IGBT modules, with each IGBT module representing one leg of the converter. In each IGBT module, one is used as an IGBT switch, and the body diode of the other IGBT is used as a diode to get the converter, as shown in Figure 3.1. Skyper 32R driver is used as the gating circuit for the semiconductor devices. A hollow shaft-type incremental quadrature encoder, ERA50T, connected to the shaft of the machine is used to sense the rotor position. The resolution of the encoder is 1024 pulses per revolution (PPR). One hall current sensor, LA25P, is employed to measure current through the magnetization path (i_{mag}). Signal conditioning for the current sensing circuit is done by MCP6022 op-amp-based differential amplifier circuit. Control implementation for the system is carried out on a DSP microcontroller, the TMS320F28379D.

3.5.1 Control Algorithm

The digital control algorithm implementation of the proposed scheme involves speed and current control. The clock frequency (f_{clock}) of the TMS320F28379D is 200 MHz [TI \(2019\)](#). The gating pulses need to be generated according to the commutation sequence. The enhanced quadrature encoder pulse (eQEP) module of the controller is configured in quadrature counter mode. Hence, the counter register (QPOSCNT) counts from 0 to 4096 ($4 \cdot \text{PPR}$) in a full mechanical rotation. Speed is calculated by determining the incremental position in a unit time (UT) interval. This time interval for speed measurements should align with the control loop bandwidth (4 Hz), ensuring it is at least twice as fast as the control loop period for timely updates. Additionally, the interval should be less than the time required for traversing a complete rotation at maximum speed. At maximum speed (2000 rpm), the rotor completes one full rotation in 0.03 seconds. Therefore, to calculate speed, the unit timer register of the eQEP module is set to $2 \cdot 10^6 (= 0.01 \cdot f_{clock})$ to achieve a UT of 0.01 seconds. To measure the current, one analog-to-digital conversion (ADC) pin is configured in a single 12-bit mode. Six ePWM modules are configured in independent mode for a

switching frequency of 10 kHz. For this, ePWM prescalers are set to 1, and the ePWM timer base period (TBPRD) register is set with a value of 5000. For synchronizing the control operations, a timer (timer0) is configured for $20\mu s$. Consequently, all the transfer functions, including the speed low pass filter, current low pass filter, speed controller, and current controller, are discretized for a sampling time of $20\mu s$. The control algorithm is implemented in the timer interrupt service routine (ISR). Algorithm 1 outlines the timer ISR control algorithm, while Figure 3.18 visually showcases its implementation within the timer ISR using a flowchart.

A brief explanation of the algorithm is given below.

3.5.1.1 Calculation of position and speed

First, the position and speed are calculated from the position sensor, as shown in steps 1 and 2 in Algorithm 1. One mechanical rotation of the rotor corresponds to 4096 counts in the QPOSCNT register, measured with respect to the index pulse position from the QEP sensor. In the case of an SRM with six rotor poles, one mechanical rotation translates to six electrical rotations. To determine the excitation and commutation angles, it is essential to predetermine and utilize the appropriate phase. As shown in Figure 3.18, the QPOSCNT register's content is latched to the position latch register during each unit timer interrupt (i.e., after every 0.01 s). Consequently, the speed can be calculated by determining rotations per minute from the change in position within the unit time (UT).

3.5.1.2 Current sensing

The current sensor is connected to the ADC pin. ADC result register is read and multiplied by the calibration factor, k_{ADC} as shown in step 4 of Algorithm 1. The maximum voltage input for the ADC is 3 V, and a 3 V input corresponds to 4095 in the ADC result register. Therefore, by taking into account the sensor gain and the calibration factor mentioned earlier, the ADC result is calibrated to obtain an accurate value.

3.5.1.3 Speed and current low pass filters

The transfer functions in (3.3) and (3.4) are discretized using bilinear transformation at a sampling frequency of $20\mu s$. The pseudo-code of the digital filters is shown in

Algorithm 1 Timer ISR for speed control system.

- 1: **Position calculation via QEP module:**
QPOSCNT=Read Position Counter Register.
Calculate mechanical position and electrical angle:
$$\theta_m = \frac{360 (\text{QPOSCNT})}{4096}$$
$$\theta_e = \text{remainder}(\theta_m, 60)$$
 - 2: **Speed Calculation:**
 θ_{new} = Read position latch register if the unit timer flag is set.
$$\omega_{new} = \frac{60(\theta_{new} - \theta_{old})}{4096 \cdot (UT)}; \theta_{old} = \theta_{new}$$
 - 3: **Speed low pass filter:**
$$\omega_{fnew} = k_{\omega f1}(\omega_{new} + \omega_{old}) + k_{\omega f2} \cdot \omega_{fold};$$
$$\omega_{old} = \omega_{new}; \omega_{fold} = \omega_{fnew}$$
 - 4: **Currents Sensing via ADC module:**
Set SOC and wait for the EOC flag. Acknowledge and reset the EOC flag.
$$i_{new} = \text{ADCRESULT} \cdot k_{ADC}$$
 - 5: **Current low pass filter:**
$$i_{fnew} = k_{if1}(i_{new} + i_{old}) + k_{if1} \cdot i_{fold}$$
$$i_{old} = i_{new}; i_{fold} = i_{fnew}$$
 - 6: **Speed Controller:**
$$\omega_{errnew} = \frac{\pi}{30}(\omega_{ref} - \omega_{fnew})$$
$$c_{wnew} = k_{\omega 11}(\omega_{errnew} + \omega_{erold}) + c_{wold};$$
$$i_{refnew} = k_{\omega 21} \cdot c_{wnew} - k_{\omega 22} \cdot c_{wold} + k_{\omega 23} \cdot i_{refold}$$
 - 7: **Saturation, integral anti-windup and variable updates for speed controller:**
if ($i_{refnew} > i_{thresh}$) **then**
 $c_{wnew} = c_{wnew} + k_w(i_{thresh} - i_{refnew})$
 $i_{refnew} = i_{thresh}$
else if ($i_{refnew} < 0$) **then**
 $c_{wnew} = c_{wnew} + k_w \cdot (0 - i_{refnew}); i_{refnew} = 0$
end if
$$\omega_{erold} = \omega_{errnew}; c_{wold} = c_{wnew}; i_{refold} = i_{refnew};$$
 - 8: **Current controller:**
$$i_{errnew} = i_{refnew} - i_{fnew}$$
$$c_{inew} = k_{i11}(i_{errnew} + i_{erold}) + c_{iold}$$
$$d_{new} = (k_{i21}c_{inew} - k_{i22}c_{iold} + k_{i23}d_{old})$$
$$i_{erold} = i_{errnew}; c_{iold} = c_{inew}; d_{old} = d_{new};$$
 - 9: **Excitation and commutation sequence:**
if ($7^\circ < \theta_e < 22^\circ$) **then**
 Phase A: $\text{CMP}_{T_1} \leftarrow \text{TBPRD}; \text{CMP}_{T_5} \leftarrow d_{new} \cdot \text{TBPRD}$
else if ($22^\circ < \theta_e < 37^\circ$) **then**
 Phase B: $\text{CMP}_{T_3} \leftarrow \text{TBPRD}; \text{CMP}_{T_6} \leftarrow d_{new} \cdot \text{TBPRD}$
else if ($37^\circ < \theta_e < 52^\circ$) **then**
 Phase C: $\text{CMP}_{T_2} \leftarrow \text{TBPRD}; \text{CMP}_{T_5} \leftarrow d_{new} \cdot \text{TBPRD}$
else
 Phase D: $\text{CMP}_{T_4} \leftarrow \text{TBPRD}; \text{CMP}_{T_6} \leftarrow d_{new} \cdot \text{TBPRD}$
end if
 - 10: Acknowledge Timer interrupt and return to main program.
-

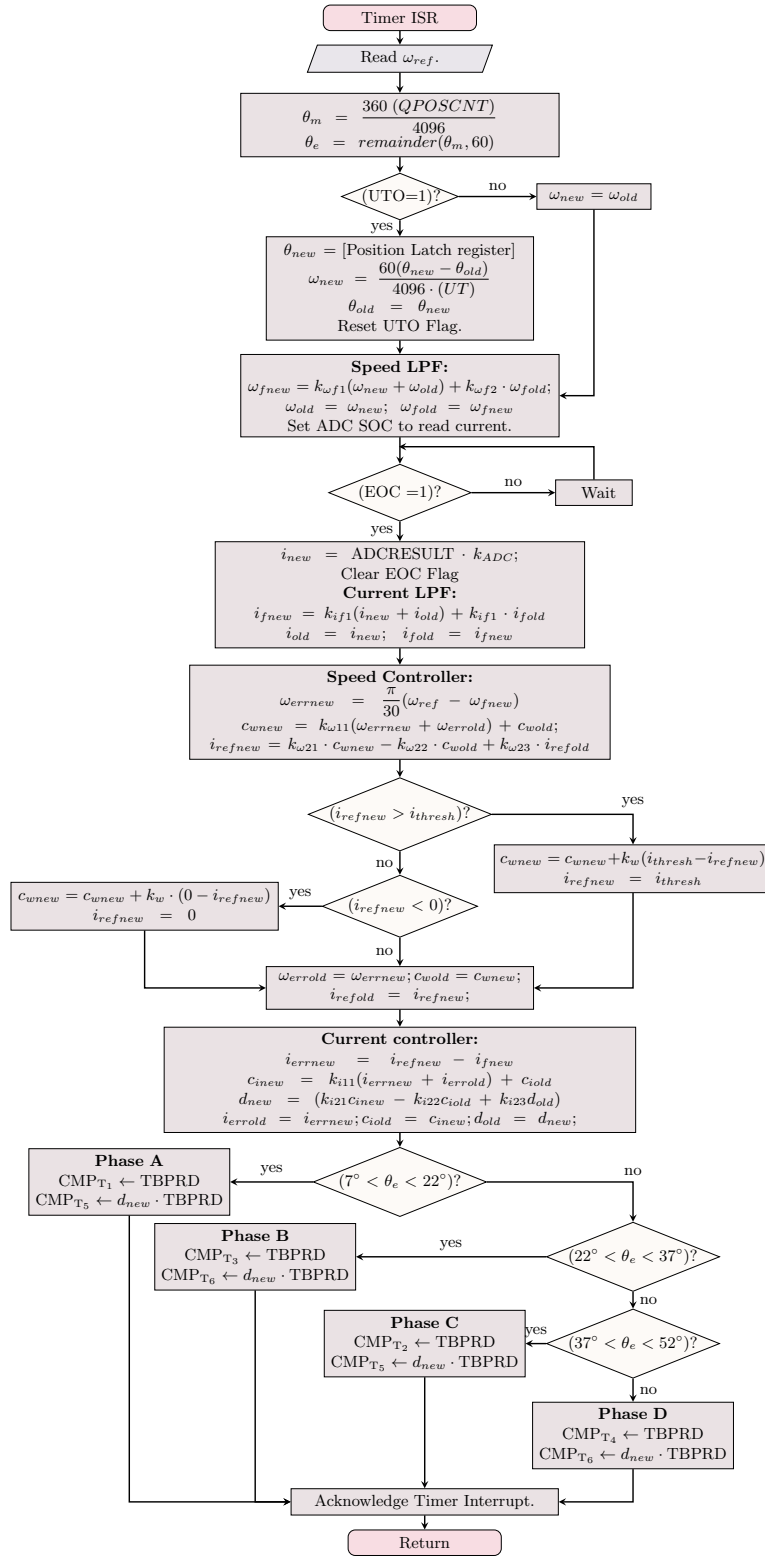


Figure 3.18: Flowchart of the control implementation within Timer ISR.

steps 3 and 5 of Algorithm 1. The constants $k_{\omega f1}$ and $k_{\omega f2}$ pertain to the discretized speed feedback filter, while k_{if1} and k_{if2} correspond to the constants in the discretized current filter.

3.5.1.4 Speed and current controllers

The discretized models for the current and speed controllers shown in Figure 3.10 and Figure 3.11 are implemented in the controller as demonstrated in the steps 6 and 8 in Algorithm 1. As evident in Figure 3.11, the integral anti-windup term (k_w) is incorporated to address integral windup issues. In step 7 of Algorithm 1, to implement saturation and integral anti-windup, it is first checked if the value of i_{refnew} exceeds a predefined threshold band (i_{thresh} and zero). If it does, c_{wnew} saturates due to the windup term, and i_{refnew} is set to the threshold value.

3.5.1.5 Phase Current Control

As in step 9 of Algorithm 1, the output of the current controller (d_{new}) represents the duty cycle to be applied to either switches T_1 or T_2 , depending on the phase that needs to be excited. The determination of the phase to be excited is made in advance based on predetermined excitation and commutation angles. Consequently, the product of the duty cycle and TBPRD is directed to the compare (CMP) register of the corresponding ePWM. Simultaneously, as one of the bottom switches (T_1, T_2, T_3, T_4) are active throughout their respective phase conduction period, TBPRD is fed into their corresponding compare registers.

3.5.2 Results and Discussion

The performance of the proposed SRM drive is assessed using the experimental prototype, examining both steady-state and dynamic behavior. In Figure 3.19, steady-state experimental waveforms are presented. Figure 3.19(a) illustrates voltage and current waveforms at 1200 rpm, with a switching frequency of 10 kHz. The results align with the simulation results presented. The current controller successfully regulates phase current within acceptable limits without employing hysteresis control, showcasing its effectiveness as a simpler and more reliable alternative to hysteresis or delta modulation techniques. Figure 3.19(b) demonstrates the successful decoupling of the demagnetizing current, showcasing the efficacy of control using a single sensor. To

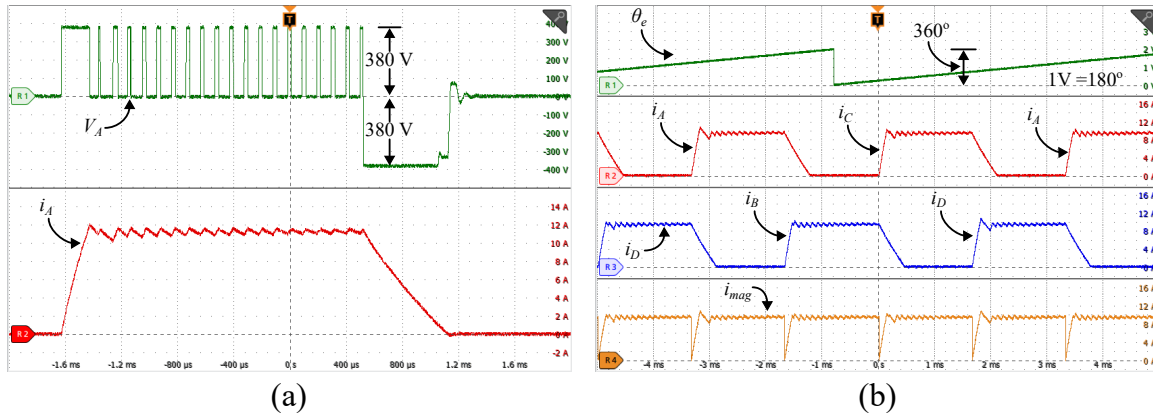


Figure 3.19: Experimental results showing steady state voltage and current waveforms. (a) Phase voltage and phase current at 1200 rpm at rated load. (b) electrical angle, phase currents, and current through magnetization path at 1500 rpm at rated load.

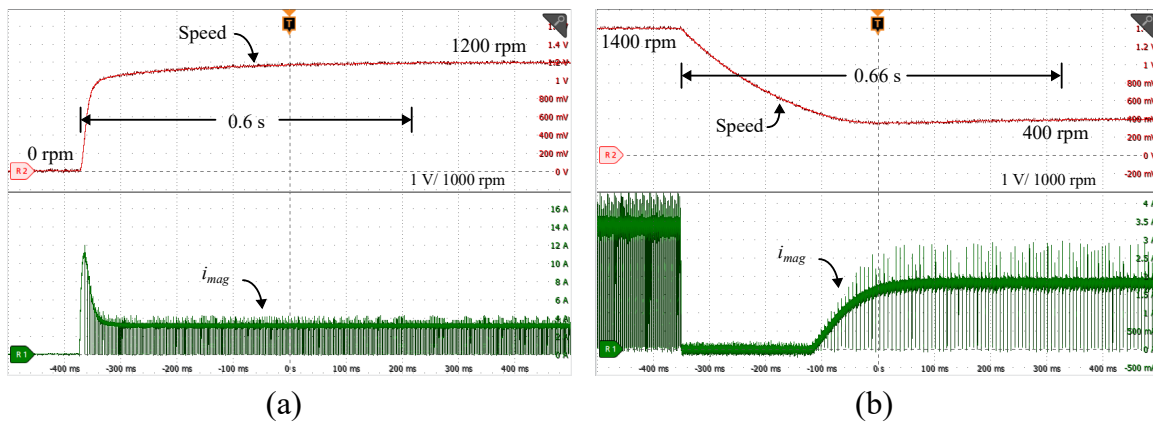


Figure 3.20: Experimental results showing transient speed waveforms and current through the magnetizing path (i_{mag}). (a) Transient waveforms for a step change in speed reference from 0 to 1200 rpm. (b) Transient waveforms for a step change in speed reference from 1400 to 400 rpm.

visualize this, the digital-to-analog (DAC) channel within the DSP microcontroller is configured to display electrical rotor angle waveforms on the digital storage oscilloscope (DSO). Current probes are positioned along the two common connections for alternate phases. The waveform of the current through the magnetizing path (i_{mag}), which is sensed for closed-loop operation, is also measured using a current probe. The results affirm the successful decoupling of the demagnetizing current. It is evident from the waveforms that the current through the individual phases can be controlled by controlling the current through the magnetizing path, when there is no overlap between phases in the conduction period.

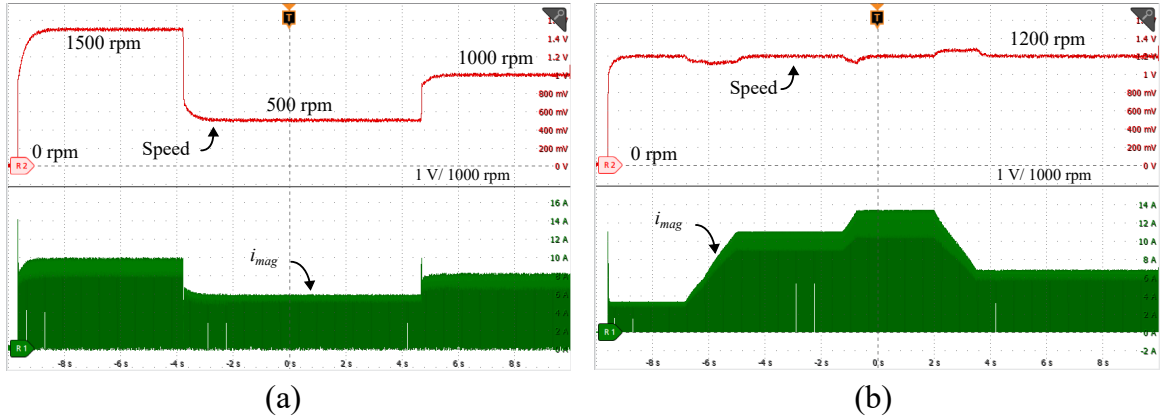


Figure 3.21: Experimental results showing speed waveforms and current through the magnetizing path (i_{mag}) during dynamic changes. (a) Dynamic waveforms for step changes in reference speed (1500 rpm, 500 rpm, and 1000 rpm). (b) Waveforms for dynamic changes in the load torque.

To examine the transient behavior of the proposed drive, its performance is analyzed with a step change in the speed reference. The speed is displayed on the DSO by configuring the Digital-to-Analog Converter (DAC) channel within the DSP microcontroller. In Figure 3.20, transient speed waveforms and current through the magnetizing path (i_{mag}) for step changes in speed reference are presented. Figure 3.20(a) illustrates transient waveforms for a step change in speed reference from 0 to 1200 rpm under no load conditions. The motor starts from rest and achieves the reference speed of 1200 rpm, stabilizing within 0.6 seconds with no overshoot. Figure 3.20(b) shows waveforms for a step change in speed reference from 1400 to 400 rpm under no load conditions, with the trajectory stabilizing at 400 rpm within 0.66 seconds, exhibiting a minor undershoot.

The dynamic behavior of the drive is further explored with variations in reference speed and load torque. Load torque is varied by adjusting the excitation to the DC machine coupled with the SRM, with the rheostat connected to the DC machine armature set to its maximum position. In Figure 3.21, waveforms of speed and current through the magnetizing path (i_{mag}) during dynamic changes in speed and load torque are presented. Figure 3.21(a) displays dynamic waveforms for step changes in reference speed (1500 rpm, 500 rpm, and 1000 rpm) starting from rest, with constant excitation and load resistance. Smooth speed trajectories are observed with no overshoots or undershoots. Figure 3.21(b) illustrates the speed and i_{mag} during constant speed operation (1200 rpm) with dynamic load changes. Variations in load

result in minor speed fluctuations, and the system tracks back to the reference speed without delay, indicating minimal overshoots or undershoots. These dynamic operation results align with simulation results, emphasizing the proposed drive's ability to operate under diverse conditions.

Experimental results align with simulation findings, further solidifying the observed robust performance of the drive system across various operating conditions, including steady state, dynamic, and transient scenarios. This confirms the effectiveness of the control design, demonstrating its consistent robustness under dynamic step speed and load torque variations.

3.6 Conclusions

This paper presents a systematic approach to digital control development for a four-phase SRM drive for medium power applications. Medium-power applications demand efficient and cost-effective control solutions for SRM drives. However, existing literature often lacks a detailed and comprehensive control development procedure, considering the need to minimize cost and complexity. Addressing this gap, this paper introduces a novel SRM drive combining a Miller converter-fed motor with a single current sensor, specifically designed for medium-power applications. A systematic control development procedure is presented for the drive, covering mathematical modeling of the motor and converter, design procedures, dynamic simulation, analysis, and experimental validation.

An accurate MATLAB Simulink simulation model of the SRM is obtained by FEA using Ansys. Subsequent parametric simulation studies is utilized for optimizing conduction angle. For control design, a reliable linear model of the SRM is obtained using small signal analysis. Speed and current controllers are then designed using the K-factor method. Additionally, the paper presents the detailed control algorithm developed, targeting the TMS320F28379D DSP microcontroller, for the proposed SRM drive.

Simulations and experiments effectively validate the proposed drive's performance across diverse operating conditions, including steady-state operation, dynamic speed changes, and transient load variations. Simulations confirmed the drive's effectiveness in both constant torque (below base speed) and constant power (above base speed) operating regions. Due to the DC machine's speed limit, experiments focused on

variable speed and load variations below base speed. These experiments demonstrated a settling time of around 1.6 seconds for a speed step change from 0 to 1200 rpm and around 1.66 seconds for a step change from 1400 to 400 rpm. Moreover, the experimental results showcase the drive's robust speed tracking even during dynamic speed changes and load variations, aligning with the simulation findings and validating its effectiveness.

Looking forward, further research could focus on position sensorless control strategies and torque ripple minimization strategies for medium-power applications. Although these strategies are discussed in the literature, further investigation into developing cost-effective strategies with reduced current sensors and computational intensity remains relevant.

Chapter 4

Ćuk Converter-fed SRM Drive with Accelerated Demagnetization and Integrated On-board Charging Capability for EVs

This chapter introduces a novel bidirectional dual-port Ćuk converter-fed SRM drive with integrated on-board charging capability, offering a cost-effective solution for electric vehicles (EVs). The proposed drive optimizes efficiency and reduces torque ripple through a modified v/f control strategy with an extended conduction angle. In driving mode, the v/f control strategy fundamental frequency switching, minimizing switching losses and core losses. This approach is complemented by utilizing the Ćuk converter as a front-end converter, providing variable magnetization voltage control for speed regulation and ensuring a higher demagnetization voltage to eliminate negative torque production, thereby enhancing the torque-ampere ratio. In grid-to-vehicle (G2V) mode, the SRM drive is reconfigured to act as a diode bridge followed by the Ćuk converter in reverse, functioning as a power factor correction (PFC) converter. This dual functionality of the proposed SRM drive significantly reduces costs and enhances the overall power density of the EV system. The paper details the control design procedure using a k-factor approach for both driving and G2V modes. Simulation and experimental results are provided to validate the effectiveness and practical viability of the proposed SRM drive, confirming its potential to address key challenges in EV technology.

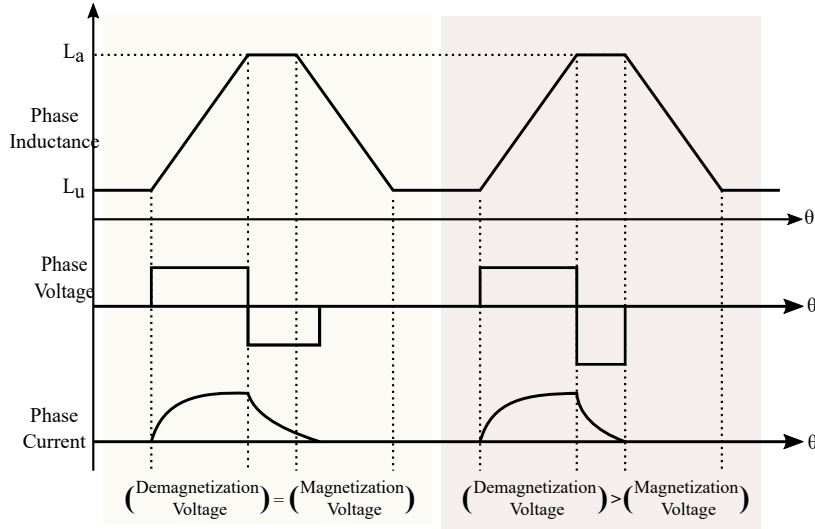


Figure 4.1: Theoretical waveforms showing variations in per phase inductance, voltage, and current with machine rotor angle for different demagnetization voltages.

4.1 Conventional SPC and Effect of Higher Demagnetization Voltage

In SPC, the phases are switched at the fundamental frequency, reducing the switching losses and core losses. In conventional SPC, the input DC voltage is fixed, and the speed control strategy involves controlling the conduction angle. This strategy has its own disadvantages of higher torque ripple due to lack of torque sharing at the commutation, especially at lower speeds. Hence, keeping the conduction angle constant and employing the input voltage strategy can effectively reduce the torque ripple at lower speeds and, hence, suitable for a wide range of speeds. The torque ripple can further be reduced with an extended conduction period with torque sharing between phases at the commutation. However, this can result in lower average torque due to slow demagnetization.

Theoretical waveforms of phase voltage and phase current against phase inductance in SPC with demagnetization voltage equal to the magnetization voltage, and higher demagnetization voltage are shown in Figure 4.1. In SRM, a positive voltage is applied when the phase is magnetized, and a negative voltage is applied during demagnetization. The effect of a higher demagnetization voltage can be understood theoretically from the voltage equation of the SRM. The voltage equation for an SRM

is given by:

$$v_{ph} = i_{ph}R_s + L_{ph}(\theta)\frac{di_{ph}(t)}{dt} + \omega_m i_{ph}(t)\frac{dL_{ph}(\theta)}{d\theta_m} \quad (4.1)$$

where v_{ph} , I_{ph} , ω_m , θ_m , R_s , and L_{ph} are the phase voltage, phase current, mechanical speed, mechanical angle, stator winding resistance, and phase self-inductance, respectively. As shown in Figure 4.1, at the phase turn-off instant (beginning of demagnetization), the phase inductance can be assumed to be equal to the aligned phase inductance value, and the slope of inductance can be assumed to be zero. Hence, during demagnetization, the voltage equation in (4.1) can be written as:

$$v_{dmag} = i_{ph}R_s + L_{ph}(\theta)\frac{di_{ph}(t)}{dt} \implies \frac{di_{ph}(t)}{dt} = \frac{v_{dmag} - i_{ph}R_s}{L_{ph}(\theta)}. \quad (4.2)$$

Here, v_{dmag} is the demagnetization voltage. In conventional SRM drives, as shown in Figure 4.1, the demagnetization voltage is equal to the negative of the input magnetization voltage. In this case, the rate of decay of the phase current is slow, leading to negative torque as it enters the negative torque region of the inductance characteristic. Employing an extended conduction period to reduce torque ripple can result in negative torque and, consequently, a reduced torque-ampere ratio. However, the higher the negative demagnetization voltage, the faster the decay rate of the phase current during demagnetization. Hence, this enables the employability of an extended conduction period for torque ripple reduction with a higher torque-ampere ratio.

To analyze these aspects in the SRM drive, a simulation using MATLAB Simulink is conducted. In order to perform simulations, the FEA-based simulation model is obtained. Ansys Maxwell is employed for the characterization of the SRM. The parameters of the SRM machine are shown in Table 2.1. The torque look-up table (torque(rotor angle, current)) and current look-up table (current(rotor angle, flux)) obtained from the SRM characterization are presented in Figure 2.3 and Figure 2.5. For the analysis of these aspects in SPC, an asymmetric H-Bridge (AHB) converter is used as the SRM converter.

Initially, a conventional SPC for a wide range of speeds is simulated to analyze the performance of the SRM drive. In this case, the conduction angle controls the speed. Figure 4.2 presents the simulation results for a constant input voltage of 180 V, showing phase voltages, phase currents, phase torques, and net torque at different

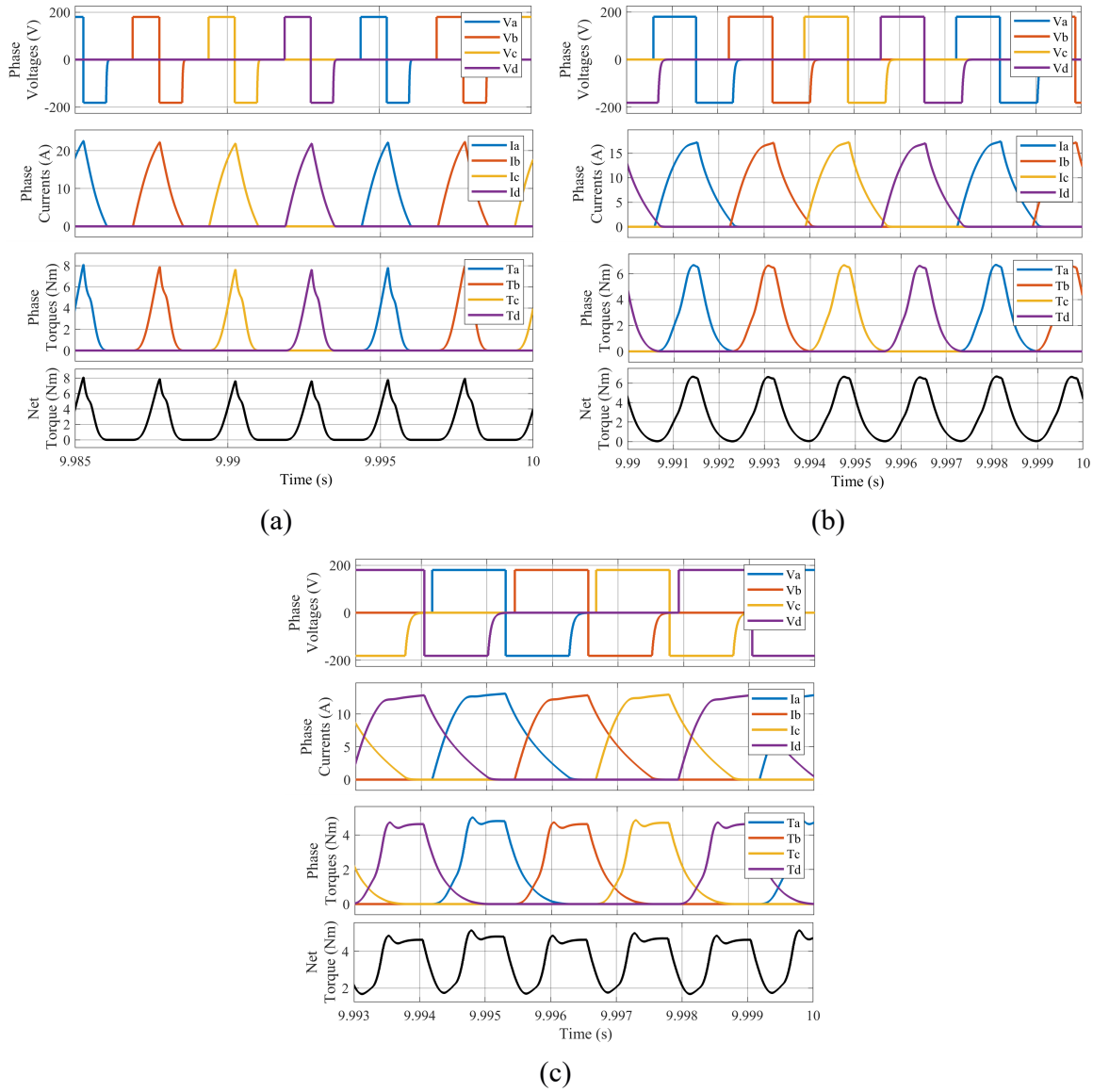


Figure 4.2: Simulation results for conventional SPC with variable conduction angle for controlling speed at different speeds of SRM drive. (a) Speed of 1000 rpm. (b) Speed of 1500 rpm. (c) Speed of 2000 rpm.

speeds. At 1000 rpm, as depicted in Figure 4.2(a), with an input voltage of 180 V, the net torque exhibits discontinuity. At 1500 rpm, as shown in Figure 4.2(b), the net torque is nearly continuous with high torque ripple. Conversely, at 2000 rpm, as illustrated in Figure 4.2(c), the net torque is continuous, and the torque ripple is reduced. It can be inferred that torque ripple at commutation significantly diminishes as the speed increases due to torque sharing between phases during commutation.

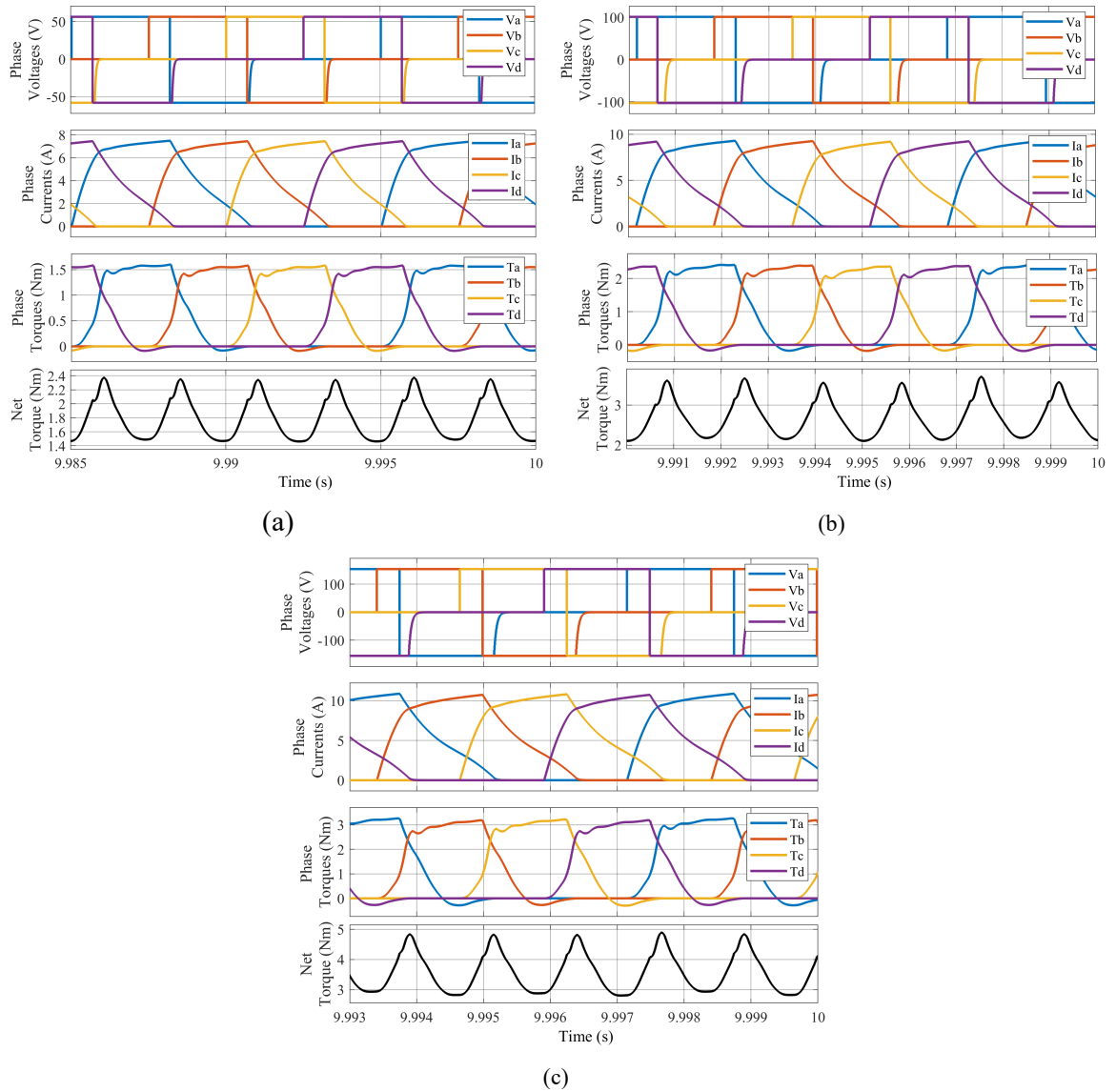


Figure 4.3: Simulation results for v/f control with constant conduction period (18.25°) and demagnetization voltage equal to the magnetization voltage at different speeds of the SRM drive. (a) Speed of 1000 rpm. (b) Speed of 1500 rpm. (c) Speed of 2000 rpm.

Additionally, it is observed that, with a fixed input voltage, the motor core is more likely to get saturated at lower speeds since the back emf is low at lower speeds.

Therefore, the variable conduction period is not suitable for variable speed drives across a wide range of speed variations. Consequently, it is imperative to employ v/f control. To analyze the performance of the SRM drive in v/f control, a fixed conduction angle of 18.25° is employed. This fixed conduction angle is chosen for

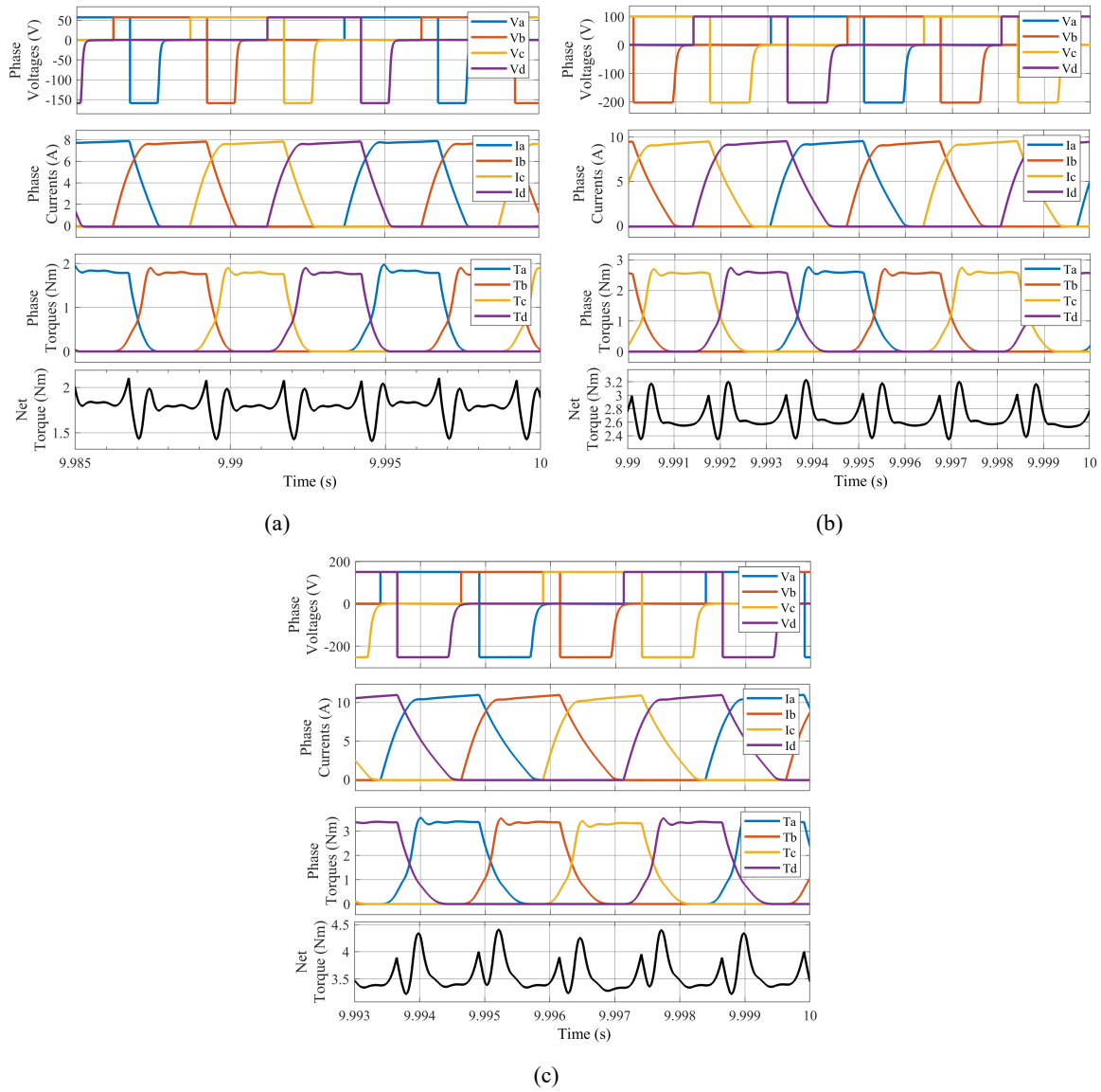


Figure 4.4: Simulation results for v/f control with constant conduction period (18.25°) and higher demagnetization voltage at different speeds of the SRM drive. (a) Speed of 1000 rpm. (b) Speed of 1500 rpm. (c) Speed of 2000 rpm

analysis purposes, allowing torque sharing between phases during phase commutation. Figure 4.3 presents simulation results showing phase voltages, phase currents, phase torques, and net torques at different speeds. Regardless of the speed of the SRM drive, torque ripple is reduced with respect to conventional SPC. However, negative torque is observed across all speeds due to slow demagnetization. This can impact the torque-ampere ratio of the SRM drive. This aligns with the theoretical analysis

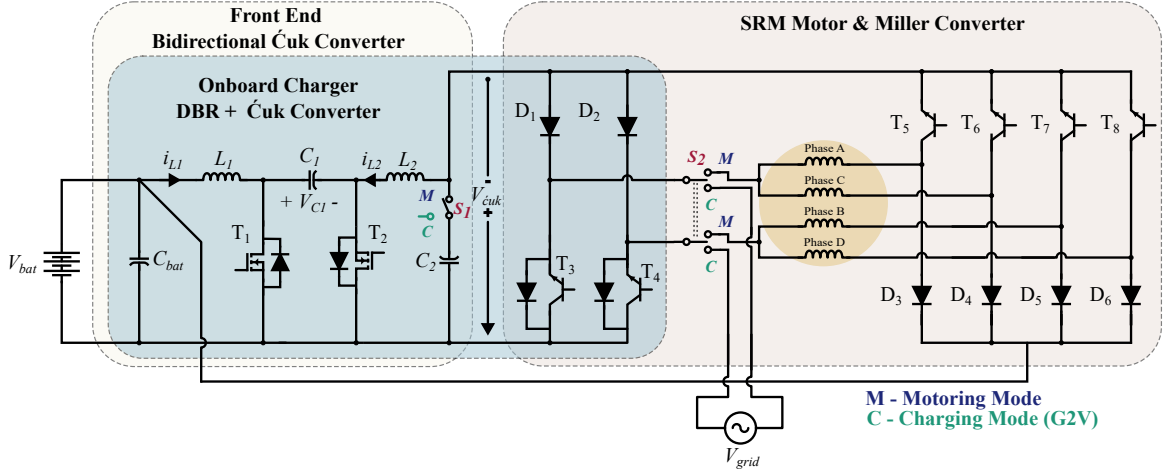


Figure 4.5: Configuration of the proposed onboard power converter for the SRM Drive-based EV with integrated onboard charging capability (Switch S closed at position M for motoring mode and position C for charging mode).

above.

The negative torque production can be eliminated by accelerating demagnetization. Therefore, with higher demagnetization, a wider conduction angle can be employed to reduce torque ripple at commutation. To achieve faster demagnetization, the demagnetization path is decoupled to connect to a higher negative voltage. Figure 4.4 presents simulation results for v/f control with a fixed conduction angle of 18.25° and a demagnetization voltage 100 V higher than the input magnetization voltage. It can be observed that negative torque is eliminated, and torque ripple is significantly reduced. Hence, v/f control with a higher demagnetization voltage helps to achieve reduced torque ripple at commutation with a higher torque ampere ratio.

The v/f control strategy of SRM, in addition to the advantages of SPC, overcomes the inherent disadvantages of SPC at low speeds. The higher demagnetization voltage allows an extended conduction period, further reducing torque ripple at commutation. This necessitates a front-end converter with a decoupled demagnetization path and a higher demagnetization voltage.

4.2 Proposed SRM Drive

The power converter designed for the proposed SRM drive, equipped with integrated onboard charging capability, is illustrated in Figure 4.5. This converter offers func-

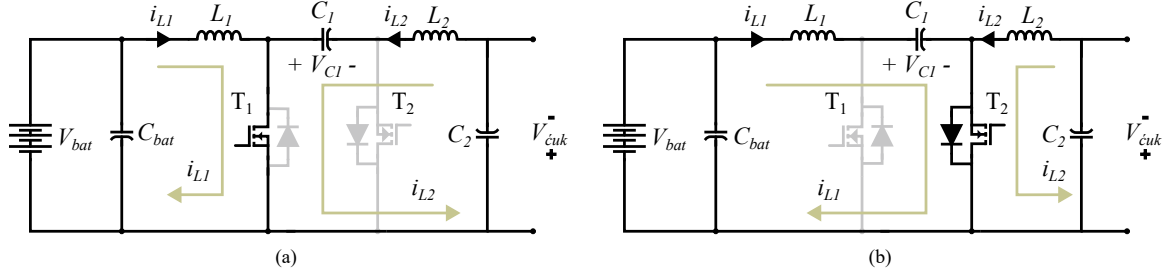


Figure 4.6: Modes of operation of the Ćuk converter in motoring mode. (a) When T_1 is ON and T_2 is OFF. (b) When T_1 is OFF and T_2 is ON.

tionality across motoring, regenerative braking, and Grid-to-Vehicle (G2V) charging modes. It comprises a bidirectional Ćuk converter at the front end, followed by a modified Miller converter featuring a decoupled demagnetization path, with a higher demagnetization voltage specifically tailored for the motoring mode. When operating in G2V mode, the converter is reconfigured to get a two-stage, non-isolated charger topology, with a diode bridge followed by a Ćuk converter. The subsequent sections elaborate on the operational modes of this converter.

4.2.1 Motoring and regenerative braking modes

During motoring and regenerative braking, switches S_1 and S_2 are connected to position M . The Ćuk converter functions in forward mode, transferring power from the battery to the SRM inverter. The operational modes of the Ćuk converter in the motoring mode are depicted in Figure 4.6. As illustrated in Figure 4.6(a), when T_1 is ON, T_2 is OFF, and the reverse diode of T_2 is reverse-biased. During this mode, inductor L_1 charges through T_1 , while capacitor C_1 discharges through T_1 , simultaneously charging inductor L_2 . Conversely, as in Figure 4.6(b), when T_1 is OFF, T_2 is ON, and the diode of T_2 is forward-biased. Here, inductor L_1 discharges through T_2 , charging capacitor C_1 , while inductor L_2 connects to the output through T_1 . The output voltage of the Ćuk converter is determined by the formula:

$$V_{\acute{c}uk} = \frac{D}{(1-D)} V_{bat}. \quad (4.3)$$

The operation modes of the SRM converter for phase A in motoring mode are depicted in Figure 4.7. As shown in Figure 4.7(a), during magnetization, T_3 and T_5 are turned ON to apply the output voltage of the Ćuk converter ($V_{\acute{c}uk}$) across

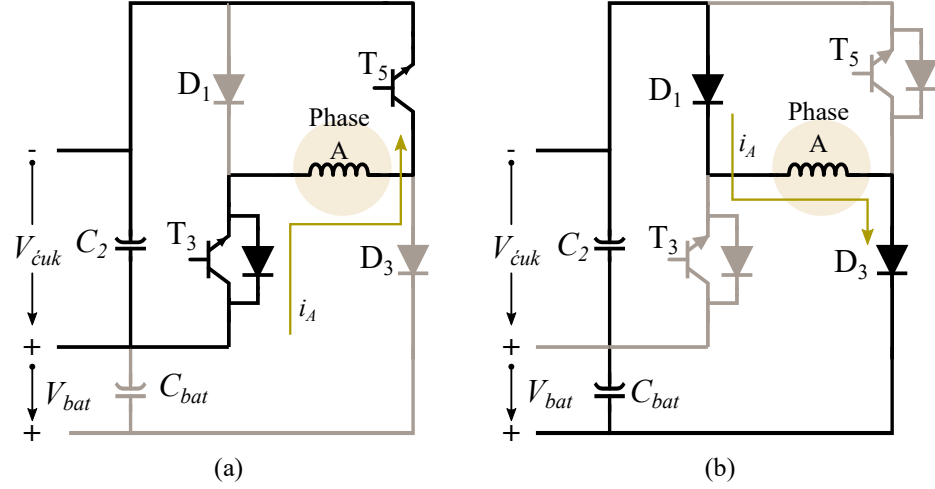


Figure 4.7: Modes of operation for one phase of SRM converter in motoring mode. (a) Magnetization mode. (b) Demagnetization mode.

the phase windings. Conversely, in Figure 4.7(b), during commutation, when both are OFF, D_1 and D_3 conduct, applying a higher demagnetization voltage equal to the sum of the battery voltage and the output voltage of the Ćuk converter. The magnetization and demagnetization voltages are given by the following equations:

$$\text{Magnetization Voltage} = V_{\acute{c}uk} = \frac{D}{(1-D)} V_{bat} \quad (4.4)$$

$$\text{Demagnetization Voltage} = -(V_{\acute{c}uk} + V_{bat}) = \frac{-V_{bat}}{(1-D)} \quad (4.5)$$

Furthermore, the Ćuk converter offers the advantage of continuous input and output currents, thereby reducing the required size of the capacitor at the input of the SRM converter.

Consequently, the drive operates under v/f control with an extended conduction period. The speed is controlled by a variable output voltage of the Ćuk converter ($V_{\acute{c}uk}$). The higher demagnetization voltage ensures a higher torque-ampere ratio, facilitating accelerated demagnetization.

4.2.2 Grid-to-Vehicle (G2V) charging mode

Disconnecting the motor windings in parking mode is a standard practice for EVs when the vehicle is stationary. During charging mode, the vehicle remains stationary.

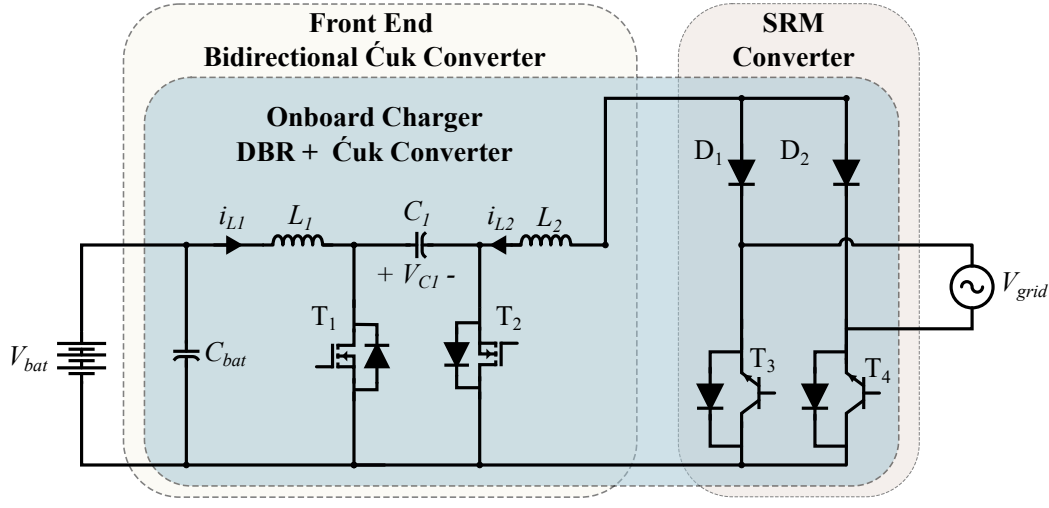


Figure 4.8: Converter in grid-to-vehicle battery charging (G2V) mode

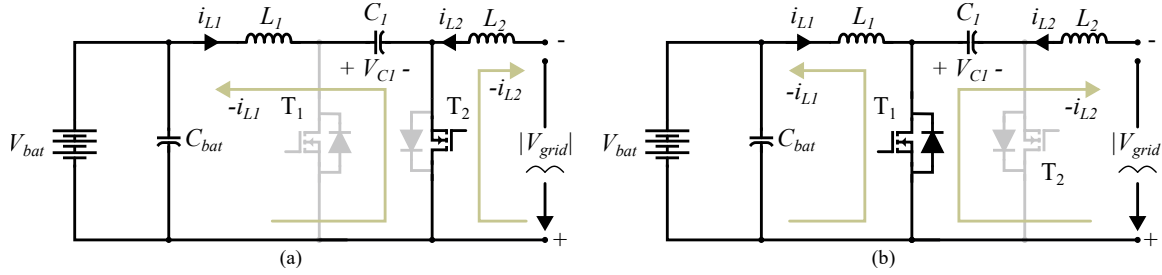


Figure 4.9: Operating modes of the power converter in grid-to-vehicle (G2V) battery charging mode. (a) When T_2 is ON and T_1 is OFF. (b) When T_2 is OFF and T_1 is ON.

Additionally, switch S_1 is positioned at 'C' to disconnect capacitor C_2 from the charging circuit. The reconfigured converter in Grid-to-Vehicle (G2V) mode is depicted in Figure 4.8. In G2V mode, the SRM converter functions as a diode bridge rectifier, while the Ćuk converter serves as a PFC converter [Bodetto et al. \(2015\)](#), regulating the charging voltage and current.

During G2V mode, the rectified voltage is applied across the Ćuk converter, illustrated in Figure 4.9. The operating modes of the Ćuk converter in G2V mode mirror those described in motoring mode (as in Figure 4.6), though in reverse, as depicted in Figure 4.9. Here, switch T_2 governs the input current and, consequently, the input current power factor. The continuous input and output currents of the Ćuk converter ensure a high input current power factor and lower current ripple in the battery current.

4.3 Front-end Converter Design

The front-end Ćuk converter must be carefully designed to meet the requirements of both driving and charging modes. Table 2.1 outlines the machine parameters essential for the design process.

For a target power of 1 kW, with an input voltage (V_{bat}) of 100 V and an output voltage ($V_{\acute{c}uk}$) of 160 V, the duty cycle (D) required for the output voltage of 160 V is calculated as follows:

$$D = \frac{V_{\acute{c}uk}}{(V_{bat} + V_{\acute{c}uk})} = .61 \quad (4.6)$$

The design of the Ćuk converter is based on fundamental voltage and current equations Hart (2011), with a targeted switching frequency (f_s) of 20 kHz.

The design specifications for the inductor L_1 include a current (I_{L_1}) of 10 A and a ripple (Δ) of 25%. The calculated value is:

$$L_1 = \frac{V_{bat}D}{\Delta I_{L_1} f_s} = 1.2 \text{ mH} \approx 1 \text{ mH}. \quad (4.7)$$

Similarly, for inductor L_2 , with a current (I_{L_2}) of 6.25 A and a ripple (Δ) of 25%, we have:

$$L_2 = \frac{V_{bat}D}{\Delta I_{L_2} f_s} = 2 \text{ mH}. \quad (4.8)$$

The voltage across capacitor C_1 is given by:

$$V_{C_1} = (V_{bat} + V_{\acute{c}uk}) = 260 \text{ V}. \quad (4.9)$$

Hence, capacitor C_1 should be designed for a voltage of 260 V, with a voltage ripple (ΔV_{C_1}) of 15%. The required capacitance is:

$$C_1 = \frac{D I_{L_2}}{\Delta V_{C_1} f_s} = 4.8 \text{ } \mu\text{F} \approx 5 \text{ } \mu\text{F} \quad (4.10)$$

For capacitor C_2 , which serves in the driving mode, the design considerations include a minimum speed (N_{min}) of 200 rpm, a minimum output power (P_{min}) of 100 W, a minimum voltage (V_{min}) of 20 V, and a voltage ripple ($\Delta V_{\acute{c}uk}$) of 2.5%. The calculated capacitance is:

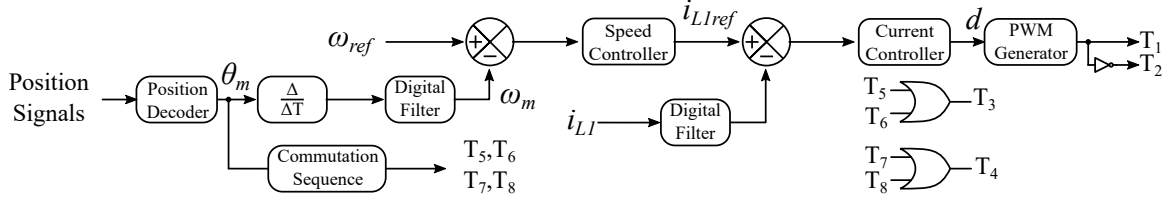


Figure 4.10: Control logic block diagram for motoring mode.

$$C_2 \geq \frac{P_{min}}{f_s V_{min}^2 \Delta V_{cuk}} = 1000\mu F \approx 1200\mu F. \quad (4.11)$$

In the charging mode, capacitor C_{bat} across the battery is pivotal. Assuming a voltage drop of 20-24 V at full discharge, the minimum battery voltage ($V_{bat-min}$) is approximated at 76 V. The capacitor C_{bat} is designed for the worst-case scenario where the battery charges at $V_{bat-min}$ with the rated charging power (P_{charge}) of 1 kW. The desired voltage ripple ΔV_{bat} is set at 10% for the grid frequency (f) of 50 Hz.

$$C_{bat} \geq \frac{P_{charge}}{4\pi f V_{bat-min}^2 \Delta V_{bat}} = 2800\mu F \approx 3300\mu F. \quad (4.12)$$

With these specifications, the converter ensures efficient operation in both driving and charging modes.

4.4 Control Design

4.4.1 Motoring mode

The control block diagram for motoring mode is depicted in Figure 4.10. In this mode, the SRM converter operates at the fundamental frequency to facilitate winding commutation. The drive's adjustable speed functionality is achieved through control of the front-end converter's output. The rotor's position is sensed using a position encoder. As illustrated in Figure 4.10, the obtained rotor position dictates the switching of the IGBTs in the SRM converter based on the predetermined commutation sequence. The rotor's speed, derived from the position data, undergoes noise filtration via a digital filter. The filtered speed is then compared to the speed reference and forwarded to the speed controller, yielding a reference input current (i_{L1ref}).

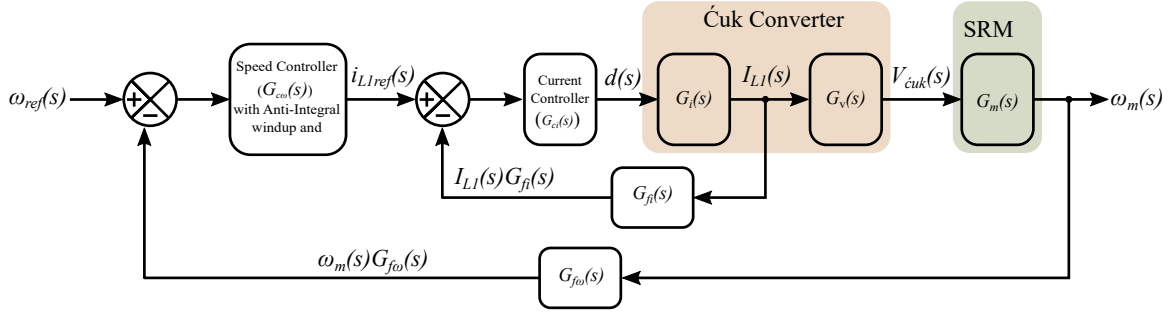


Figure 4.11: Control block diagram for the SRM drive in the motoring mode

Subsequently, the measured current (i_{L1}) passing through inductor L_1 goes through low pass filter and is compared with i_{L1ref} . This comparison result is then passed to the current controller, which determines the duty cycle for switch T_1 . The pulse width modulation (PWM) generator generates two complementary pulses, driving switches T_1 and T_2 , respectively.

The control development process entails designing speed and current controllers, alongside optimizing the conduction angle. This optimization aims to reduce torque ripple and enhance drive efficiency.

4.4.1.1 System transfer function

The control block diagram is illustrated in Figure 4.11. To begin the linear control design process, we need to obtain the system transfer functions. This involves deriving the small signal models for the SRM and the front-end Ćuk converter followed by the derivation of that of feedback LPFs. The small signal model of the SRM motor based on linear approximation ignoring saturation is derived as in (2.13). With the SRM small signal model, the front-end converter transfer function.

The small signal model for the Ćuk converter in the motoring mode (in forward direction) is obtained from voltage and current equations [Erickson and Maksimovic](#)

(2007). The state space representation is given as below:

$$\begin{bmatrix} \frac{d\hat{i}_{L1}}{dt} \\ \frac{d\hat{i}_{L2}}{dt} \\ \frac{d\hat{v}_{C1}}{dt} \\ \frac{d\hat{v}_{\acute{c}uk}}{dt} \end{bmatrix} = \begin{bmatrix} 0 & 0 & \frac{-D'}{L_1} & 0 \\ 0 & 0 & \frac{D}{L_2} & \frac{1}{L_2} \\ \frac{D'}{C_1} & \frac{-D}{C_1} & 0 & 0 \\ 0 & \frac{-1}{C_2} & 0 & \frac{-1}{C_2 R_t} \end{bmatrix} \begin{bmatrix} \hat{i}_{L1} \\ \hat{i}_{L2} \\ \hat{v}_{C1} \\ \hat{v}_{\acute{c}uk} \end{bmatrix} + \begin{bmatrix} \frac{V_{C1}}{L_1} \\ \frac{V_{C1}}{L_1} \\ \frac{-(I_{L1} + I_{L2})}{C_1} \\ 0 \end{bmatrix} \hat{d}. \quad (4.13)$$

All the variables are defined in the converter design of the Ćuk converter in previous section. Hence, the state matrix and the input matrix of the system is obtained. Following are the output equations:

$$Y_i = \begin{bmatrix} 1 & 0 & 0 & 0 \end{bmatrix} \begin{bmatrix} \hat{i}_{L1} \\ \hat{i}_{L2} \\ \hat{v}_{C1} \\ \hat{v}_{\acute{c}uk} \end{bmatrix} \quad (4.14)$$

$$Y_v = \begin{bmatrix} 0 & 0 & 0 & 1 \end{bmatrix} \begin{bmatrix} \hat{i}_{L1} \\ \hat{i}_{L2} \\ \hat{v}_{C1} \\ \hat{v}_{\acute{c}uk} \end{bmatrix} \quad (4.15)$$

From these, the input current transfer function (G_i) and the output transfer function ($G_{\acute{c}uk}$) are derived, which allows us to obtain the voltage transfer function (G_v). The obtained transfer functions are shown below:

$$G_i(s) = \frac{i_{L1}(s)}{d(s)} \quad (4.16)$$

$$G_{\acute{c}uk}(s) = \frac{V_{\acute{c}uk}(s)}{d(s)} \quad (4.17)$$

$$G_v(s) = \frac{G_{\acute{c}uk}}{G_i(s)} = \frac{V_{\acute{c}uk}(s)}{i_{L1}(s)} \quad (4.18)$$

To attenuate high-frequency components, the current and speed feedback systems employ low-pass filters (LPFs). These LPFs are designed as first-order filters with specific time constants. The current feedback transfer function, $G_{fi}(s)$, corresponds to a pole at 8 kHz, ensuring that it eliminates frequencies beyond this point. Its expression is given by:

$$G_{fi}(s) = \frac{1}{1 + s\tau_{fi}}; \tau_{fi} = \frac{1}{2\pi; 8000}. \quad (4.19)$$

Similarly, the speed feedback transfer function, $G_{f\omega}(s)$, also acts as a first-order low-pass filter, with a pole at 1000 Hz, effectively filtering out high-frequency noise:

$$G_{f\omega}(s) = \frac{1}{1 + s\tau_{f\omega}}; \tau_{f\omega} = \frac{1}{2\pi; 1000}. \quad (4.20)$$

Now, the plant transfer functions for both the current and speed controller design are obtained. The plant transfer function for the current controller, $G_{pi}(s)$, is obtained by multiplying the current feedback transfer function, G_{fi} , with the input current transfer function, $G_i(s)$:

$$G_{pi}(s) = G_{fi} \cdot G_i(s). \quad (4.21)$$

Likewise, the plant transfer function for the speed controller, $G_{p\omega}(s)$, incorporates the speed feedback transfer function, $G_{f\omega}$, and the voltage transfer function, G_v :

$$G_{p\omega}(s) = \frac{G_{ci} \cdot G_i}{1 + G_{ci} \cdot G_i \cdot G_{fi}} \cdot G_v \cdot G_m \cdot G_{f\omega}. \quad (4.22)$$

Having obtained the plant transfer functions, next is design of current and speed controller.

4.4.1.2 Design of current and speed controller

For the obtained plant transfer functions, type II compensators are designed using the K-Factor approach [Venable \(1983\)](#). A type II compensator is given by:

$$G_c(s) = \frac{A s + \omega_z}{s s + \omega_p}. \quad (4.23)$$

The design of controller using K-factor approach involves calculating the phase boost necessary for the loop transfer function to achieve the desired phase margin at the

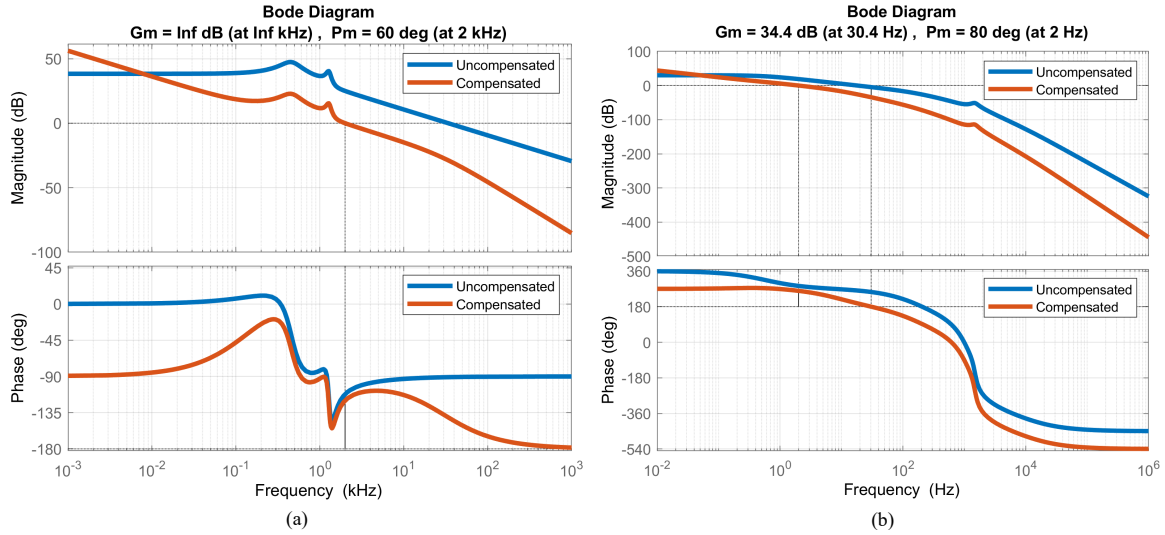


Figure 4.12: Bode plots of uncompensated and compensated systems. (a) Current control loop: plant transfer function (G_{pi}) and loop transfer function ($G_{pi} \cdot G_{ci}$). (b) Speed control loop: plant transfer function ($G_{p\omega}$) and loop transfer function ($G_{p\omega} \cdot G_{c\omega}$) for closed-loop speed control.

controller cutoff frequency. Subsequently, the controller zero (ω_z) and pole (ω_p) are determined, and the controller gain (A) is adjusted to achieve unity gain at the controller cutoff frequency.

Initially, the current controller is designed for the current loop plant transfer function in (4.21), targeting a bandwidth of 2 kHz and a phase margin of 60° . The resulting bode plot for both the plant transfer function (G_{pi}) and the loop transfer function ($G_{pi} \cdot G_{ci}$) is depicted in Figure 4.12(a).

Similarly, the speed controller for the plant transfer function in (4.22) is designed to operate at a bandwidth of 2 Hz with a desired phase margin of 80° . Figure 4.12(b) illustrates the bode plots for the plant transfer function ($G_{p\omega}$) and its corresponding loop transfer function ($G_{p\omega_m} \cdot G_{c\omega}$).

4.4.1.3 Selection of conduction angle

After developing the speed and current controllers, selecting the conduction angle becomes crucial to minimize torque ripple. Here, the conduction angle is selected to achieve least torque ripple at rated speed and torque. A MATLAB Simulink simulation of the proposed SRM drive is conducted at rated speed and torque, varying conduction angles. As evident from Figure 4.13(a), the inductance value is low near

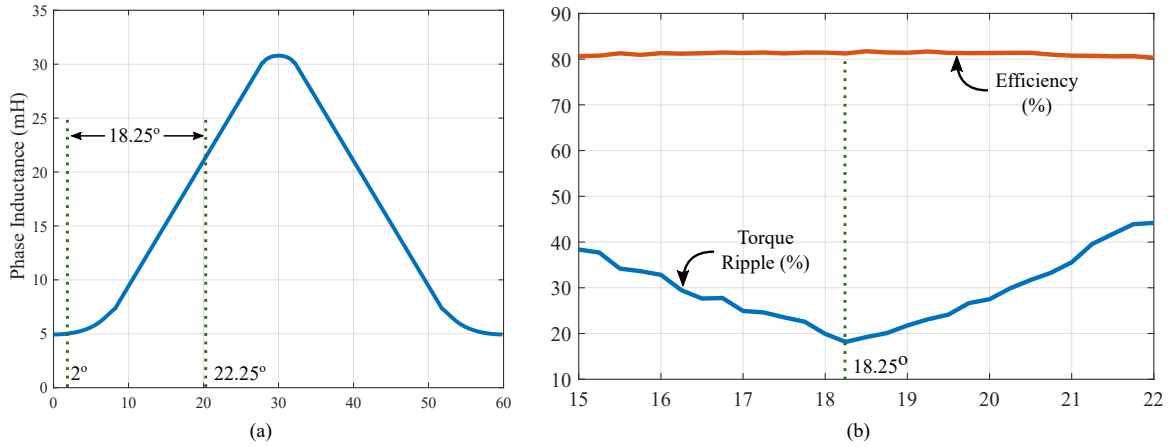


Figure 4.13: Plots showing the effect of variation in conduction angle. (a) Inductance profile of phase A showing the conduction angle of 18.25° . (b) Plot showing efficiency and torque ripple for various conduction angles.

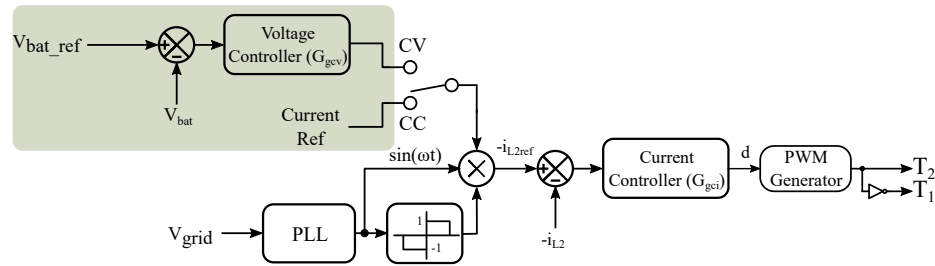


Figure 4.14: Control block diagram for constant current and constant voltage modes of operation in G2V charging mode

unaligned position, so phase current increases fast near the unaligned position. Hence the turn-on angle is fixed to 2° to ensure fast initial magnetization. Efficiency and torque ripple are then derived from the simulation data. Plotting the efficiency and torque ripple against the employed conduction angles (Figure 4.13(b)) reveals that efficiency remains relatively stable while torque ripple varies significantly. The lowest torque ripple, 18.3%, is observed at a conduction angle of 18.25° . Consequently, the conduction angle is set to 18.25° , with a turn-off angle of 20.25° , maintaining the turn-on angle at 2° .

4.4.2 G2V charging mode

The control block diagram depicted in Figure 4.14 illustrates the operation of the charger, which can function in constant voltage (CV) and constant current (CC)

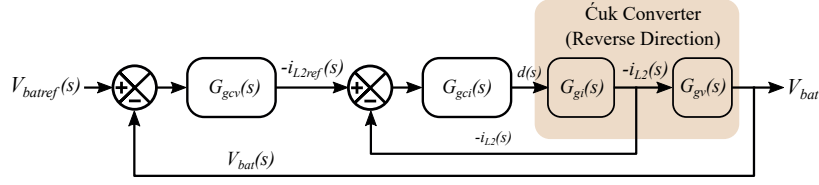


Figure 4.15: Control model block diagram for constant voltage mode of operation in G2V charging mode

modes. During CV mode, the battery voltage is compared with a reference battery voltage, and this error is fed to the voltage controller to determine the peak current reference. Conversely, in CC mode, the peak current reference is directly provided. Next, the reference peak current is multiplied by the output of the phase-locked loop (PLL), and the result is further multiplied by the sign of the grid voltage to generate a rectified sine reference. This reference is then compared with the measured current through the inductor, L_2 ($-i_{L2}$), and the resultant error goes to the current controller to compute the duty cycle for switch T_2 . The complementary pulse is then directed to T_1 .

4.4.3 Derivation of system model

As shown in Figure 4.8, the Cuk converter operates in reverse mode in G2V mode. The control model block diagram is shown in Figure 4.15. Here, the transfer function should be obtained for the converter in reverse mode. As in motoring mode, the small signal model can be obtained as below:

$$\begin{bmatrix} \frac{-d\hat{i}_{L1}}{dt} \\ \frac{-d\hat{i}_{L2}}{dt} \\ \frac{d\hat{v}_{C1}}{dt} \\ \frac{d\hat{v}_{cuk}}{dt} \end{bmatrix} = \begin{bmatrix} 0 & 0 & \frac{-D'}{L_2} & 0 \\ 0 & 0 & \frac{D}{L_1} & \frac{1}{L_1} \\ \frac{D'}{C_1} & \frac{-D}{C_1} & 0 & 0 \\ 0 & \frac{-1}{C_{bat}} & 0 & \frac{-1}{C_{bat}R_l} \end{bmatrix} \begin{bmatrix} -\hat{i}_{L2} \\ -\hat{i}_{L1} \\ \hat{v}_{C1} \\ \hat{v}_{bat} \end{bmatrix} + \begin{bmatrix} \frac{V_{C1}}{L_1} \\ \frac{V_{C1}}{L_1} \\ \frac{(I_{L1} + I_{L2})}{C_1} \\ 0 \end{bmatrix} \hat{d}. \quad (4.24)$$

All the variables are defined in the converter design of the Ćuk converter in previous section. Hence, the state matrix and the input matrix of the system is obtained. Following are the output equations:

$$Y_i = \begin{bmatrix} 1 & 0 & 0 & 0 \end{bmatrix} \begin{bmatrix} -\hat{i}_{L2} \\ -\hat{i}_{L1} \\ \hat{v}_{C1} \\ \hat{v}_{bat} \end{bmatrix} \quad (4.25)$$

$$Y_v = \begin{bmatrix} 0 & 0 & 0 & 1 \end{bmatrix} \begin{bmatrix} -\hat{i}_{L2} \\ -\hat{i}_{L1} \\ \hat{v}_{C1} \\ \hat{v}_{bat} \end{bmatrix} \quad (4.26)$$

From these, the input current transfer function (G_{gi}) and the output transfer function (G_g) are derived, which allows us to obtain the voltage transfer function (G_{gv}). The obtained transfer functions are shown below:

$$G_{gi}(s) = \frac{-i_{L2}(s)}{d(s)} \quad (4.27)$$

$$G_g(s) = \frac{V_{bat}(s)}{d(s)} \quad (4.28)$$

$$G_{gv}(s) = \frac{G_g(s)}{G_{gi}(s)} = \frac{V_{bat}(s)}{-i_{L2}(s)} \quad (4.29)$$

From Figure 4.15, the plant transfer function is given in (4.27). The plant transfer function for voltage outer loop in CV mode is as given below:

$$G_{gpv}(s) = \frac{G_{gci} \cdot G_{gi}}{1 + G_{gci} \cdot G_{gi}} \cdot G_{gv}. \quad (4.30)$$

4.4.4 Design of voltage and current controller

After determining the system's transfer functions, the current controller, G_{gci} , is obtained. A type 2 compensator (as in (4.23)) is specifically designed for the plant transfer function, G_{gi} , using the K-factor method to achieve a target closed-loop bandwidth of 4 kHz and a phase margin of 60°. The Bode plots for both compensated and uncompensated systems are illustrated in Figure 4.16(a). Similarly, the voltage

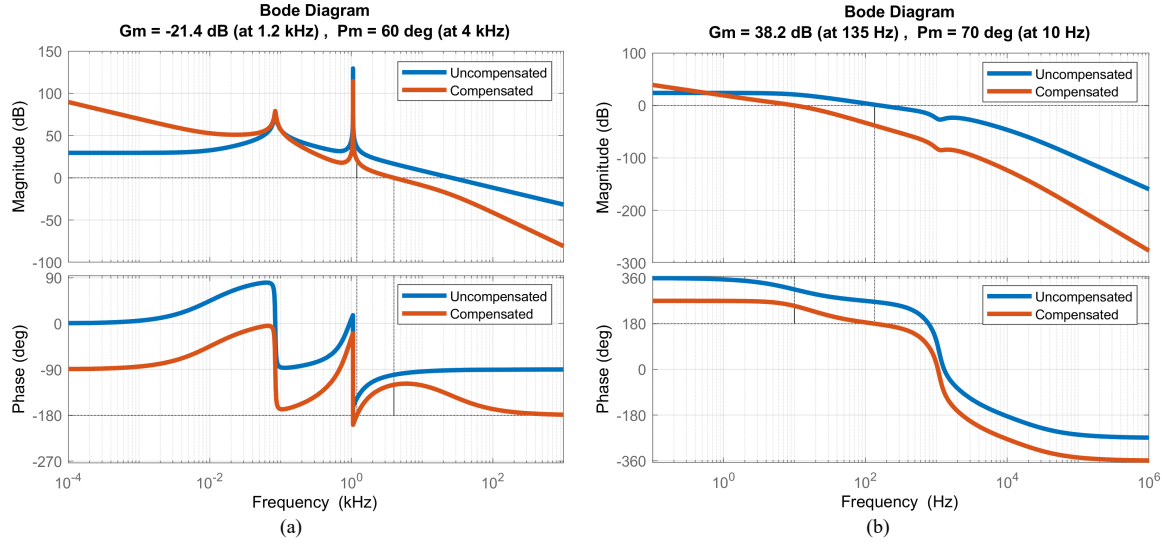


Figure 4.16: Bode plots of uncompensated and compensated systems for G2V mode. (a) Current control loop: plant transfer function (G_{gi}) and loop transfer function ($G_{gi} \cdot G_{gci}$). (b) Speed control loop: plant transfer function (G_{gpv}) and loop transfer function ($G_{gpv} \cdot G_{gcv}$) for closed-loop voltage control in CV mode.

controller (G_{gcv}) gains for CV mode are determined for a desired bandwidth of 10 Hz with a desired phase margin of 70°. The Bode plots for the compensated and uncompensated systems are depicted in Figure 4.16(b).

4.5 Simulation Results

The operation of the proposed SRM drive and the designed control is validated using simulations. A MATLAB Simulink model of the SRM drive, which was described in Section 4.1, is used for the simulation studies. The parameters for the Čuk converter used in the simulations are the same as those derived in Section 4.3. The simulation results for motoring and G2V charging modes are presented in subsequent sections.

4.5.1 Motoring Mode

Extensive motoring mode simulations (Figure 4.17) evaluate the proposed SRM drive controller's robustness across diverse operating conditions. Constant torque (below base speed) and constant power (above base speed) regions are explored through step changes in reference speed, load torque, and input battery voltage. These assess

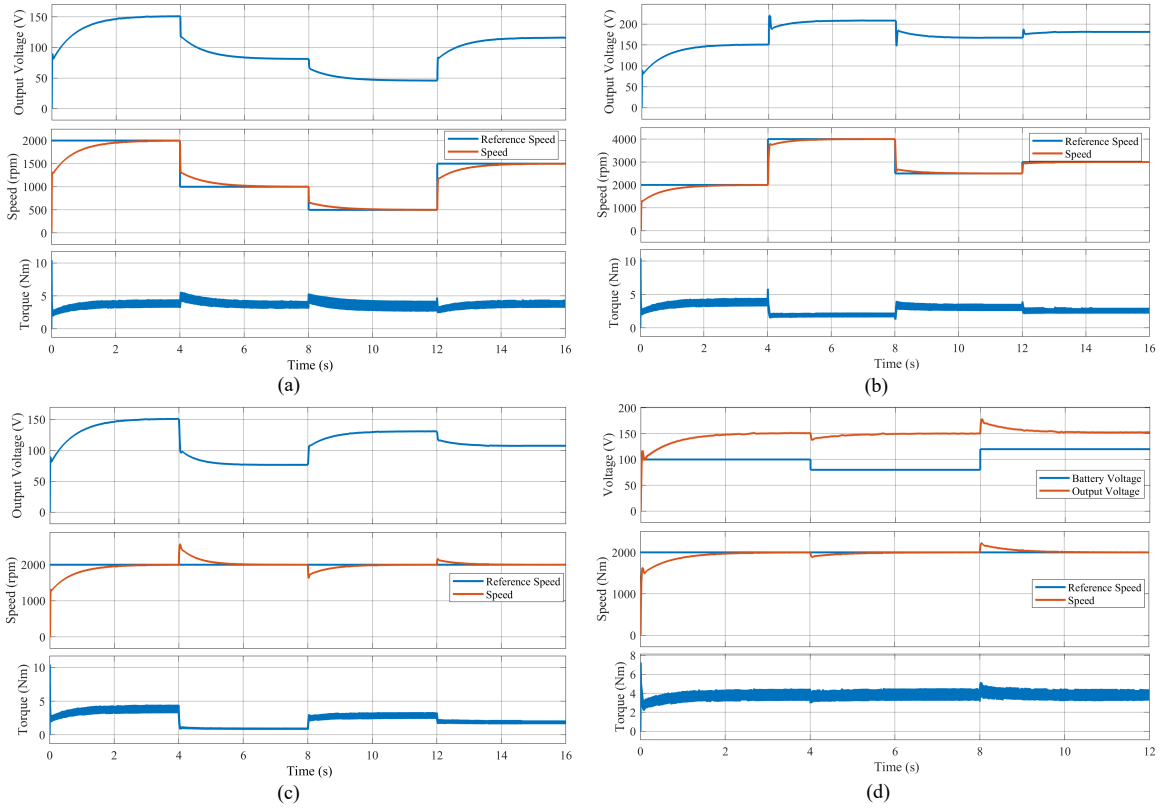


Figure 4.17: Simulation results showing the voltage output of the Ćuk converter ($V_{\check{c}uk}$), rotor speed generated electromagnetic torque during dynamic operating conditions. (a) Step variations in speed reference (2000 rpm, 1000 rpm, 500 rpm, and 1500 rpm) at constant rated torque. (b) Step variations in speed reference above base speed (2000 rpm, 4000, rpm, 2500 rpm, and 3000 rpm) in constant power mode. (c) Step variations in load at constant speed. (d) Step variation in input battery voltage (100 V, 80 V, 120 V) at rated speed and torque.

the controller’s ability to track commands, handle fluctuating loads, and maintain stability under varying power supply conditions, thereby comprehensively validating its robustness against external disturbances.

As showcased in Figure 4.17(a), fixed step changes in speed reference (ranging from 2000 to 500 rpm) at constant torque reveal accurate tracking within 2 seconds. Similar performance is observed at higher speeds (2000 to 4000 rpm) in constant power mode (Figure 4.17(b)), further emphasizing the controller’s adaptability to different conditions. The controller demonstrates speed tracking capabilities, achieving fast settling times without overshoot under both constant torque and constant power operations.

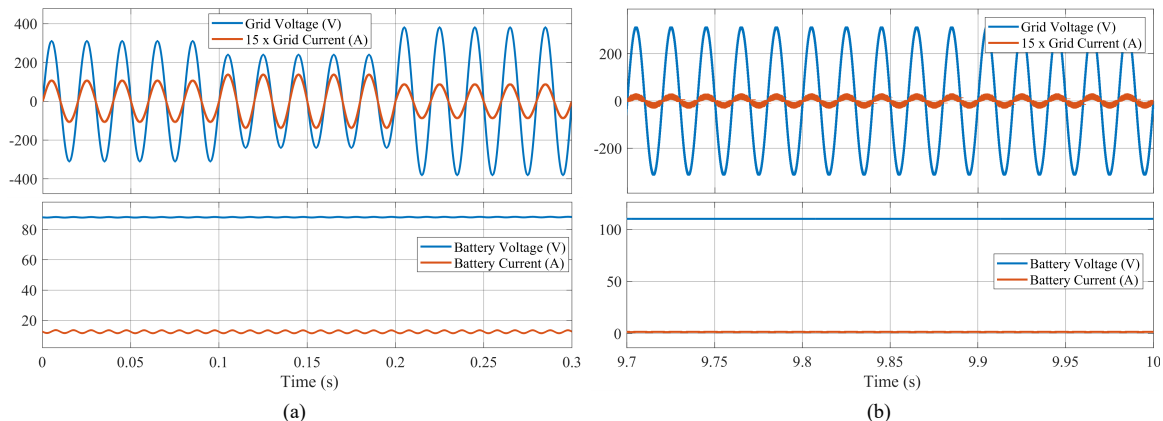


Figure 4.18: Simulation results showing grid voltage, grid current, battery voltage, battery current in G2V charging mode in dynamic conditions. (a) Dynamic variations in input grid voltage (220 V, 170 V, and 270 V). (b) Dynamic Variations in input current in slow charging in CV mode.

To evaluate the robustness of the controller, the response of the drive for step changes in load and battery voltage are evaluated. Figure 4.17(c). The simulation results show robust tracking of the reference speed of 2000 rpm after transient load changes. Also, for a step variations in the battery voltage from 100 V to 80 V to 120 V, the robustness of the controller is analysed and the results are presented in Figure 4.17(d). The simulation results show robust tracking of the reference speed despite transient changes in the input voltage.

Figure 4.17(c) demonstrates effective rejection of load torque fluctuations, ensuring consistent reference speed tracking (2000 rpm). Additionally, Figure 4.17(d) highlights the controller's resilience against input step battery voltage variations (100 V to 80 V and 120 V), maintaining stable speed regardless of the power supply fluctuations.

The simulation results effectively showcase the effectiveness of the proposed drive across various operating conditions. The drive's performance during transient load, speed, and input voltage variations demonstrates the robustness of the SRM drive design.

4.5.2 Grid to Vehicle Mode

Simulation results were conducted to validate the proposed grid-to-vehicle (G2V) system, which operates in both constant current (CC) and constant voltage (CV)

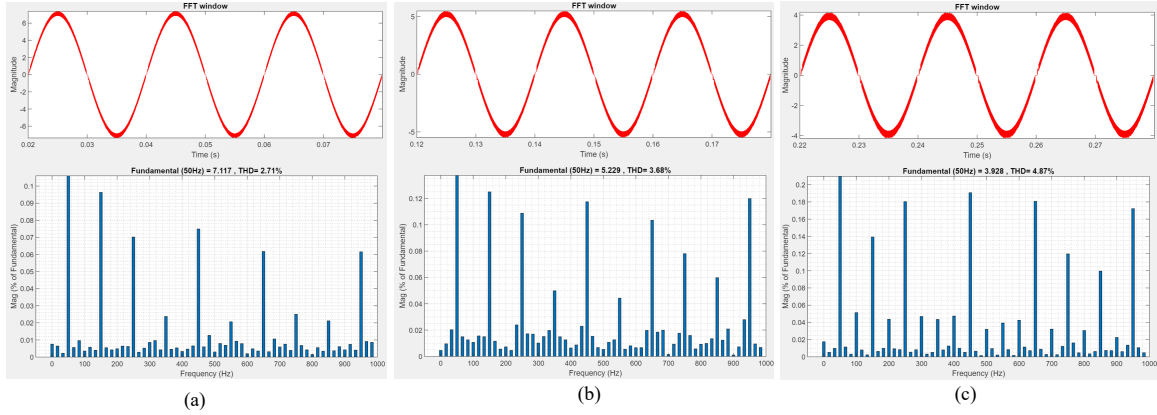


Figure 4.19: Simulation results showing THD for different reference currents. (a) 5 A (b) 3.67 A (c) 2.5 A.

modes. In CC mode, employed when the battery state of charge (SOC) is below 80% for fast charging, while CV mode is utilized for SOC levels exceeding 80%, enabling slow charging. The simulations encompass step variations in both input grid voltages and reference grid currents. Figure 4.18 illustrates the resulting grid voltage and current, as well as battery voltage and current.

In Figure 4.18(a), the simulation results for step variations in input grid voltage are presented, alongside varied reference grid currents to maintain a constant battery current. These results demonstrate unity power factor (UPF) operation with a total harmonic distortion (THD) below 5%. Figure 4.18(b) showcases the simulation results during slow charging in CV mode when battery SOC is above 80%.

The THD results presented in Figure 4.19 demonstrate that the G2V system operates under Unity Power Factor (UPF) across various reference currents, with THD levels conforming to the IEEE power quality standards (IEEE 519-2022). Specifically, simulations indicate a minimum THD of 2.71% at the rated reference current of 5 A, while a higher THD of 4.87% is observed at lower reference currents, such as 2.5 A. Overall, the simulation results validate the efficient performance of the proposed G2V system, confirming its capability to operate effectively under diverse conditions while meeting stringent power quality requirements. However, it is crucial to note that THD levels exceed 5% in light load conditions (below 2.5 A).

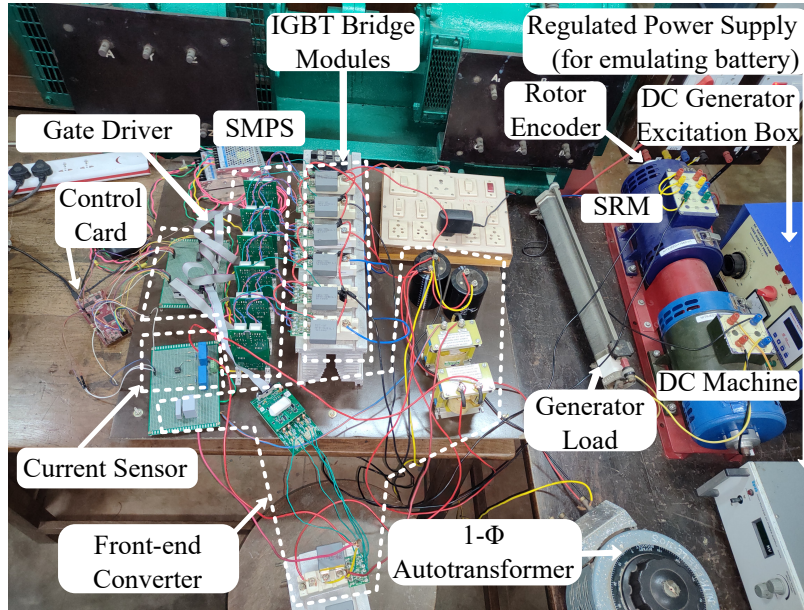


Figure 4.20: Photograph of the experimental setup.

4.6 Experimental Results

An experimental prototype featuring a one hp Switched Reluctance Motor (SRM) coupled with a DC generator is setup, depicted in Figure 4.20. Six SKM50GB12T4 IGBT modules are employed to configure the Miller converter, with Skyper 32R serving as the driver for these modules. For the Ćuk converter, the two switches (T_1 and T_2) are realized using another SKM50GB12T4 IGBT module with Skyper 32R driver. To form the capacitance C_1 in the Ćuk converter, a combination of Power film capacitors (MKP1848) totaling $5\mu F$ (consisting of $4\mu F$ and $1\mu F$ capacitors in parallel) is employed. Electrolytic capacitors serve as C_{bat} and C_2 in the system. An incremental quadrature encoder, ERA50T with 1024 PPR connected to the SRM shaft is used for rotor position sensing. The speed is also deduced from the encoder. Hall current sensor, LA25P is used to sense current. A potential divider circuit followed by a differential amplifier with DC offset is used to sense the grid voltage during G2V mode. The control system is implemented using a TMS320F28379D DSP microcontroller. Experimental results are presented for motoring and G2V modes are presented in subsequent sections.

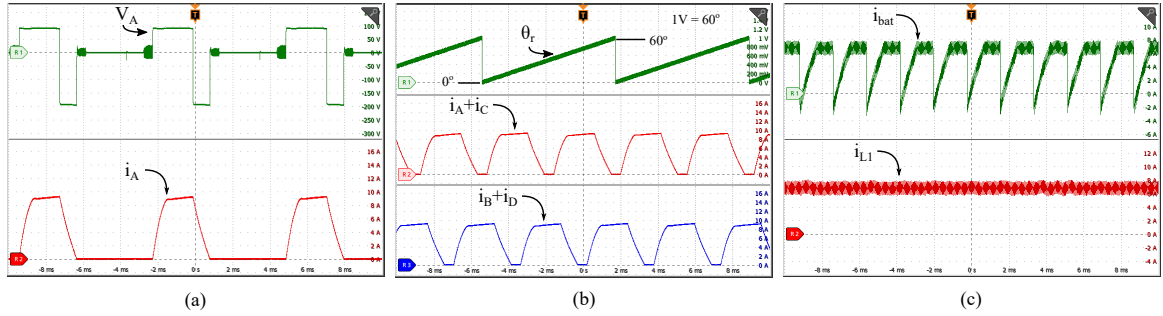


Figure 4.21: Experimental results showing the operational waveforms in motoring mode at 1400 rpm. (a) Phase A voltage and current. (b) Rotor position and phase currents. (c) Input battery current and inductor current.

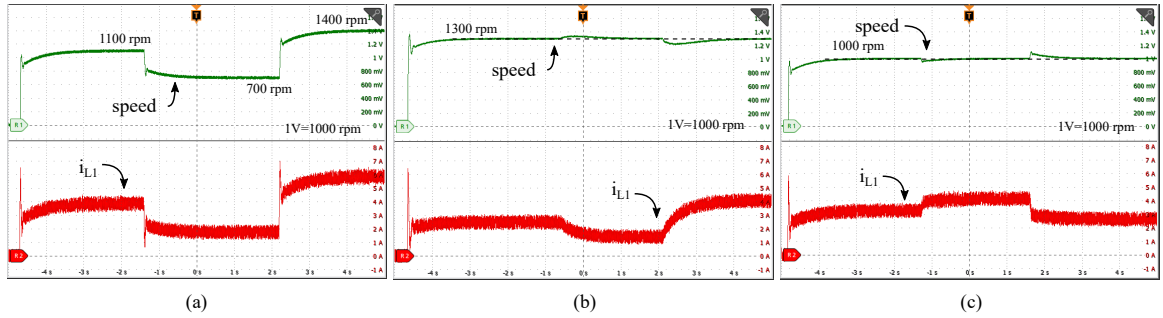


Figure 4.22: Experimental results depicting speed and input inductor current (i_{L1}) waveforms during motoring mode across various operating conditions. (a) Step reference speed variations (1100 rpm, 700 rpm, 1400 rpm). (b) Constant speed operation at 1300 rpm with variations in load torque. (c) Constant speed operation at 1000 rpm under variations in input battery voltage through 80 V, 100 V, and 120 V.

4.6.1 Motoring mode

In the motoring mode, a DC regulated power supply ranging from 0 to 800V serves as the DC source. A 100 Ω , 5A rheostat connected across the DC generator armature terminals loads the setup to load the Switched Reluctance Motor (SRM). The loading is adjustable by varying the excitation to the DC generator. Experimental results, depicted in Figures 4.21 and 4.22, are detailed below.

Figure 4.21(a) illustrates the voltage and current in phase A at 1400 rpm, indicating higher demagnetization voltage and faster demagnetization. In Figure 4.21(b), rotor position (electrical angle) and phase currents at 1400 rpm are displayed. The rotor position is shown via Digital Storage Oscilloscope (DSO) using the controller's Digital-to-Analog Converter (DAC), revealing current sharing during commutation. Figure 4.21(c) presents inductor current and input current, exhibiting a 0.5A ripple

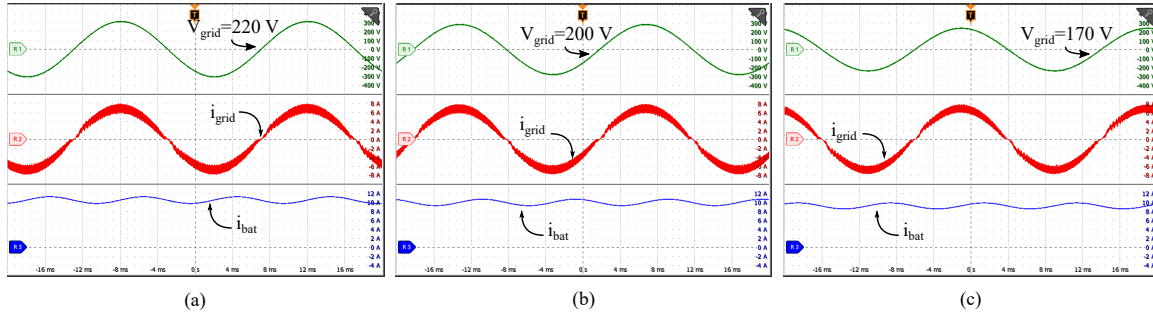


Figure 4.23: Experimental results showing grid voltage, grid current, and battery current in G2V charging mode for constant grid current at different grid voltages. (a) $V_{grid}=220V$. (b) $V_{grid}=200V$. (c) $V_{grid}=170V$

in the input current with occasional dips into negative values during commutation.

Figure 4.22 showcases speed and inductor current (i_{L1}) in various dynamic operating scenarios. The speed, depicted through DAC of the microcontroller, is illustrated in Figure 4.22(a) for step reference speed variations (1100 rpm, 700 rpm, 1400 rpm), with a settling time of 3s and no overshoot in speed observed. Figure 4.22(b) displays speed and inductor current waveforms when the speed reference is set to 1300 rpm and the load is varied, showing minor overshoots and undershoots during load changes. Figure 4.22(c) illustrates speed waveform and inductor current waveforms as the input voltage varies from 100V to 80V to 120V for a reference speed of 1000 rpm. Despite voltage fluctuations, robust tracking of the reference speed is evident.

In conclusion, the experimental results demonstrate the effective performance of the system across a range of operating conditions, showcasing robust speed control in the tested conditions.

4.6.2 G2V mode

In G2V charging mode, a single-phase supply is connected via an autotransformer. A 100Ω rheostat serves as the load in G2V mode. Experimental findings regarding variations in input voltage and reference grid current are depicted in Figures 4.23 and 4.24.

The experiment conducted with varied voltage aims to validate the proposed on-board charger’s ability to handle dynamic fluctuations in grid voltage. Figure 4.23 displays the input grid voltage, grid current, and output DC load current across different voltage levels (220V, 170V, and 200V). The Total Harmonic Distortion (THD)

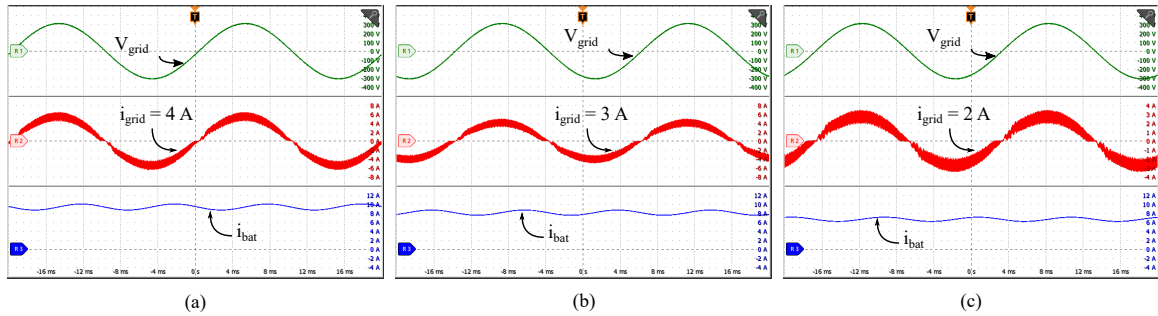


Figure 4.24: Experimental results showing grid voltage, grid current, and battery current in G2V charging mode for different reference grid currents at grid voltage of 220V. (a) $I_{grid}=4A$. (b) $I_{grid}=3A$. (c) $I_{grid}=2A$.

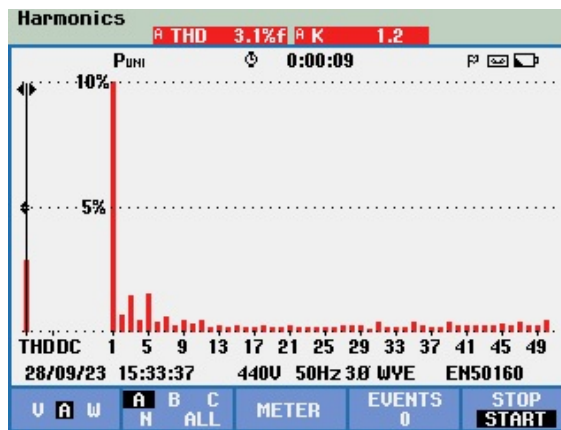


Figure 4.25: Experimental results showing power quality analyzer result showing THD for reference current of 4A.

of the input current, measured in accordance with IEEE power quality standards, aligns with simulation results.

Experimental validation is also conducted for lower reference grid currents to assess the charger’s performance during slow charging within CV mode. Figure 4.24 presents experimental results for various reference current values (4A, 3A, and 2A), revealing an increase in grid current THD as the reference current decreases, with the lowest THD observed at the rated current of 4A. Figure 4.25 shows the Fluke power quality analyzer results, indicating the current THD obtained for the 4A reference current.

In conclusion, the experimental results confirm the capability of the proposed integrated on-board charger to effectively charge from a single-phase grid.

4.7 Conclusions

The presented bidirectional dual-port Ćuk converter-fed SRM drive, with integrated on-board charging capability, offers a promising solution for advancing EV technology. In driving mode, employing the modified v/f control strategy with an extended conduction angle results in improved efficiency and reduced torque ripple, crucial for enhancing overall vehicle performance. The Ćuk converter, serving as the front-end converter, facilitates precise speed control and enhances the torque-ampere ratio with a higher demagnetization voltage. Moreover, in grid-to-vehicle (G2V) mode, the drive seamlessly transitions to act as a diode bridge, followed by the Ćuk converter in reverse, effectively serving as a power factor correction (PFC) converter. This dual functionality not only reduces costs but also enhances the power density of the EV system, making it a cost-effective and efficient charging solution.

Simulation and experimental validation of the proposed system demonstrate its robustness across motoring and G2V charging modes. In motoring mode, the system exhibits precise speed tracking and torque control under varying load conditions, achieving settling times within 3 seconds and negligible overshoot. Additionally, in G2V mode, the system maintains unity power factor operation with THD below 5% at rated current, even amidst dynamic variations in grid voltage. The presentation of grid current during slow charging further validates the system's charging performance for a full charging cycle, ensuring stability throughout. These metrics underscore the robustness of the proposed system across different operating modes and under transient fluctuations in system parameters.

Chapter 5

A Bidirectional Interleaved Totem Pole PFC-based IOBC for EV SRM Drive

This chapter presents an improved IOBC tailored for a 4-phase SRM drive. The proposed IOBC is non-isolated and utilizes the totem pole PFC operation for reduced common-mode voltage. Furthermore, the proposed system accommodates bidirectional functions, ensuring versatility during charging mode. A non-isolated IOBC for SRM with reduced common-mode voltage and bidirectional capability has largely been ignored in the literature. The proposed system utilizes a modified Miller converter in the motoring mode and is easily reconfigured into a two-phase interleaved totem pole converter during charging modes without the need for any magnetic contactors. The proposed system features zero instantaneous torque (ZIT) at steady-state, ensuring minimal machine wear during charging modes. The proposed IOBC is controlled to ensure symmetric positive and negative grid currents for any given rotor position (during charging), thereby eliminating even harmonics and enhancing the power quality of grid current. The proposed system achieves charging power twice the motoring power with parallel-connected phase windings. Ansys electromagnetic transient simulation, MATLAB-based SRM drive simulations, experimental results, and comprehensive comparative analysis are presented to validate the various features (motoring mode, G2V and V2G modes) and effectiveness of the proposed IOBC for SRM based EVs.

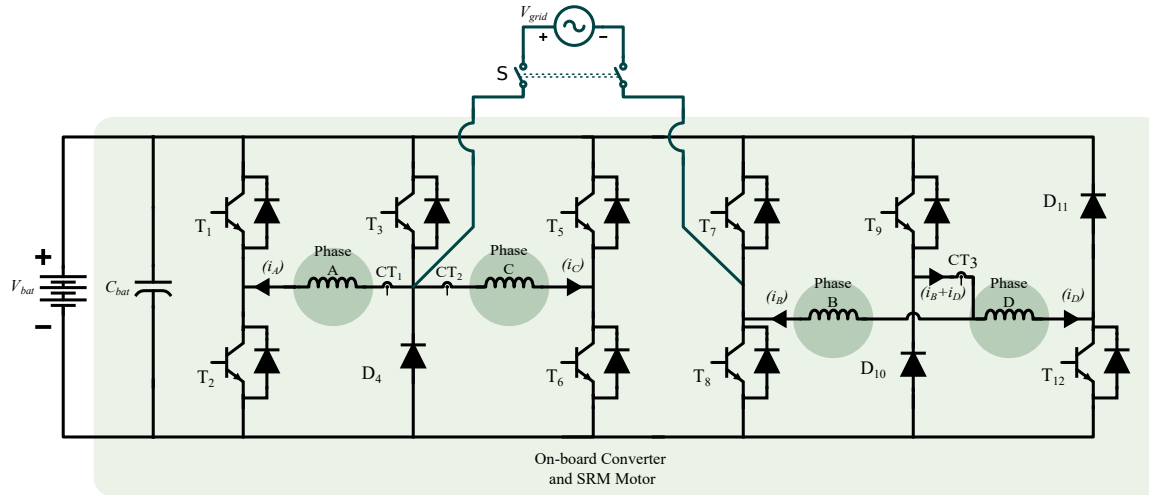


Figure 5.1: Circuit configuration for the proposed SRM drive.

5.1 Proposed System

Figure 5.1 shows the circuit configuration for the proposed SRM drive. It comprises a modified Miller converter-fed SRM drive with three current sensors: CT_1 for measuring phase A current (i_A), CT_2 for measuring phase C current (i_C), and CT_3 for measuring the sum of currents in phases B and D ($i_B + i_D$). In the presented drive, the converter intentionally incorporates asymmetry with diode D_{11} to minimize costs, as diodes are less expensive compared to IGBT/MOSFET. Nevertheless, symmetry can be restored by substituting D_{11} with IGBT/MOSFET. The subsequent sections explain the operating modes and control of the proposed converter during motoring and charging (G2V and V2G) modes.

5.1.1 Motoring and Regenerative Braking Modes

5.1.1.1 Operating Modes

To achieve independent control of phase currents, the phases are shared between alternate phases as depicted in Figure 5.1. The various operating states for phase A winding during motoring/regenerative braking modes are illustrated in Figure 5.2. During magnetization, T_2 and T_3 conduct to apply the battery voltage across the windings. In freewheeling mode, T_3 is turned off to apply zero voltage across the winding, while the switch T_2 and the diode D_4 conduct for the winding current to decay due to winding resistance. When both T_2 and T_3 are turned off, negative

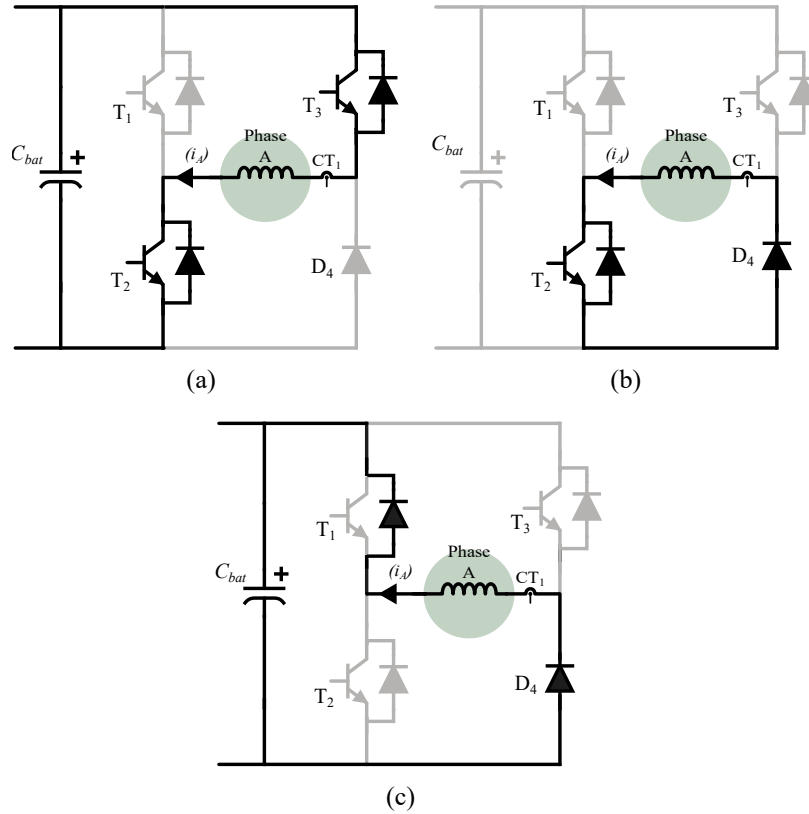


Figure 5.2: Three operating states of phase A during the motoring and regenerative braking modes. (a) Magnetization mode. (b) Zero voltage mode. (c) Demagnetization mode.

battery voltage is applied through D_4 and the reverse diode of T_1 to demagnetize the windings before entering the negative torque region. The identical approach is followed for the remaining phases as well. The switching table and the current sensor to be read during each switching mode are shown in Table 5.1. During motoring, the phase windings are energized in the positive inductance slope region, whereas during regenerative braking, they are energized in the negative inductance slope region.

5.1.1.2 Control Design

The procedure for linear model development and subsequent controller design is detailed in the sections 2.2 and 3.3. The current controller (type 2 compensator) is designed using the K-factor approach Venable (1983) to achieve a desired phase margin of 70° at a loop gain bandwidth of 800 Hz (as the switching frequency is 10 kHz). Similarly, the speed controller is designed for a loop gain bandwidth of 4 Hz and with

Table 5.1: Table showing the switching states and sensor used for each phase during motoring and regenerative braking modes.

Components	Phase A			Phase B			Phase C			Phase D		
	Mag ¹	FW ²	Demag ³	Mag ¹	FW ²	Demag ³	Mag ¹	FW ²	Demag ³	Mag ¹	FW ²	Demag ³
Switches / Diodes	T ₂ , T ₃	T ₂ , D ₄	D ₄ , Diode of T ₁	T ₈ , T ₉	T ₈ , D ₁₀	D ₁₀ , Diode of T ₇	T ₃ , T ₆	T ₆ , D ₄	D ₄ , Diode of T ₅	T ₉ , T ₁₂	T ₁₂ , D ₁₀	D ₁₀ , D ₁₁
Current Sensor	CT ₁			CT ₃			CT ₂			CT ₃		

- ¹ Magnetization mode.
² Freewheeling mode.
³ Demagnetization mode.

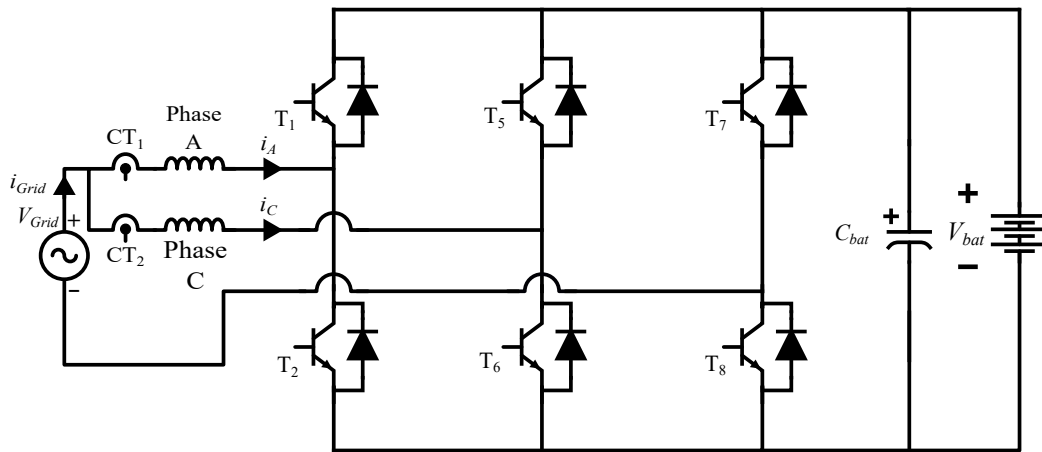


Figure 5.3: Circuit configuration of the power converter during charging mode (reconfigured version of the circuit in Figure 5.1).

a desired phase margin of 80° . The obtained controller transfer function is in the continuous domain. This is discretized using bilinear transformation for a sampling period of $20\mu s$ for the digital implementation of the controller.

5.1.2 Charging (G2V and V2G) modes

5.1.2.1 Operating Modes

During the charging (G2V and V2G) modes, when the vehicle is parked, the rotor shaft must first be disengaged from the transmission and, hence, the wheels, allowing the rotor to rotate freely. Then, the switch S in Figure 5.1 is closed. During steady-state operation, as the dc-link voltage exceeds the peak grid voltage, the free-wheeling

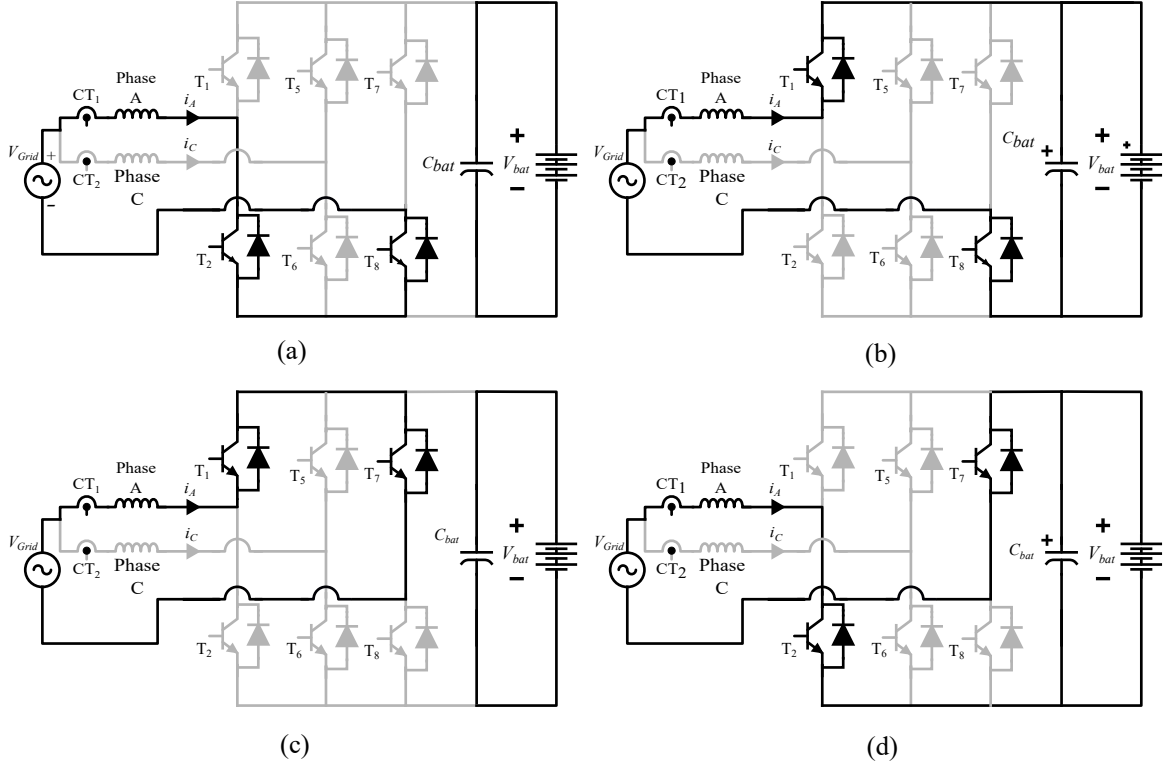


Figure 5.4: Operating modes for phase A winding in G2V/V2G modes. (a) While T_2 is turned on during the positive cycle. (b) While T_2 is turned off during the positive cycle. (c) While T_1 is turned on during the negative cycle. (d) While T_1 is turned off during the negative cycle.

diode of T_3 and the diode D_4 remain non-conductive. Switches $T_1, T_2, T_5, T_6, T_7,$ and T_8 form a two-phase interleaved totem pole PFC rectifier, as depicted in Figure 5.3.

The operational modes of the converter in AC grid-connected modes for phase A are illustrated in Figure 5.4. The totem-pole PFC operates in the positive and negative cycles of the AC mains input. The current flow depends on how T_2 and T_1 are switched. The switches, together with the inductor, create a synchronous boost converter. Similarly, phase C operates interleaved with phase A, utilizing switches T_5 and T_6 with a 180° phase shift.

Figure 5.5 illustrates the control block diagram for G2V and V2G modes. In the positive half cycle, T_2 and T_6 serve as boost switches with duty cycles d_1 and d_2 , while T_1 and T_5 are driven by complementary PWM signals $(1-d_1)$ and $(1-d_2)$ respectively. Simultaneously, T_8 conducts continuously. In the negative half cycle, the roles reverse

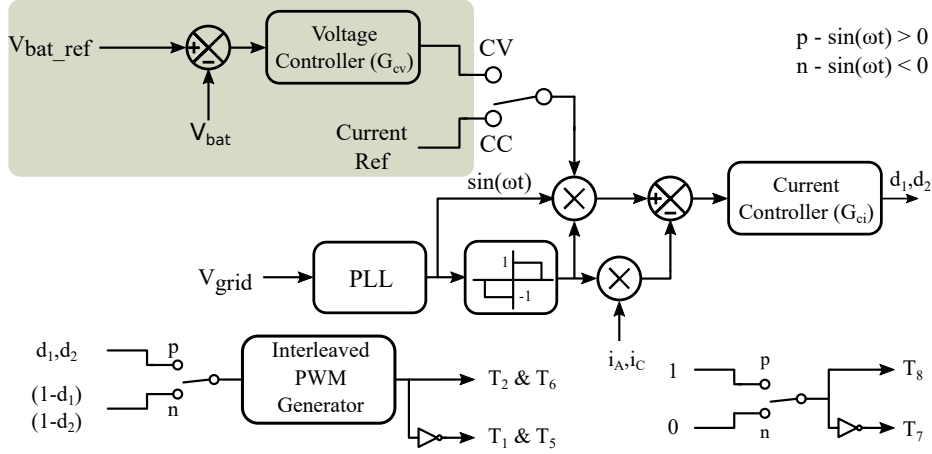


Figure 5.5: Control block for G2V (positive current reference) and V2G (negative current reference) modes.

with T_1 and T_5 as boost switches, and T_2 and T_6 driven by complementary PWM signals. Throughout, T_7 conducts continuously. Seamless bidirectional operation is achieved by switching T_8 during the positive cycle and T_7 during the negative half cycle of the input voltage.

5.1.2.2 Control Design

As shown in Figure 5.5, the converter can operate in constant voltage (CV) and current (CC) modes. In CV mode, the battery voltage is regulated, while in CC mode, the grid current (or indirectly the battery current) is regulated. A second-order generalized integrator (SOGI) based phase locked loop (PLL) with offset rejection is designed and implemented [Xie et al. \(2017\)](#). The reference peak current is multiplied by the sine output of the PLL and the sign of grid voltage to get the reference current. The measured current is multiplied by the sign of grid voltage and compared with the reference current. That is:

$$i_{Aref} = i_{Cref} = I_{ref} |\sin(\omega t)| \quad (5.1)$$

$$|i_A| = \begin{cases} i_A & \sin(\omega t) > 0 \\ -i_A & \sin(\omega t) < 0 \end{cases} \quad (5.2)$$

In V2G mode, the reference peak current is set to a negative value.

The machine windings have a rating of 2.5 A. In grid-connected modes, where two

windings are interleaved, the controller is specifically designed for a rated current of 2.5 A per inductor. The small signal model for the converter is derived based on an average inductance value [Erickson and Maksimovic \(2007\)](#). The subsequent sections provide a detailed discussion of the variation of inductance with respect to the rotor position. The voltage and current controllers shown in [Figure 5.5](#) are designed using the K-factor method [Venable \(1983\)](#). The current controller is designed to achieve a phase margin of 60° at a loop gain bandwidth of 2 kHz (as the switching frequency is 20 kHz), while the voltage controller is designed for a phase margin of 60° at a loop gain bandwidth of 20 Hz. For digital implementation of the controller, the controller is discretized using bilinear transformation for a sampling period of $20\mu s$.

5.2 Discussion on instantaneous torque and variation of inductance during charging modes

In charging modes, the proposed system functions exclusively with two specific windings: phase A and phase C. As a result, the torque generated is the combined sum of the torques produced by phase A and phase C. Hence, the net torque (T_{net}) is given by:

$$T_{net} = T_A + T_C \quad (5.3)$$

In charging modes, the Totempole PFC is controlled to ensure equal currents in both phases' windings, with the polarity determined by the AC cycles. Nevertheless, the torque generated per phase remains unipolar. This unipolarity is a consequence of the torque per phase in the SRM being directly proportional to the square of the phase current, as illustrated in the equation below:

$$T_{ph} = i_{ph}^2 \frac{dL_{ph}}{d\theta}. \quad (5.4)$$

Equation (5.4), further demonstrates that the magnitude of torque produced per phase also increases with the inductance slope and depends on its sign.

In subsequent sections, individual phase torques and net torque during the charging modes are analyzed theoretically, along with the Ansys and MATLAB Simulink simulation results. To accurately analyze the performance of the SRM during charging mode, an appropriate model needs to be developed using FEA as detailed in [2.1](#).

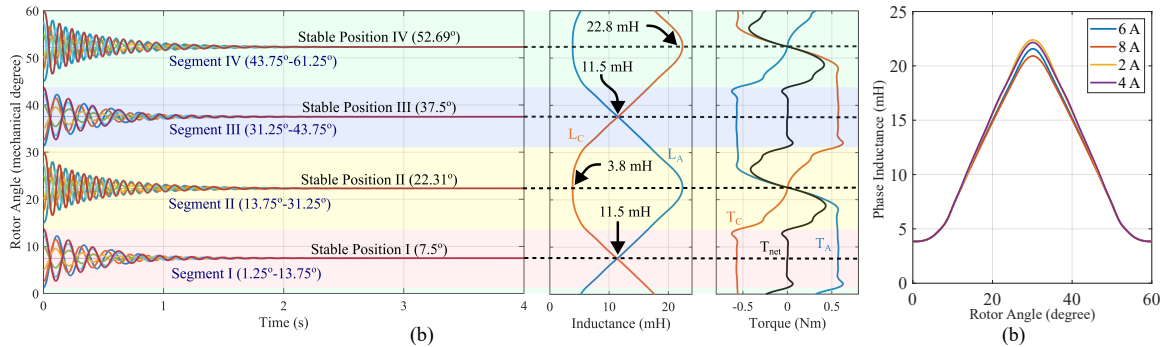


Figure 5.6: FEA results depicting (a) rotor trajectory with arbitrary initial position plotted along with inductance and torque profiles. (b) Phase inductance profile of the SRM for different phase currents.

The obtained model serves two primary purposes: (i) to investigate the transient behavior of the rotor position during charging using Ansys Maxwell Transient analysis, and (ii) to develop a MATLAB Simulink model to analyze the voltage, current, and instantaneous torque generated by the SRM during charging.

The 2D model of the SRM generated using Ansys RMXprt simulation is utilized for the Ansys Maxwell simulation (with the solution type set to Transient). The Ansys Maxwell simulation results are discussed in more detail in the next section.

5.2.1 Ansys Transient Analysis: Results and Discussion

The transient simulation for the Ansys Maxwell model is carried out with the phases A and C excited with 4A peak sinusoidal current (as phases A and C are utilized in charging). Figure 5.6(a) shows the rotor trajectory with different initial rotor positions when the two phases are excited. The position plot is presented along with the phase inductance profile and torque profile of the two phases of the SRM and the net torque for a current of 4A to get a clear understanding. Figure 5.6(b) shows the inductance profile obtained using FEA for different phase current values.

In Figure 5.6(a), one electrical cycle is divided into four segments. In segment I, the slopes of the inductance for phases A and C are opposite, resulting in opposing torques (as per (5.4)). Hence, the rotor tends to settle along the position where the net torque is zero. The same applies to segment III. Consequently, in segments I and III, the rotor settles at the position where the phase inductance values of the phases are exactly equal. These are the positions referred to as stable position I (7.5°)

and stable position II (37.5°) in Figure 5.6(a), with an inductance value of 11.5 mH. Therefore, when the rotor is at stable positions I or III,

$$\frac{dL_A}{d\theta} = -\frac{dL_C}{d\theta} \Rightarrow T_A = -T_C \Rightarrow T = 0 \quad (5.5)$$

Whereas in segment II, as evident from Figure 5.6(a), C-phase torque (T_C) is low compared to A-phase torque (T_A) since phase C is nearly in unaligned position. In segment II, T_A is positive below the stable position II and negative beyond the stable position II. Consequently, if the initial position of the rotor is at any point in segment II, the rotor aligns with phase A of the stator pole at position II (22.31°) during steady state, where the net torque is zero. As a result, the inductances of phases A and C differ at this point. The inductance of phase A matches the aligned inductance (22.8 mH), while the inductance of phase C corresponds to the unaligned inductance (3.8 mH) of the SRM. Similarly, in segment IV, the rotor aligns with phase C of the stator pole at position IV (52.69°), where the net torque is zero. Hence, when the rotor is at stable positions II or IV,

$$\frac{dL_A}{d\theta} = \frac{dL_C}{d\theta} = 0 \Rightarrow T = T_A = T_C = 0 \quad (5.6)$$

Hence, it is clear from the above discussion that with equal currents in phases A and C during charging mode, from any arbitrary initial position, the rotor aligns along any one of the aforementioned stable positions. Figure 5.7 shows the steady-state rotor positions (stable positions I, II, III, and IV) and flux lines during charging modes. From Figure 5.6 and Figure 5.7, it is evident that the maximum angular displacement from any arbitrary initial position to the corresponding stable position is nearly equal to 7.5° .

5.2.2 Inductance values during charging mode

As discussed in the previous section, designing the controller for charging modes requires an accurate small signal model of the power electronic converter. This requires the phase inductance values. From the above discussion, the three potential

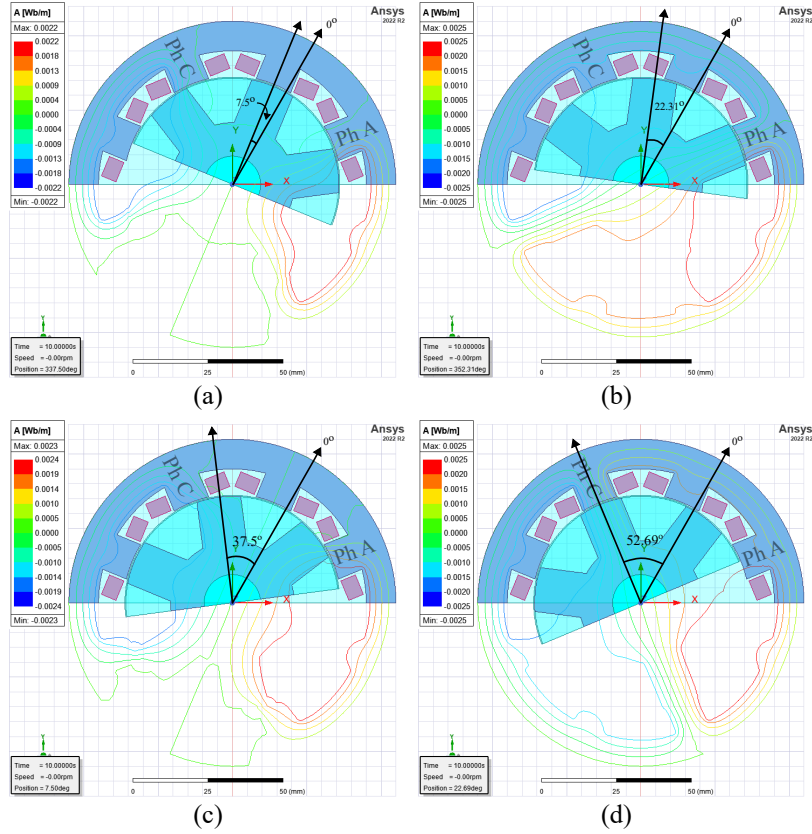


Figure 5.7: Ansys FEA results showing flux lines at the stable positions. (a) Stable Position I (7.5°) (b) Stable Position II (22.31°) (c) Stable Position III (37.5°) (d) Stable Position IV (52.69°)

combinations of inductance values during charging mode are as follows:

$$\begin{aligned}
 L_A = L_C = 11.5 \text{ mH} & \quad \text{Pos I \& III} \\
 L_A = 22.8 \text{ mH } L_C = 3.8 \text{ mH} & \quad \text{Pos II} \\
 L_A = 3.8 \text{ mH } L_C = 22.8 \text{ mH} & \quad \text{Pos IV}
 \end{aligned} \tag{5.7}$$

The average value of inductance of a phase across the four stable positions can be calculated as below:

$$L_{avg} = \frac{(3.8 + 11.5 + 11.5 + 22.8) \text{ mH}}{4} = 12.4 \text{ mH} \tag{5.8}$$

For small signal modeling of the totem pole converter, a filter inductor value of 12.4 mH is assumed, representing the average inductance at stable rotor positions (as in (5.8)). Analysis of (5.7) reveals significant inductance deviations from the average

during stable positions II and IV. Consequently, the phase with the lowest inductance value (3.8 mH) exhibits a higher current ripple, while the phase with a higher inductance value (22.8 mH) experiences a lower ripple. However, interleaving ensures that these variations in inductance values do not impact the power quality of the grid current during charging mode.

Additionally, when different phases are connected during the positive and negative cycles, the filter inductance can vary with the rotor position, potentially leading to unequal inductance values between the positive and negative cycles. This imbalance can result in unsymmetrical currents and the generation of even harmonics. However, in the proposed topology, once the rotor reaches stable positions, the inductance remains constant for both phases during both cycles. This guarantees a symmetric current waveform, effectively preventing the occurrence of even harmonic currents.

5.2.3 Matlab Simulations: Results and Discussion

As discussed in Section III(A), the FEA-based SRM simulation model is employed in MATLAB Simulink to analyze the converter's performance during charging modes. Alongside the SRM model, the converter is designed and implemented in the MATLAB simulation. For this purpose, the DC link capacitor (C_{bat}) is designed considering a battery voltage (V_{bat}) of 400 V, a voltage ripple (ΔV) of 1%, and a minimum power (P_{out}) of 1 kW. The frequency of the output voltage ripple (f_{ripple}) is known to be 100 Hz (given the grid frequency is 50 Hz), and the calculation for C_{bat} is expressed as follows [Hart \(2011\)](#):

$$C_{bat} = \frac{P_{out}}{2\pi f_{ripple} V_{bat}^2 \Delta V} \approx 1000\mu F \quad (5.9)$$

The converter's switching frequency during the charging mode is set at 20 kHz. This MATLAB simulation evaluates the performance of the designed controllers and PFC operation in both charging modes (i.e., G2V and V2G). Furthermore, the simulation validates and presents the phase torque and net torque of the SRM at steady-state positions.

Figure 5.8 illustrates simulation results during charging mode, showcasing input grid voltage, grid current, inductor currents, A-phase and C-phase torques, and net torque at stable positions I, II, III, and IV. In Figure 10, the phase C currents is

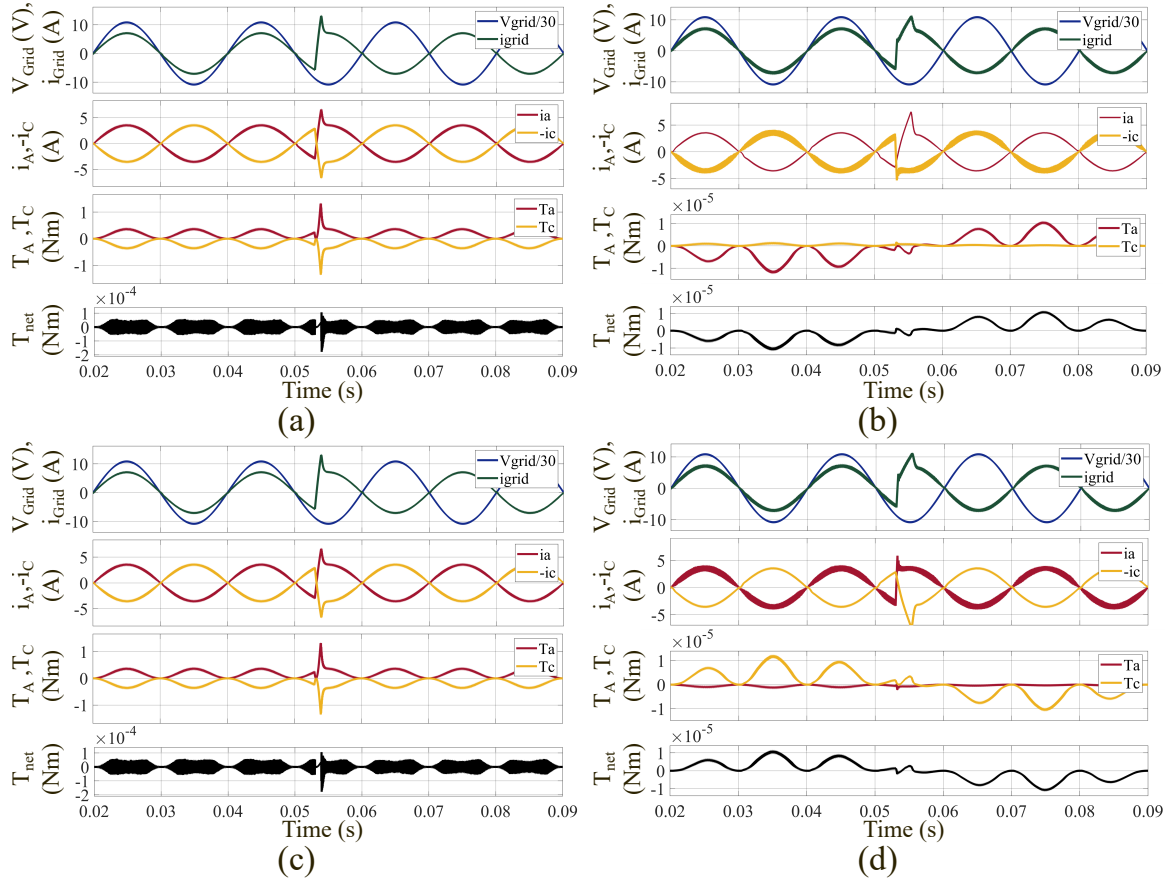


Figure 5.8: Simulation results showing input grid voltage, grid current, inductor currents, A-phase and C-phase torques, and net torque for stable positions. (a) Position I. (b) Position II. (c) Position III. (d) Position IV.

intentionally inverted to enhance visibility. In Figure 5.8(a) (stable position-1), equal current ripples in phase A and phase C are evident due to identical inductances (11.5 mH). Also, it is observed that the A-phase and C-phase torques are equal and opposite, leading to a net instantaneous torque that is negligibly low and a zero average net torque. Additionally, as evident from 5.8(a), during the mode transition from G2V to V2G at 0.053 seconds, the converter exhibits seamless tracking of the reference current, and negligible net torque ensures no pulsation during the switching process.

Figure 5.8(b) displays simulation results for stable position II, revealing unequal current ripples due to differing inductance values (as discussed earlier). Despite the higher phase-C current ripple (3.8 mH), interleaved operation reduces the grid current's THD to 4.61% [Figure 5.8(b)]. Additionally, it can be observed that the phase

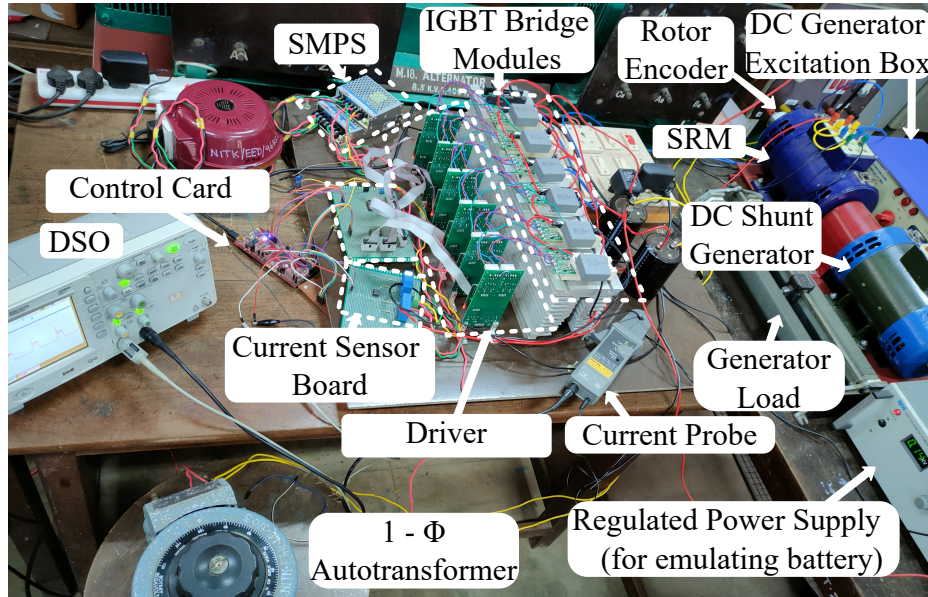


Figure 5.9: Photograph of the experimental setup.

A and phase C torque is low, giving negligible net zero instantaneous torque, and zero average torque.

Similar waveforms are observed at stable positions III and IV (Figure 5.8(c) and Figure 5.8(d)), following patterns seen in stable positions I and II, respectively. From Figure 5.8(b) to Figure 5.8(d), it is also observed that seamless tracking of reference current and negligible instantaneous torque persist during transitions from G2V to V2G and vice versa across stable positions II to IV.

5.3 Experimental Results

To validate the efficacy of the proposed motor drive with IOBC capability for an SRM-based EV, an experimental prototype is set up in the laboratory, featuring a 1-hp SRM coupled with a separately excited DC machine as shown in Figure 5.9. The parameters of the motor employed in the experimental setup are detailed in Table II.

In the experimental setup, a 0-750V, 15A regulated power supply (with voltage setting ranging from 350 to 400V) is used to emulate the battery for testing the motor drive and V2G functionality of the proposed system. For validating the performance of the system in G2V mode, a resistor bank with a rating of 100 Ω , 5A, is used and connected at the DC link to dissipate the power drawn from the grid. The

motor drive prototype comprises six SKM50GB12T4 IGBT legs (rated 1200 V, 50 A) equipped with Skyper 32R drivers. An incremental encoder (ERA50T) with a resolution of 1024 PPR is connected to the motor shaft to detect precise rotor position. Additionally, three hall current sensors (LA25P) are utilized to measure the phase currents, as shown in Figure 5.1. MCP6022 op-amp-based differential amplifier circuits are employed for signal conditioning in the current and grid-side voltage sensing circuits. A DSP microcontroller TMS320F28379D is employed for the digital control implementation of the entire system.

5.3.1 Motoring Mode

The proposed drive in motoring mode is analyzed for steady-state and dynamic performance. To enhance the dynamic performance of the drive, integrator anti-windup using the back-calculation method for the speed loop is incorporated into the closed-loop control system.

Figure 5.10 displays closed-loop steady-state and dynamic waveforms during motoring mode. The efficacy of closed-loop current control is evident in Figure 5.10(a) and 5.10(b), depicting speed and phase current profiles at reference speeds of 300 rpm and 500 rpm, respectively. Figure 5.10(c) reveals that with a speed reference of 800 rpm, the motor settles within 1.52 seconds with minimal overshoot. Similarly, Figure 5.10(d) demonstrates a 2-second settling time with a 100 rpm undershoot at a reference speed of 300 rpm, while the motor operates at 800 rpm. Figure 5.10(e) showcases successful tracking of the reference speed, demonstrating the efficacy of the designed controllers. Integral anti-windup implementation effectively mitigates windup effects, contributing to improved control performance for the drive.

5.3.2 G2V and V2G modes

To validate the performance of the experimental prototype of the proposed IOBC's during charging modes, a single-phase autotransformer was employed to connect the AC supply to the converter. The converter, configured in a totem pole arrangement, is operated in closed-loop with two levels of interleaving. The obtained experimental results, showcasing basic waveforms, switch stress, and output voltage, are presented in Figure 5.11. Figure 5.11(a) illustrates the input voltage and duty cycle waveforms for T_2 and T_6 , while Figure 5.11(b) depicts the output waveform of the PLL, along

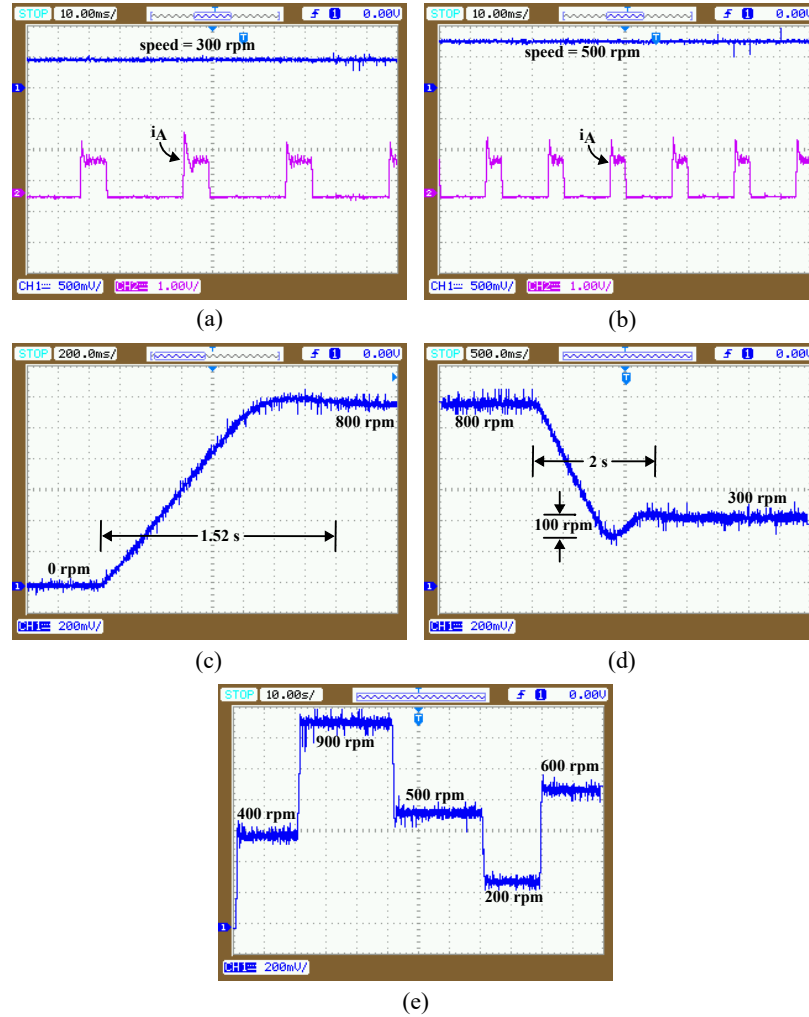


Figure 5.10: Experimental results during motoring mode. (a) Steady-state speed and phase (phase A) current at a speed of 300 rpm. (b) Steady-state speed and phase (phase A) current at a speed of 500 rpm. (c) Speed transient for increasing speed reference from 0 to 800 rpm. (d) Speed transient for decreasing speed reference from 800 to 300 rpm. (e) Speed for variable speed references.

with the two inductor currents and the grid current. It is evident that interleaved operation effectively reduces the ripple in the grid current compared to the two inductor currents. Figure 5.11(c) demonstrates the voltage stress across the low-side switches (T_2 and T_6) and highlights the interleaved operation of the switches with 20 kHz switching frequency. Figure 5.11(d) presents the output DC-link voltage and the dc current. Overall, the waveforms presented in Figure 5.11 closely align with the theoretical analysis and effectively demonstrate the performance of the designed

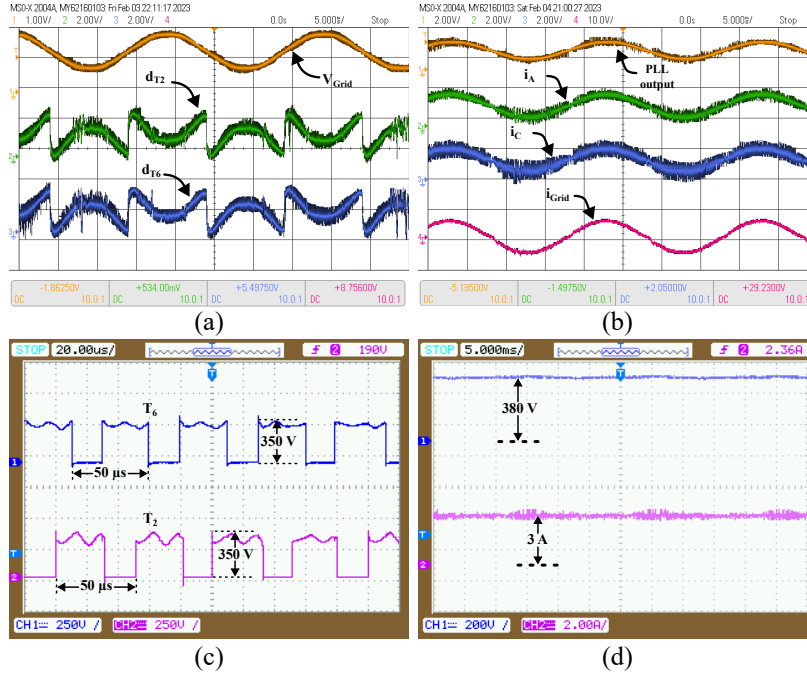


Figure 5.11: Experimental results showing waveforms in G2V/V2G modes for a grid reference current of 4 A. (a) Grid voltage and duty cycles for T_2 and T_6 . (b) PLL output, inductor currents (i_A and i_C), and grid current (i_{Grid}). (c) Voltage across T_2 and T_6 . (d) Battery voltage (V_{bat}) and battery current.

controller.

Figure 5.12 illustrates the steady-state grid current for various grid currents in charging modes. A negative current reference triggers the transition from G2V to V2G mode. THD measurements of grid current for different reference values are performed using a Fluke Power Quality Analyzer. The worst harmonic distortion recorded is 8% for a current of 1.4 A (Figure 5.12(a)), while the lowest harmonic distortion is 3.5% for 4.6 A (Figure 5.12(c)). These THD values adhere to IEEE 519-2022 standards. Remarkably, the converter smoothly achieved PFC operation without any significant torque pulsation in the machine during charging modes. Additionally, Figure 5.12 illustrates symmetric current waveforms with equal ripples in positive and negative cycles. This is further confirmed by the absence of even harmonics in the power quality analysis.

Efficiency is evaluated in both G2V and V2G modes with varying loads, as depicted in Figure 5.13. The system's efficiency peaked at 65% load and dropped to its lowest point at 30% load for both G2V and V2G modes. In G2V mode, the system

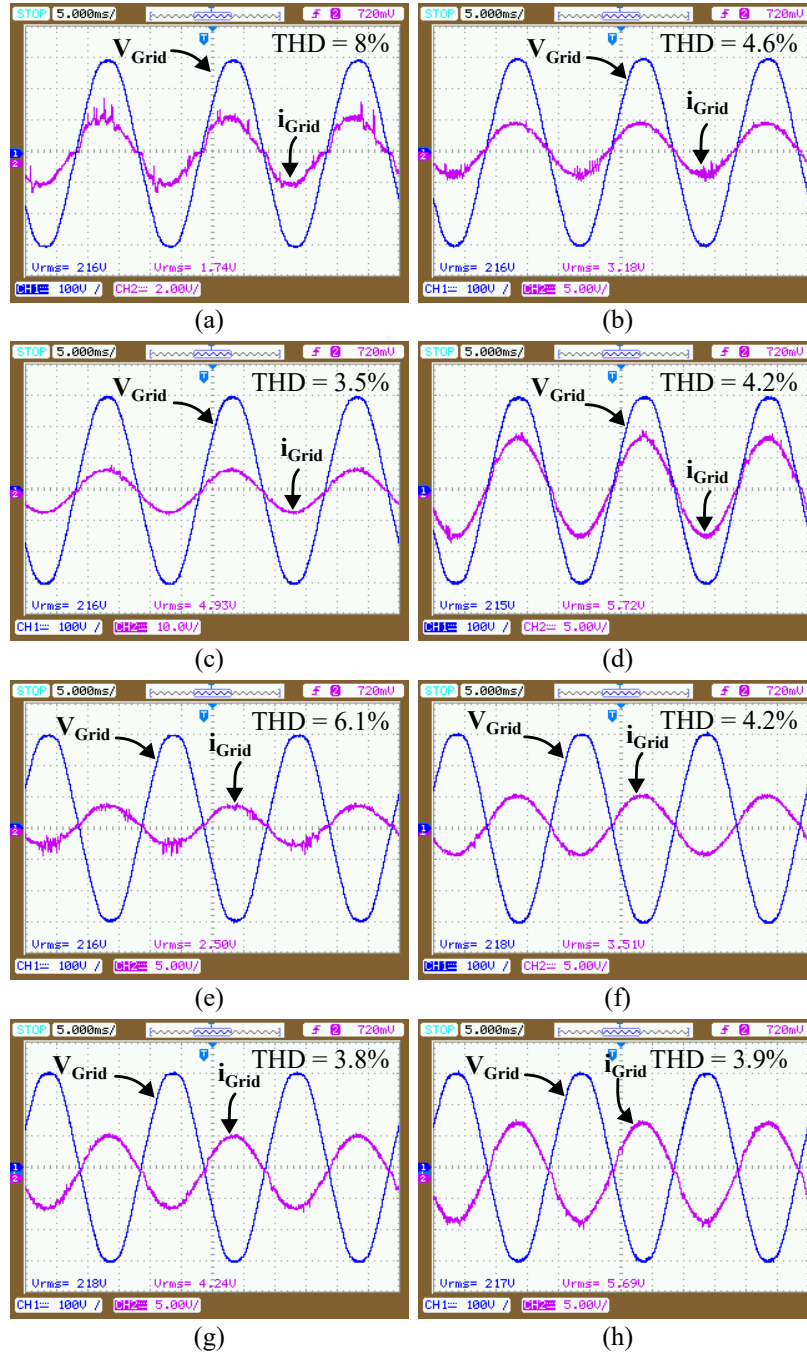


Figure 5.12: Experimental results showing grid voltages and current waveforms in G2V/V2G modes for different reference grid currents. (a) 1.4 A. (b) 2.83 A. (c) 4.6 A. (d) 5.3 A. (e) -2.12 A. (f) -3.18 A. (g) -3.9 A. (h) -5.2 A.

achieved a maximum efficiency of 95.7% and a minimum of 95.23%. In V2G mode, the peak efficiency was recorded at 95.43%, with a minimum of 94.96%. Notably, as

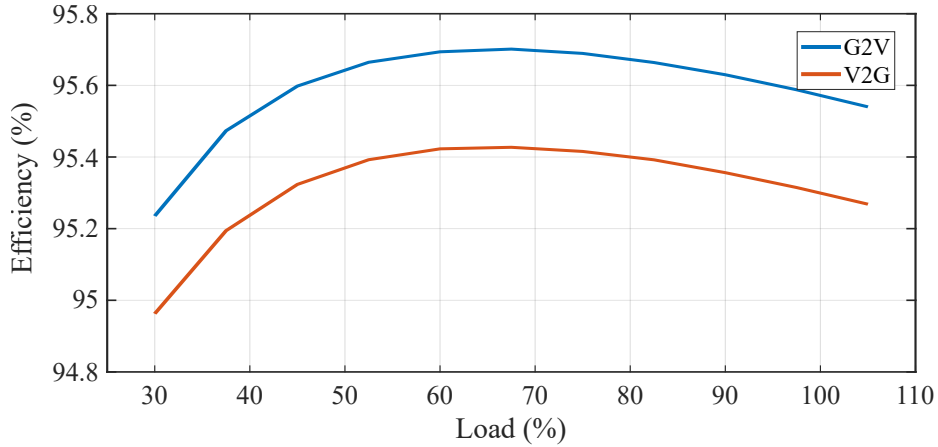


Figure 5.13: Efficiency vs load curve obtained from experimental results.

the load increases from the lowest efficiency at 30%, there is a subsequent decrease in efficiency beyond the 65% load mark. These findings underscore the system’s robust performance across varying load conditions.

Table 5.2 provides a comprehensive comparison of the proposed IOBC’s features against other reported IOBCs for SRM-based EVs. The comparison is based on various key criteria, including instantaneous electromagnetic torque production during charging, even harmonics, power electronic component count, magnetic contactor usage, bidirectional capability, and power capacity. From Table 5.2, it can be inferred that the proposed SRM drive with IOBC capability (with interleaved totem pole PFC operation) exhibits bidirectional power transfer with a capacity twice that of traction power. During charging mode, the system achieves ZIT operation, eliminating torque pulsations. By employing equal filter inductance values in both positive and negative cycles during charging modes, the proposed converter maintains symmetrical grid current, effectively suppressing even harmonics. Additionally, the absence of additional magnetic contactors for reconfiguration contributes to the system’s cost-effectiveness.

5.4 Conclusions

In conclusion, this chapter investigates the effect of utilization of machine windings as filter inductors in SRM based IOBCs. The chapter introduces a novel IOBC system specifically designed for a 4-phase SRM drive. The proposed IOBC employs a modified Miller converter in motoring mode and seamlessly transitions to a two-phase

Table 5.2: Comparison of different IOBCs utilizing machine windings as filter inductors for SRM based EVs

Reference	ZIT	Equal Inductance in +ve and -ve Cycles	Switches	Diodes	Magnetic Contactors	Bidirectional Capability	Totem Pole PFC	Charging power capability (in times of SRM traction power)
Chang and Liaw (2009)	×	×	8	8	2	×	×	1
Chang and Liaw (2011)	×	✓	10	0	3	×	×	1
Cai and Zhao (2021)	✓	×	6	6	0	×	×	1
Shah and Payami (2021)	✓	×	6	8	0	×	×	2
Chen et al. (2019)	×	×	8	8	0	×	×	1
Shah and Payami (2023)	✓	✓	6	8	0	×	×	2
Proposed	✓	✓	9	3	0	✓	✓	2

interleaved totem pole converter during charging modes, eliminating the need for magnetic contactors. Leveraging interleaved totem pole PFC operation, the system attains commendable power quality, heightened efficiency, and reduced common mode leakage currents in charging modes (G2V/V2G).

This versatile IOBC demonstrates bidirectional capability, accommodating various operational modes, including G2V, V2G, V2V, etc., although the G2V and V2G functionalities are exclusively validated in this study. The IOBC's circuit configuration and control ensures ZIT for the motor during charging, mitigating wear and tear induced by torque pulsations. The system's performance is further substantiated through simulations conducted using Ansys and Matlab Simulink, validating its efficacy in charging modes.

Experimental results from the hardware prototype of the IOBC affirm the SRM drive's performance in both driving and charging modes. Key findings from the theoretical analysis, simulation and experimental results include:

- ZIT on the motor during charging modes.
- Grid current THD below 5% under near-rated conditions.
- PFC operation (>0.99 power factor) ensuring enhanced power quality in the grid current during charging.
- Equal inductance in positive and negative cycles of the grid voltage, resulting in symmetrical grid currents with no even harmonics.
- Usage of zero magnetic contactors for transitioning from motoring to charging modes.
- Bidirectional operation with minimum number of power electronic components (i.e. 9 switches and 3 diodes).
- Peak efficiencies of 95.7% in G2V mode and 95.43% in V2G mode.
- Precise tracking of motor speed reference with superior dynamic performance (settling time = 1.52 s and 100 rpm overshoot) in motoring mode.

In summary, the proposed IOBC system demonstrates robust performance across various modes, providing a promising solution for efficient and high-quality power transfer in 4-phase SRM drives.

Chapter 6

Conclusion and Future Scope

This chapter presents the conclusions and contributions of this thesis. Suggestions regarding the future scope for further research in this area are also included.

6.1 Conclusions and Contributions of the Thesis

This thesis has explored the promising realm of EVs and their propulsion systems, focusing particularly on the utilization of SRM drives and the integration of IOBC. The overarching goal has been to address key challenges hindering the widespread adoption of EVs while advancing sustainable transportation solutions.

Through a thorough exploration of SRM drives, this research has highlighted their inherent advantages, such as efficient operation, fault tolerance, and minimal rotor losses. Despite challenges like higher torque ripple and lower power density, this study has underscored the potential of SRMs in EV propulsion and emphasized the need for further research and enhancement in this domain. Moreover, the integration of IOBCs has been identified as a significant step towards enhancing the efficiency and functionality of EV systems. By seamlessly combining motor driving and charging functions, IOBCs offer cost savings, reduced complexity, and increased power density. The bidirectional capability of IOBCs enables diverse operating scenarios like grid-to-vehicle (G2V), vehicle-to-grid (V2G), vehicle-to-load (V2L), and vehicle-to-home (V2H), thereby adding versatility to EV systems.

This thesis has made several notable contributions to the field of electric vehicle propulsion and charging systems. The development of accurate simulation models for Switched Reluctance Motors (SRMs) is fundamental for the successful implemen-

tation and evaluation of proposed solutions in this thesis. Throughout the research journey, it became evident that precise characterization of SRMs is essential to capture their intricate behavior accurately. Various methods, ranging from analytical approaches to electromagnetic Finite Element Analysis (FEA) tools, are available for SRM characterization, each offering unique advantages and trade-offs. This thesis has detailed the development of a MATLAB Simulink model derived from FEA-based characterization of an SRM prototype. This obtained model allows intricate analysis of the proposed solutions in the thesis. Furthermore, the procedure for obtaining a linearized SRM model for controller design is also detailed in the thesis. In essence, these models lay the groundwork for conducting comprehensive simulation studies on the proposed solutions. These help to gain valuable insights into the performance, efficiency, and feasibility of SRM-based propulsion systems and integrated on-board chargers (IOBCs) for electric vehicles.

The thesis has contributed significantly to the advancement of SRM drive technology across medium-power applications through the proposal and comprehensive validation of novel drive configurations and control strategies. The first part of the thesis focused on the development and validation of a cost-effective SRM drive utilizing a Miller converter-fed SRM motor with a single current sensor. By addressing the absence of a structured control development procedure in existing literature and leveraging the K-factor method for controller design, the proposed drive demonstrated robust performance across variable speed, variable torque, and constant power modes. The integration of hardware prototypes and rigorous experimentation underscored the feasibility and effectiveness of the proposed solution, paving the way for practical implementation within cost constraints without compromising performance.

Furthermore, the introduction of a bidirectional dual-port Ćuk converter-fed SRM drive with IOBC capability and accelerated demagnetization represents a significant advancement in the field. Through detailed analysis and simulation studies, the thesis elucidated the impact of various control strategies on torque ripple, efficiency, and demagnetization in SRM drives. The proposed Ćuk converter-fed SRM drive exhibited robust performance and cost reduction potential, offering increased power density and versatility across multiple operational modes. The validation of these findings through simulations and experimental prototypes reaffirmed the viability of the proposed solution for real-world applications.

Lastly, the thesis addressed the challenges and opportunities in enhancing IOBC

systems for 4-phase SRM drives, with a particular focus on utilizing machine windings as filter inductors. By exploring novel configurations and control strategies, the thesis demonstrated the potential for increased power density, cost reduction, and improved reliability in IOBC systems. Detailed discussions are provided regarding the effects of utilizing machine windings as filter inductors, including the mitigation of torque pulsations and the variation of inductance during charging modes. This thesis introduces a totem pole PFC converter-based bidirectional OBC that utilizes machine windings as filter inductors during charging. The proposed converter promises higher efficiency, reduced common-mode voltage, and versatile operating modes with bidirectional capability compared to the IOBCs reported in the literature. Extensive simulation studies and experimental validation were conducted and presented to assess the suitability of the proposed IOBC for electric vehicle applications.

In conclusion, this thesis comprehensively explores the integration of SRMs in EVs and IOBCs to improve efficiency and functionality. Through simulation studies and experimental validation, novel solutions for SRM drives and IOBC systems are proposed, addressing challenges including reliability, efficiency, safety, and cost. The results demonstrate robust performance and validate the advantages of these proposed systems, paving the way for advancements in sustainable transportation solutions. Overall, this research contributes valuable insights and practical solutions to advance SRM drive technology, offering promising avenues for future research and industrial implementation.

6.2 Future Research Prospects

The control strategy proposed in this thesis employs a dedicated position sensor along with a single current sensor, as sensorless strategies are either computationally intensive or require more memory storage. Future research could focus on developing sensorless control methods that are less resource-intensive and more suitable for medium-power applications. Another potential area for exploration is the investigation and implementation of advanced nonlinear control strategies to further reduce torque ripple.

However, the proposed single-sensor configuration introduces a single point of failure, which could render the entire drive system inoperable if the sensor fails. To mitigate this risk, a redundant sensor configuration or fault-tolerant control algorithms

could be considered.

The v/f control strategy with extended conduction periods and accelerated demagnetization, as proposed in this thesis, utilizes a Ćuk converter in the front-end. While effective, the Ćuk converter presents limitations for higher power applications due to increased component stress. Further research into more suitable front-end converters for v/f controlled SRM drives with accelerated demagnetization in higher power applications is necessary. Additionally, investigating converter and control strategies to improve efficiency at low speeds offers promising future directions.

The experimental validation of the SRM drive in this thesis was limited by the available experimental setup. Extending this validation to include operations in the constant power region, above base speed, is a logical next step. Moreover, instantaneous torque measurements were not conducted, and experimental analysis of torque ripple is needed to gain deeper insights into torque ripple minimization strategies.

The IOBC system proposed in this thesis, which utilizes machine windings as filter inductors, is non-isolated, raising safety concerns for real-world applications, particularly in high-power scenarios. Isolated IOBCs utilizing machine windings have received limited attention in the literature. Further research into isolated IOBCs utilizing machine windings could render them suitable for high-power applications. Additionally, exploring Silicon Carbide (SiC)-based SRM drives with IOBC capability could enhance efficiencies in both driving and charging modes.

Bibliography

- Ahmad, S. S. and Narayanan, G. (2020). Modeling of single-pulse operated switched reluctance generator and its verification. *IEEE Transactions on Industry Applications*, 56(5):4966–4976.
- Bae, H. and Krishnan, R. (1996). A study of current controllers and development of a novel current controller for high performance srm drives. In *IAS'96. Conference Record of the 1996 IEEE Industry Applications Conference Thirty-First IAS Annual Meeting*, volume 1, pages 68–75. IEEE.
- Bilgin, B., Howey, B., Callegaro, A. D., Liang, J., Kordic, M., Taylor, J., and Emadi, A. (2020). Making the case for switched reluctance motors for propulsion applications. *IEEE Transactions on Vehicular Technology*, 69(7):7172–7186.
- Bilgin, B., Jiang, J. W., and Emadi, A. (2019). *Switched reluctance motor drives: fundamentals to applications*. CRC press.
- Bodetto, M., Marcos-Pastor, A., El Aroudi, A., Cid-Pastor, A., and Vidal-Idiarte, E. (2015). Modified cuk converter for high-performance power factor correction applications. *IET Power Electronics*, 8(10):2058–2064.
- Bodo, N., Levi, E., Subotic, I., Espina, J., Empringham, L., and Johnson, C. M. (2017). Efficiency evaluation of fully integrated on-board ev battery chargers with nine-phase machines. *IEEE Trans. Energy Convers.*, 32(1):257–266.
- Boldea, I., Tutelea, L. N., Parsa, L., and Dorrell, D. (2014). Automotive electric propulsion systems with reduced or no permanent magnets: An overview. *IEEE Transactions on Industrial Electronics*, 61(10):5696–5711.

- Bose, B. K., Miller, T. J. E., Szczesny, P. M., and Bicknell, W. H. (1986). Micro-computer control of switched reluctance motor. *IEEE Transactions on Industry Applications*, IA-22(4):708–715.
- Bostanci, E., Moallem, M., Parsapour, A., and Fahimi, B. (2017). Opportunities and challenges of switched reluctance motor drives for electric propulsion: A comparative study. *IEEE Transactions on Transportation Electrification*, 3(1):58–75.
- Cai, H., Guan, B., and Xu, L. (2014). Low-cost ferrite pm-assisted synchronous reluctance machine for electric vehicles. *IEEE Transactions on Industrial Electronics*, 61:5741–5748.
- Cai, J. and Zhao, X. (2021). An on-board charger integrated power converter for ev switched reluctance motor drives. *IEEE Transactions on Industrial Electronics*, 68(5):3683–3692.
- Chang, H.-C. and Liaw, C.-M. (2009). Development of a compact switched-reluctance motor drive for ev propulsion with voltage-boosting and pfc charging capabilities. *IEEE Transactions on Vehicular Technology*, 58(7):3198–3215.
- Chang, H. C. and Liaw, C. M. (2011). An integrated driving/charging switched reluctance motor drive using three-phase power module. *IEEE Transactions on Industrial Electronics*, 58(5):1763–1775.
- Chau, K. T., Chan, C. C., and Liu, C. (2008). Overview of permanent-magnet brushless drives for electric and hybrid electric vehicles. *IEEE Transactions on Industrial Electronics*, 55(6):2246–2257.
- Chaurasiya, S. K., Bhattacharya, A., and Das, S. (2023). Reduced switch multi-level converter for grid fed srm drive to improve magnetization and demagnetization characteristics of an srm. *IEEE Transactions on Industry Applications*, 59(6):6804–6816.
- Chen, H. C. and Huang, B. W. (2021). Integrated G2V/V2G Switched Reluctance Motor Drive with Sensing only Switch-Bus Current. *IEEE Transactions on Power Electronics*, 36(8):9372–9381.

- Chen, H.-C., Wang, W.-A., and Huang, B.-W. (2019). Integrated driving/charging/discharging battery-powered four-phase switched reluctance motor drive with two current sensors. *IEEE Transactions on Power Electronics*, 34(6):5019–5022.
- Cheng, H., Wang, L., Xu, L., Ge, X., and Yang, S. (2020a). An integrated electrified powertrain topology with srg and srm for plug-in hybrid electrical vehicle. *IEEE Transactions on Industrial Electronics*, 67(10):8231–8241.
- Cheng, H., Wang, Z., Yang, S., Huang, J., and Ge, X. (2020b). An integrated srm powertrain topology for plug-in hybrid electric vehicles with multiple driving and onboard charging capabilities. *IEEE Transactions on Transportation Electrification*, 6(2):578–591.
- Cheok, A. D. and Fukuda, Y. (2002). A new torque and flux control method for switched reluctance motor drives. *IEEE Transactions on Power Electronics*, 17(4):543–557.
- de Paula, M. V. and Barros, T. A. d. S. (2022). A sliding mode ditc cruise control for srm with steepest descent minimum torque ripple point tracking. *IEEE Transactions on Industrial Electronics*, 69(1):151–159.
- de Santiago, J., Bernhoff, H., Ekergård, B., Eriksson, S., Ferhatovic, S., Waters, R., and Leijon, M. (2012). Electrical motor drivelines in commercial all-electric vehicles: A review. *IEEE Transactions on Vehicular Technology*, 61(2):475–484.
- Dhale, S., Nahid-Mobarakeh, B., and Emadi, A. (2021). A review of fixed switching frequency current control techniques for switched reluctance machines. *IEEE Access*, 9:39375–39391.
- Erickson, R. W. and Maksimovic, D. (2007). *Fundamentals of power electronics*. Springer Science & Business Media.
- Gan, C., Jin, N., Sun, Q., Kong, W., Hu, Y., and Tolbert, L. M. (2018a). Multiport bidirectional SRM drives for solar-assisted hybrid electric bus powertrain with flexible driving and self-charging functions. *IEEE Transactions on Power Electronics*, 33(10):8231–8245.

- Gan, C., Sun, Q., Jin, N., Tolbert, L. M., Ling, Z., Hu, Y., and Wu, J. (2018b). Cost-effective current measurement technique for four-phase srm control by split dual bus line without pulse injection and voltage penalty. *IEEE Transactions on Industrial Electronics*, 65(6):4553–4564.
- Gan, C., Sun, Q., Wu, J., Kong, W., Shi, C., and Hu, Y. (2019). Mmc-based srm drives with decentralized battery energy storage system for hybrid electric vehicles. *IEEE Transactions on Power Electronics*, 34(3):2608–2621.
- Gan, C., Wu, J., Hu, Y., Yang, S., Cao, W., and Kirtley, J. L. (2016). Online sensorless position estimation for switched reluctance motors using one current sensor. *IEEE Transactions on Power Electronics*, 31(10):7248–7263.
- Hannoun, H., Hilairret, M., and Marchand, C. (2007). Analytical modeling of switched reluctance machines including saturation. In *2007 IEEE International Electric Machines & Drives Conference*, volume 1, pages 564–568. IEEE.
- Hart, D. W. (2011). *Power electronics*, volume 166. McGraw-Hill New York.
- Hu, K.-W., Yi, P.-H., and Liaw, C.-M. (2015a). An ev srm drive powered by battery/supercapacitor with g2v and v2h/v2g capabilities. *IEEE Transactions on Industrial Electronics*, 62(8):4714–4727.
- Hu, Y., Gan, C., Cao, W., Fang, Y., Finney, S. J., and Wu, J. (2016). Solar pv-powered srm drive for evs with flexible energy control functions. *IEEE Transactions on Industry Applications*, 52(4):3357–3366.
- Hu, Y., Gan, C., Cao, W., Li, C., and Finney, S. J. (2015b). Split converter-fed srm drive for flexible charging in ev/hev applications. *IEEE Trans. Ind. Electron.*, 62(10):6085–6095.
- Hu, Y., Gan, C., Sun, Q., Li, P., Wu, J., and Wen, H. (2018). Modular tri-port high-power converter for srm based plug-in hybrid electrical trucks. *IEEE Transactions on Power Electronics*, 33(4):3247–3257.
- Ilic, M., Marino, R., Peresada, S., Taylor, D., et al. (1987). Feedback linearizing control of switched reluctance motors. *IEEE Transactions on Automatic Control*, 32(5):371–379.

- Inderka, R. and De Doncker, R. (2003). Dirc-direct instantaneous torque control of switched reluctance drives. *IEEE Transactions on Industry Applications*, 39(4):1046–1051.
- Jain, A. and Mohan, N. (2005). Srm power converter for operation with high demagnetization voltage. *IEEE Transactions on Industry Applications*, 41(5):1224–1231.
- Khaligh, A. and Dantonio, M. (2019). Global trends in high-power on-board chargers for electric vehicles. *IEEE Transactions on Vehicular Technology*, 68:3306–3324.
- Klein-Hessling, A., Burkhart, B., Scharfenstein, D., and De Doncker, R. W. (2014). The effect of excitation angles in single-pulse controlled switched reluctance machines on acoustics and efficiency. In *2014 17th International Conference on Electrical Machines and Systems (ICEMS)*, pages 2661–2666.
- Krishnan, R. (2017). *Switched reluctance motor drives: modeling, simulation, analysis, design, and applications*. CRC press.
- Kumar, P., Israyelu, M., and Sashidhar, S. (2023). A simple four-phase switched reluctance motor drive for ceiling fan applications. *IEEE Access*, 11:7021–7030.
- Kwon, M. and Choi, S. (2017). An electrolytic capacitorless bidirectional ev charger for v2g and v2h applications. *IEEE Transactions on Power Electronics*, 32:6792–6799.
- Le-Huy, H. and Brunelle, P. (2005). A versatile nonlinear switched reluctance motor model in simulink using realistic and analytical magnetization characteristics. In *31st Annual Conference of IEEE Industrial Electronics Society, 2005. IECON 2005.*, pages 6 pp.–.
- Lee, D.-H., Liang, J., Lee, Z.-G., and Ahn, J.-W. (2009). A simple nonlinear logical torque sharing function for low-torque ripple sr drive. *IEEE Transactions on Industrial Electronics*, 56(8):3021–3028.
- Metwly, M. Y., Abdel-Majeed, M. S., Abdel-Khalik, A. S., Hamdy, R. A., Hamad, M. S., and Ahmed, S. (2020). A Review of Integrated On-Board EV Battery Chargers: Advanced Topologies, Recent Developments and Optimal Selection of FSCW Slot/Pole Combination. *IEEE Access*, 8:85216–85242.

- Moghaddam, R. R. and Gyllensten, F. (2014). Novel high-performance synrm design method: An easy approach for a complicated rotor topology. *IEEE Transactions on Industrial Electronics*, 61:5058–5065.
- Mohamadi, M., Rashidi, A., Nejad, S. M. S., and Ebrahimi, M. (2018). A switched reluctance motor drive based on quasi z-source converter with voltage regulation and power factor correction. *IEEE Transactions on Industrial Electronics*, 65(10):8330–8339.
- Monteiro, V., Pinto, J. G., and Afonso, J. L. (2016). Operation modes for the electric vehicle in smart grids and smart homes: Present and proposed modes. *IEEE Transactions on Vehicular Technology*, 65:1007–1020.
- Na, T., Yuan, X., Tang, J., and hang, Q. Z. (2019). A review of on-board integrated electric vehicles charger and a new single-phase integrated charger. *CPSS Transactions on Power Electronics and Applications*, 4.
- Outlook, G. E. (2021). Trends and developments in electric vehicle markets.
- Park, M.-H., Baek, J., Jeong, Y., and Moon, G.-W. (2019). An interleaved totem-pole bridgeless boost pfc converter with soft-switching capability adopting phase-shifting control. *IEEE Trans. Power Electron.*, 34(11):10610–10618.
- Pasquesoone, G., Mikail, R., and Husain, I. (2011). Position estimation at starting and lower speed in three-phase switched reluctance machines using pulse injection and two thresholds. *IEEE Transactions on Industry Applications*, 47(4):1724–1731.
- Peng, F., Ye, J., and Emadi, A. (2016). A digital pwm current controller for switched reluctance motor drives. *IEEE Transactions on Power Electronics*, 31(10):7087–7098.
- Peng, F., Ye, J., and Emadi, A. (2017a). An asymmetric three-level neutral point diode clamped converter for switched reluctance motor drives. *IEEE Transactions on Power Electronics*, 32(11):8618–8631.
- Peng, F., Ye, J., Emadi, A., and Huang, Y. (2017b). Position sensorless control of switched reluctance motor drives based on numerical method. *IEEE Transactions on Industry Applications*, 53(3):2159–2168.

- Pires, V. F., Pires, A. J., Cordeiro, A., and Foito, D. (2020). A review of the power converter interfaces for switched reluctance machines. *Energies*, 13.
- Pollock, C. and Williams, B. (1990). Power convertor circuits for switched reluctance motors with the minimum number of switches. *IEE Proceedings B (Electric Power Applications)*, 137(6):373–384.
- Rahman, K., Fahimi, B., Suresh, G., Rajarathnam, A., and Ehsani, M. (2000). Advantages of switched reluctance motor applications to ev and hev: design and control issues. *IEEE Transactions on Industry Applications*, 36(1):111–121.
- Ralev, I., Qi, F., Burkhart, B., Klein-Hessling, A., and De Doncker, R. W. (2017). Impact of Smooth Torque Control on the Efficiency of a High-Speed Automotive Switched Reluctance Drive. *IEEE Transactions on Industry Applications*, 53(6):5509–5517.
- Rivera, S., Goetz, S. M., Kouro, S., Lehn, P. W., Pathmanathan, M., Bauer, P., and Mastromauro, R. A. (2023). Charging infrastructure and grid integration for electromobility. *Proc. IEEE*, 111(4):371–396.
- Sadeghi, Z., Nejad, S. M. S., Rashidi, A., and Shahparasti, M. (2021). Fast demagnetization and vibration reduction in switched reluctance motor drive system. *IEEE Access*, 9:110904–110915.
- Samudio, R. and Pillay, P. (1995). Design of a flexible dsp-based drive development system. In *IAS'95. Conference Record of the 1995 IEEE Industry Applications Conference Thirtieth IAS Annual Meeting*, volume 3, pages 1854–1861. IEEE.
- Shah, V. and Payami, S. (2021). An integrated driving/charging 4-phase switched reluctance motor drive with reduced current sensors for electric vehicle application. *IEEE Journal of Emerging and Selected Topics in Power Electronics*, pages 1–1.
- Shah, V. and Payami, S. (2023). Switched reluctance motor drive-train with fully integrated battery charger and instantaneous zero charging torque for electric transportation. *IEEE Trans. Transp. Electrif.*, pages 1–1.

- Sun, Q., Wu, J., and Gan, C. (2021). Optimized direct instantaneous torque control for srms with efficiency improvement. *IEEE Transactions on Industrial Electronics*, 68(3):2072–2082.
- Tang, Y., He, Y., Wang, F., Xie, H., Rodríguez, J., and Kennel, R. (2021). A drive topology for high-speed srm with bidirectional energy flow and fast demagnetization voltage. *IEEE Transactions on Industrial Electronics*, 68(10):9242–9253.
- Tarbouriech, S. and Turner, M. (2009). Anti-windup design: An overview of some recent advances and open problems. *IET Control Theory and Applications*, 3:1–19.
- Thankachan, J. and Singh, S. P. (2020). Bidirectional multiport solar-assisted srm drive for pure electric vehicle applications with versatile driving and autonomous charging capabilities. *IET Electric Power Applications*, 14(4):570–583.
- TI (2019). *Technical Reference Manual: TMS320F2837xD Dual-Core Microcontrollers*. Texas Instruments. Rev. J.
- Venable, H. D. (1983). The k factor: A new mathematical tool for stability analysis and synthesis. In *Proc. Powercon*, volume 10, page 1. Citeseer.
- Visioli, A. (2006). *Practical PID control*. Springer Science & Business Media.
- Xiao, D., Filho, S. R., Fang, G., Ye, J., and Emadi, A. (2022). Position-sensorless control of switched reluctance motor drives: A review. *IEEE Transactions on Transportation Electrification*, 8(1):1209–1227.
- Xie, M., Wen, H., Zhu, C., and Yang, Y. (2017). Dc offset rejection improvement in single-phase sogi-pll algorithms: Methods review and experimental evaluation. *IEEE Access*, 5:12810–12819.
- Xu, A., Shang, C., Chen, J., Zhu, J., and Han, L. (2019). A New Control Method Based on DTC and MPC to Reduce Torque Ripple in SRM. *IEEE Access*, 7:68584–68593.
- Yan, N., Cao, X., and Deng, Z. (2019). Direct torque control for switched reluctance motor to obtain high torque-ampere ratio. *IEEE Transactions on Industrial Electronics*, 66(7):5144–5152.

- Yang, Z., Shang, F., Brown, I. P., and Krishnamurthy, M. (2015). Comparative study of interior permanent magnet, induction, and switched reluctance motor drives for ev and hev applications. *IEEE Transactions on Transportation Electrification*, 1(3):245–254.
- Ye, J., Bilgin, B., and Emadi, A. (2015a). Elimination of mutual flux effect on rotor position estimation of switched reluctance motor drives considering magnetic saturation. *IEEE Transactions on Power Electronics*, 30(2):532–536.
- Ye, J., Bilgin, B., and Emadi, A. (2015b). An offline torque sharing function for torque ripple reduction in switched reluctance motor drives. *IEEE Transactions on Energy Conversion*, 30(2):726–735.
- Yilmaz, M. and Krein, P. T. (2013). Review of battery charger topologies, charging power levels, and infrastructure for plug-in electric and hybrid vehicles. *IEEE Transactions on Power Electronics*, 28:2151–2169.
- Yu, Z., Gan, C., Ni, K., Chen, Y., and Qu, R. (2021). Dual-electric-port bidirectional flux-modulated switched reluctance machine drive with multiple charging functions for electric vehicle applications. *IEEE Transactions on Power Electronics*, 36(5):5818–5831.
- Zeraoulia, M., Benbouzid, M. E. H., and Diallo, D. (2006). Electric motor drive selection issues for hev propulsion systems: A comparative study. *IEEE Transactions on Vehicular Technology*, 55(6):1756–1764.
- Zhang, Y., Perdikakis, W., Cong, Y., Li, X., Elshaer, M., Abdullah, Y., Wang, J., Zou, K., Xu, Z., and Chen, C. (2019). Leakage current mitigation of non-isolated integrated chargers for electric vehicles. In *IEEE Energy Conversion Congress and Exposition (ECCE)*, pages 1195–1201.
- Zhang, Y., Yang, G., He, X., Elshaer, M., Perdikakis, W., Li, H., Yao, C., Wang, J., Zou, K., Xu, Z., and Chen, C. (2018). Leakage current issue of non-isolated integrated chargers for electric vehicles. In *IEEE Energy Conversion Congress and Exposition (ECCE)*, pages 1221–1227.
- Zhu, Z. Q. and Howe, D. (2007). Electrical machines and drives for electric, hybrid, and fuel cell vehicles. *Proceedings of the IEEE*, 95(4):746–765.

Publications based on the thesis

Papers published in refereed journals

1. **Faheemali T.**, Arun Dominic D. and Prajof Prabhakaran, "A Systematic Approach to Digital Control Development for Four-Phase SRM Drive using Single Current Sensor for Medium Power Applications," *IEEE Access*, doi: 10.1109/ACCESS.2024.33-72988.
2. **Faheemali T.**, Arun Dominic D. and Prajof Prabhakaran, "A Bidirectional Interleaved Totem Pole PFC-based Integrated On-board Charger for EV SRM Drive," *IEEE Access*, doi: 10.1109/ACCESS.2024.3432791.
3. **Faheemali T.**, Arun Dominic D. and Prajof Prabhakaran, "Ćuk Converter-fed SRM Drive with Accelerated Demagnetization and Integrated On-board Charging Capability for EVs," *Elsevier Computers and Electrical Engineering*. (Under Review).

Conference

1. **Faheemali T.**, Arun Dominic D. and Prajof Prabhakaran, "A Novel Single-Pulse Operated SRM Drive with Improved Performance and Integrated On-board Charging Capability for EVs," **2022 IEEE International Power and Renewable Energy Conference (IPRECON)**, Kollam, India, 2022, pp. 1-6, doi: 10.1109/IPRECON55716.2022.10059566.

Biodata

Name : Faheemali T.

Date of birth: 20-02-1991

Marital status: Married

E-mail: faheemalit@gmail.com

Mobile: +91 8592067730

Address

Research Scholar

Department of Electrical & Electronics Engineering

National Institute of Technology Karnataka

Surathkal, Mangaluru, India-575025, India.

Education

- **M.Tech.**, Power Electronics and Drives, Government College of Engineering Kannur (GCEK), Kerala, CGPA - 7.13, 2016.
- **B.Tech**, Electrical & Electronics Engineering, Rajiv Gandhi Institute of Technology (RIT), Percentage - 63.99, 2013.